

Terahertz and Infrared Sensing with Metasurfaces and Spectroscopy Techniques

A thesis by

Irati Jáuregui-López

under the supervision of

Miguel Beruete and Kizkitza Insausti

In fulfillment of the requirements for the degree of Doctor of
Philosophy at the Public University of Navarra

upna

Universidad Pública de Navarra
Nafarroako Unibertsitate Publikoa

Antennas Group

Department of Electrical, Electronic, and Communication Engineering

Pamplona, Marzo 2023

Agradecimientos

A lo largo de este tiempo, han sido muchas las personas que, de una forma u otra, me han ayudado en este camino de la investigación, y de la vida. Espero no olvidarme de nadie en estas líneas.

En primer lugar, me gustaría agradecer a mis supervisores, Miguel y Kizkitza, por la pasión con la que os dedicáis a vuestro trabajo, que hizo posible que entrase, contagiada, en este mundo de la investigación. Gracias de verdad por brindarme esta oportunidad, y por toda la ayuda a lo largo de estos años. Por la confianza, por ayudarme a crecer profesionalmente, y por la paciencia, en los momentos buenos y en los no tan buenos.

Este largo camino hubiese sido muy diferente si no hubiese tenido la suerte de contar con mis compañeros y compañeras del día a día. Gracias a todo el Grupo de Antenas. A las personas que han llegado hace poco, las que continúan, y las que ya se han marchado de los despachos, pero no de mi corazón. Gracias de manera muy especial a Alexia, Unai, Jose, Alicia, Íñigo, Dayan, Osmerly, Biurrun, Choc, David, Douglas, Angel, Carlos Lezaun, Cristina, Kike, María, Mohsen, Antonio. Muchas gracias por estar siempre ahí, por las risas y por alguna que otra lágrima, por los buenos debates y por los chistes malos, por los cafés y las cervezas, por los piques y las competiciones, y por enseñarme que no importa tanto el qué hacer o dónde estar, sino con quién hacerlo.

Gracias a mis personas vitamina, que llevan acompañándome tanto tiempo, siempre dispuestas a sacarme sonrisas y a hacerme sentir en casa, sin importar dónde estemos. A Mer, Javi, y Tiberio, por enseñarme que la amistad no entiende de tiempos, ni de distancias. Y es que como decía Santi, *“qué suerte que aún hay gente que lo hace fácil, aquellos que consiguen que fluya bien”*. Qué suerte la mía teneros en mi vida, y poder ir con vosotros, a cualquier otra parte.

Por último, pero con mayúsculas y exclamaciones, me gustaría agradecer a mi familia. Mi apoyo incondicional, y el pilar más importante de mi vida. Gracias a mis padres, a mi hermana, y a mi abuela que, aunque no esté aquí para ver los frutos, sé que estaría orgullosa de verme por fin en el final de este largo camino. Gracias por confiar en mí más que nadie, por aguantarme en los buenos, pero sobre todo en los malos momentos, por darme fuerza cuando más lo necesitaba, y por todo el amor que me hacéis sentir siempre. No puedo sentirme más orgullosa de la familia que tengo. A Víctor, por apoyarme siempre y aguantar mis berrinches, por siempre hacerme ver el lado positivo de las cosas con una sonrisa, por todo el cariño que me demuestras todos los días. Por ser mi compañero, amigo, y confidente, y por enseñarme lo que significa realmente el amor. No tengo palabras suficientes para agradecer todo lo que me dais.

Muchísimas gracias de verdad, a todas y cada una de las personas que habéis formado parte de mi vida durante estos años, y que habéis compartido conmigo de una forma u otra esta etapa, que llega a su fin.

***“It would not be much of a universe if
it wasn't home to the people you love.”***

-Stephen Hawking-

Abstract

Metamaterials emerged in the early years of the 21st century as artificial materials with unusual parameters, presenting an exotic electromagnetic behavior, with more possibilities for the control of electromagnetic radiation. Since their first experimental realization, the research in the field of electromagnetism had a great momentum and, as a result, numerous designs based on metasurfaces (the planar version of metamaterials) have been proposed for various applications such as telecommunications, security, spectroscopy, imaging, or sensing, among others. This Thesis investigates the use of devices inspired by the metasurfaces paradigm for sensing applications, operating in the terahertz frequency regime. The content of the Thesis can be divided into three distinct parts that are related to the different studies carried out in these years. First, the numerical and experimental design of metasensors for thin films, biological and chemical samples sensing applications. For this purpose, two types of metasurface-based structures are presented: a design with a complicated geometry that allows obtaining results with high sensitivity, and a design based on hole arrays that exploits the phenomenon of extraordinary transmission. On the other hand, the effect of geometry on metasensor patterns and its influence on detection quality is investigated by geometrical modification of a very simple tripod-based design. Finally, the application of mid-infrared spectroscopy for the analysis of oxidative products in animal meat is investigated.

Resumen

Los metamateriales aparecen en los primeros años del siglo XXI como materiales artificiales con parámetros inusuales, que presentan un comportamiento electromagnético exótico, con más posibilidades para el control de la radiación electromagnética. Desde su primera realización experimental, la investigación en el campo del electromagnetismo tuvo un gran impulso y, como resultado, se han propuesto numerosos diseños basados en metasuperficies (la versión plana de los metamateriales) para diversas aplicaciones como las telecomunicaciones, seguridad, espectroscopía, imagen, sensado, etc. En esta Tesis se investiga el uso de dispositivos inspirados en el paradigma de las metasuperficies para aplicaciones de sensado, operando en el régimen frecuencial de los terahercios. El contenido de la Tesis se puede dividir en tres partes diferenciadas que se relacionan con los diferentes estudios que se han llevado a cabo. En primer lugar, el diseño numérico y experimental de metasensores para el sensado de películas delgadas, muestras biológicas, y químicas. Para ello, se presentan dos tipos de estructuras basadas en metasuperficies: un diseño con una geometría complicada que permite obtener resultados con una elevada sensibilidad; y un diseño basado en matrices de agujeros que explota el fenómeno de la transmisión extraordinaria. Por otra parte, se investiga el efecto de la geometría en los patrones de los metasensores y su influencia en la calidad de la detección, mediante la modificación geométrica de un diseño basado en tripolos. Por último, se investiga la aplicación de la espectroscopía de infrarrojo medio para el análisis de productos oxidativos en carne de origen animal.

Table of Contents

Chapter I: Introduction	1
1.1. Infrared, MID-Infrared, and THz waves	3
1.1.1. The Infrared band	4
1.1.2. The Mid Infrared band	5
1.1.3. The Terahertz band	5
1.2. History of metamaterials and metasurfaces	9
1.3. Structure of the thesis	13
Chapter II: THz Metasurfaces and Sensing	17
2.1. Motivation of Thin-film Sensing	18
2.2. Evolution of metasurfaces towards sensing applications	19
2.3. Biological Sensing with Metasurfaces	23
2.4. Our work (A, B): From Meta-atoms to Metageometries	28
Chapter III: Metasurfaces for Food Safety	49
3.1. Polycyclic Aromatic Hydrocarbons (PAHs) – What are they?	50
3.1.1. Health risks and regulation	50
3.1.2. Factors affecting food contamination	52
3.1.3. Detection and quantification techniques. Chromatography	53
3.2. Our work (PAPER C): Metasensor for PAH detection and identification	55
Chapter IV: Alternative Metasurface Designs	75
4.1. Alternative meta-atom designs	76
4.2. Our work (D): Sensitivity enhancement on tripod-based metasurfaces	76
4.3. Extraordinary Transmission Metasurfaces for sensing	77
4.3.1. Extraordinary transmission phenomena	77
4.3.2. Subwavelength Hole Array metamaterials	78
4.4. Our work (E): ET based Hole Array metasurface	81
Chapter V: MIR spectroscopy for food quality determination	93
5.1. Fundamentals of Infrared spectroscopy	94
5.2. IR Instrumentation	96
5.3. MIR applications in Food Systems	100
5.3.1. Meat Oxidation	101
5.4. Our work (Paper F): Application of MIR spectroscopy to Lipid/protein Oxidation Quantification in Foal Meat	102
Chapter VI: Conclusions and Future Lines	125
References	129
Author Merits	145

List of Figures

1.1	Schematic representation of an EM wave	2
1.2	Full electromagnetic spectrum representation	3
1.3	Electromagnetic spectrum: Microwaves, THz, and IR	6
1.4	Schematic of a THz-TDS-based system and its components	8
1.5	Architecture of the VNA-based system employed in this work	9
1.6	Schematic comparison between natural materials and metamaterials	10
1.7	Materials classification in the $\varepsilon - \mu$ plane (real part)	11
1.8	Examples of different applications of metasurfaces working on the THz band	12
2.1	Thin-film sample interaction with traditional and metasurface-based detection techniques	19
2.2	Frequency saturation effect in a coated metasurface for different analyte thicknesses	21
2.3	Examples of different biosensing applications using THz metasurfaces	24
2.4	Electric field distribution in meta-atoms and metageometries. Comparison	28
2.5	Schematic of the layers composing the labyrinth metageometry	29
2.6	Different fungi distributions over the labyrinth metageometry	39
3.1	Parts composing a chromatographic equipment.	54
3.2	Images of a BbF sample on the labyrinth metasurface at different concentrations	56
4.1	Evolution of the tripod metasurface geometry designed in work D	62
4.2	Representation of SHAs in rectangular lattice: unit cell and anomalous ET resonance	77
4.3	Representation of designed SHAs and possible deposition methods	79
5.1	EM spectrum bands and types of interaction.	94
5.2	Molecular vibration types and classification	95
5.3	Main components and operation scheme of Dispersive IR, and FTIR spectrometers	98
5.4	Scheme of a transmittance FTIR, and FTIR-ATR detection methods	99

List of Tables

3.1	Chemical, carcinogenic, and mutagenic properties of PAHs	51
-----	--	----

Acronyms and Constants

AAS	α -amino adipic semialdehydes
ALD	Atomic layer deposition
AS	Amplitude-sensitivity
ATL	Atomic layer lithography
ATR	Attenuated total reflectance
ATS-DR	Agency for Toxic Substances and Disease Register
BaA	Benz[a]anthracene
BCC	Basal cell carcinoma
BbF	Benzo[b]fluoranthene
BaP	Benzo[a]pyrene
Chr	Chrysene
DC	Direct current
DNA	Deoxyribonucleic acid
DNG	double-negative material
DNPH	Dinitrophenylhydrazine
DPS	Double-positive material
EBL	Electron beam lithography
EC	European Commission
EFSA	European Food Safety Authority
EM	Electromagnetic
ENG	Epsilon-negative material
EPA	US Environmental Protection Agency
ET	Extraordinary Transmission
EU	European Union
FA	Fatty acids
FAO	Food and Agriculture Organization
FEL	Free electron laser
FIR	Far Infrared
FOM	Figure of Merit
FS	Frequency-sensitivity
FTIR	Fourier-Transform Infrared
FWHM	Full Width at Half Maximum

GC	Gas chromatography
GHZ	Gigahertz
GGs	γ -glutamic semialdehydes
HDPE	High-density polyethylene
HPLC	High performance liquid chromatography
IARC	International Agency for Research on Cancer
IR	Infrared
JECFA	Expert Committee on Food Additives
LCRD	Laser Communications Relay Demonstration
LDPE	Low-density polyethylene
LHM	Left-handed medium
L_OX	Lipid oxidation
MIR	Mid Infrared
MDA	Malondialdehyde
MNG	Mu-negative material
MP	Mobile phase
MS	Mass Spectrometry
MTM	Metamaterial
NASA	National Aeronautics and Space Administration
NAP	Naphthalene
NIR	Near Infrared
OR	Optical rectification
PAH	Polycyclic Aromatic Hydrocarbons
PCA	Photoconductive Antenna
PP	Polypropylene
P_OX	Protein oxidation
PUFA	Polyunsaturated fatty acids
QCL	Quantum Cascade Laser
QWP	Quarter-wave plate
RHM	Right-handed medium
RNA	Ribonucleic acid
SCF	Scientific Committee on Food
SEIRA	Surface Enhanced Infrared Absorption Spectroscopy
SHA	Subwavelength hole arrays

SNR	Signal-to-noise ratio
SP	Stationary phase
SPP	Surface plasmon polariton
SRR	Split Ring Resonator
TBARS	Thiobarbituric Acid Reactive Substances method
TDS	Time Domain Spectrometer
TE	Transversal electric
THz	Terahertz
TPI	THz pulsed imaging
UV	Ultraviolet
VNA	Vector Network Analyzer
VIS	Visible light
WHO	World Health Organization

Physic Constants

c_0	Speed of light in vacuum, $c_0 = 1/\sqrt{(\epsilon_0\mu_0)} = 3 \cdot 10^8$ (m/s)
η_0	Vacuum wave impedance, $\eta_0 = \sqrt{(\mu_0/\epsilon_0)} \approx 120\pi$ (Ω)
ϵ_0	Vacuum permittivity, $\epsilon_0 = 8.85 \cdot 10^{-12}$ (F/m)
μ_0	Vacuum permeability, $\mu_0 = 4\pi \cdot 10^{-7}$ (H/m)

Chapter I: Introduction

The use of metasurfaces in sensing applications has garnered significant interest in the last decades, due to their unique properties, such as the ability to manipulate the wavefront of electromagnetic waves and their compact size, which make them ideal for integration into sensing systems. However, there is still much to be explored and understood in this field. The goal of this thesis is to advance our understanding of the potential of metasurfaces for sensing applications and to develop novel sensing systems that can exploit these unique properties. The results of this research will have significant implications for the development of new sensing technologies in a wide range of fields, and will contribute to the growth of this important field of research.

This first chapter tries to make a general introduction in which the main concepts or topics to be discussed throughout the thesis are explained, focusing on the history of metamaterials and metasurfaces, as well as on the frequency bands used throughout this work.

Giving a general and exact definition of a wave is complicated. According to Griffiths [1], a wave is *a disturbance of a continuous medium that propagates with a fixed shape at a constant velocity*. For other authors, wave motion consists in the propagation of a physical property or a perturbation (variation of some physical magnitude) described by a certain field, through a medium. However, this is a somewhat abstract definition. We could concretize by saying that, in a wave motion, a dynamic condition is transmitted or propagated, i.e., quantity of motion and energy.

Electromagnetic (EM) waves are waves that are created as a result of vibrations between an electric field (E) and a magnetic field (H), that oscillate in phase and in directions perpendicular to each other, as depicted in Fig. 1.1. Thus, a change in the magnetic field produces a change in the electric field both in time and space, and *vice versa*. In brief, EM waves carry energy that is exchanged between the electric and magnetic components as they travel.

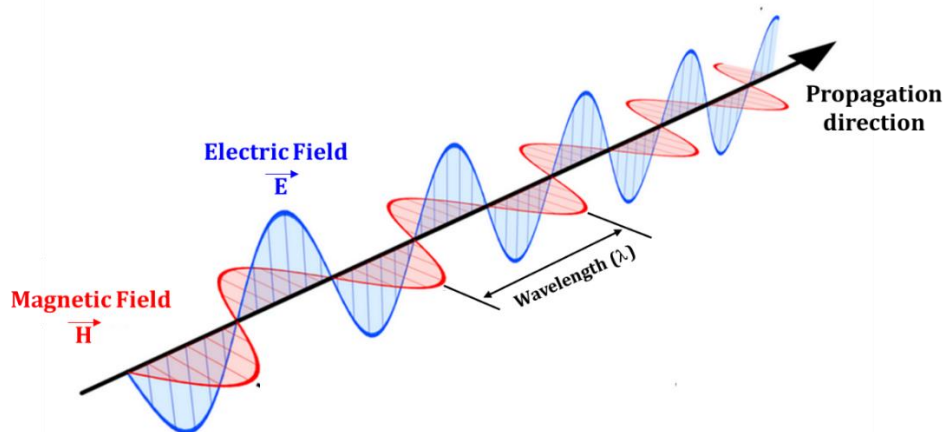


Figure 1.1: Schematic representation of an EM wave.

Unlike other types of waves, such as sound, which would need a material medium to propagate, EM waves can propagate in vacuum at a constant speed (speed of light in vacuum, $c_0 \cong 3 \times 10^8$ m/s). An EM wave propagating through any other medium will travel at the speed of light, c , with $c < c_0$ always [1]. Moreover, EM waves are capable of showing interference or diffraction (as any other type of wave). The main parameters that define an EM wave are its frequency, f , that determines the number of oscillations per unit time and is measured in Hertz (Hz); and its wavelength, λ , the spatial period of the wave and measured in meters (m). Therefore, EM waves can be classified according to these two parameters in what is known as the Electromagnetic Spectrum.

The control of EM waves has been one of the most important topics for the scientific community throughout history, long before Maxwell equations came out and the birth of modern electromagnetism. Long before this, humankind had already invented devices capable of controlling light, such as mirrors or lenses, by simply observing and repeating phenomena occurring in nature, without even knowing that light was an EM wave. In 1895 and after a process of research by different scientists of that time, Maxwell succeeded in formulating the classical theory of EM radiation, unifying for the first time electricity, magnetism, and light as distinct manifestations of a single phenomenon. In fact, Maxwell's most important contribution was to demonstrate theoretically the existence of EM waves

and, in addition, to postulate that light was an EM wave when he saw that his prediction about the speed of propagation coincided with the experimental results of the speed of propagation of light. He also predicted the existence of more EM waves at different frequencies/wavelengths beyond the visible. Later, Maxwell compiled in the laws that bear his name previous experiments and theoretical developments (Gauss's law, Faraday's law, and Ampère's law, which after Maxwell's development is the Ampère-Maxwell law).

Finally, Hertz corroborated Maxwell's theory of the existence of EM waves in a laboratory, and compiled these results in his book [2].

Today, the control of light remains one of the most important research fields of electromagnetism. At the beginning of the 21st century a major milestone in electromagnetism occurred, with the birth of a new class of materials that could be designed to exhibit unusual EM properties, impossible to occur in nature, and named *metamaterials*. This opened up the possibility of having total control over EM waves, giving rise to many real applications such as perfect lenses [3], or cloaking [4], among others.

The main objective of this chapter is to contextualize and highlight the main characteristics of the aforementioned concepts. First, a brief introduction of the frequency bands of the EM spectrum covered in this thesis is discussed. Then, the basics of metamaterials are explained, paying special attention to those applications studied in this thesis.

1.1. Infrared, MID-Infrared, and THz waves

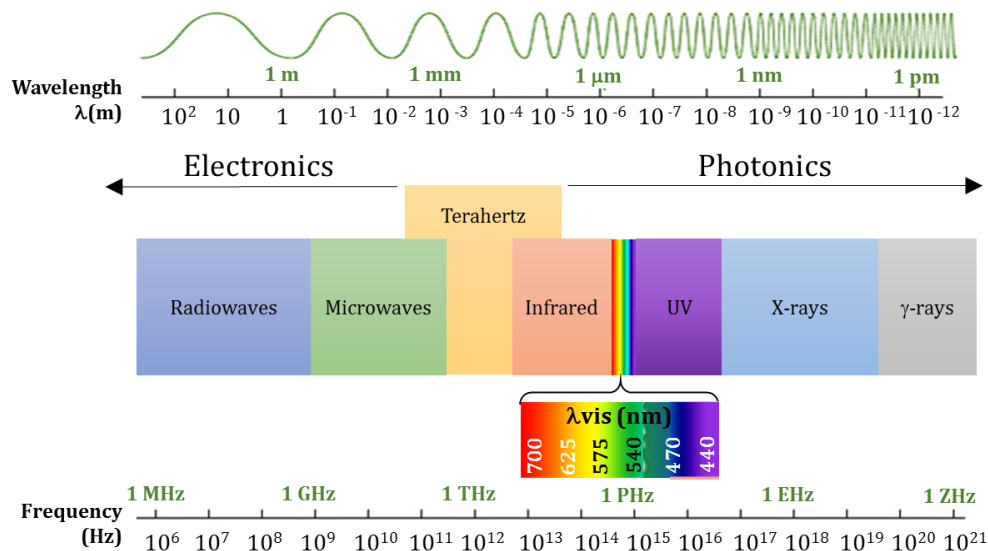


Figure 1.2: Full electromagnetic spectrum representation

EM waves can be classified by their frequency (or equivalently wavelength) within the EM spectrum. Within it, we can distinguish different regions (see Fig. 1.2). At the bottom and top spectrum limits there are waves with a wavelength as long as kilometers (radio waves), and as short as picometers (gamma rays) respectively. Amongst the extremes, there are different bands, where each of them has their own characteristics that make them more

appropriate for some applications than others. Within these regions, we can highlight the Infrared (IR), the Mid Infrared (MIR), and the Terahertz – Far Infrared (THz-FIR) bands, on which we will focus in this thesis.

1.1.1. The Infrared band

Thanks to some discoveries made in the time of Isaac Newton, Huygens, and de Broglie, we know that the white light of the visible spectrum is actually a mixture of different wavelengths, which can be refracted through a prism, and perceived in the visible as colors [5]. Despite the important discoveries reported in his work *Optiks* in 1704, Newton was an advocate of the corpuscular theory (light was composed of tiny particles or corpuscles emitted from a light source) as opposed to the wave theory of Huygens. It was after Huygens' experiments that it was determined that light was a wave [6]. Huygens' explanation was based on the fact that light had a wave behavior, since rectilinear propagation, reflection, diffraction, interference, and refraction (phenomena observed in light) were perfectly explainable by waves. In fact, the definitive argument in support of the wave theory was the double-slit experiment carried out by Young's, in which he tested an interference pattern in the light coming from a distant source as it diffracts through two gratings. Finally, it was concluded (for the time being) that light has a corpuscular (photons) and undulatory character at the same time [6].

On this basis, it was in 1800 that the IR band was discovered by Friedrich Wilhelm Herschel. In his experiments, Herschel used a prism to refract the Sun light into its different colors (or wavelengths), and with the help of a thermometer, he discovered that the temperature in each of these wavelengths was different. Thus, the temperature at the wavelength corresponding to the blue color (470nm) was lower than the temperature measured at the red color (665nm). The most remarkable feature of the experiment was that, when the thermometer was placed beyond the red region (undetectable to human eye), the temperature rose even higher, and was also higher than the room temperature. Thanks to this, he came to the conclusion that there were other wavelengths or, as Herschel called them, other "calorific rays", which were not visible to the human eye, but which had a higher energy than the temperature of the room [7]. Now we refer to these rays as IR radiation (below the red). Other experiments were made by Herschel related to the heat capacity of IR radiation, and discovered that it could be reflected, absorbed, and transmitted, just like visible light [8]. Nowadays, we know as well that a source of IR radiation is heat itself, so that any object being at room temperature will emit this kind of radiation.

IR radiation has been widely used both in the past and in our present days. Nowadays, IR radiation is used in industrial, scientific, and medical applications [9]; being very important in fields such as photonics, within which we can highlight applications such as the design of quantum cascade lasers (QCL), fiber optic communications, optic data storage, chemical sensing, or xerographic laser printing. Recently, the National Aeronautics and Space Administration (NASA) has launched an orbital infrared laser communications system. According to its publications, the Laser Communications Relay Demonstration (LCRD), will leverage the power of infrared light to send and receive information encoded into invisible laser beams from one location to the next. Including benefits such as increased data in a single downlink, or reduced size, weight, and power requirements for a

communications system on a spacecraft [10]. Within the electromagnetic spectrum, IR radiation is located between microwaves and the visible, and can be classified in three regions:

- Far Infrared (FIR): 3 – 12 THz (25 - 100 μm)
- Mid Infrared (MIR): 12 – 120 THz (2.5 - 25 μm)
- Near Infrared (NIR): 120 – 374 THz (0.8 - 2.5 μm)

1.1.2. The Mid Infrared band

MIR waves are considered a subfamily of IR waves and are located between 2.5 and 25 μm (see Fig. 1.3). The importance of this subregion lies in two fundamental facts:

Firstly, one of the most important features of MIR region lies in its potential for molecular spectroscopy applications. Despite the fact that the entire IR band of the EM spectrum contains a high degree of molecular information, since it is the region in which molecular vibrations take place, the main molecular vibrations occur in the MIR band. Here, the two most important areas (the functional group region, and the fingerprint region) are located [11], as will be discussed in more detail in Chapter V.

In addition to spectroscopy, there are several interesting applications taking place in this band. Night vision equipment using IR illumination allows increasing visibility in the dark without actually using a visible light source. In astronomy applications, imaging at IR wavelengths allows observation of objects hidden by interstellar dust, as well as to study the atmospheres of cool stars and planets [12]. IR imaging cameras also have a high potential to detect heat loss in insulated systems [13], to observe changing blood flow in the skin or muscles [14], and to detect overheating of electrical appliances [15], among others. IR radiation is often used to identify structures and molecules because different functional groups give rise to unique band characteristics, as explained in detail in future chapters of this thesis.

1.1.3. The Terahertz band

The THz band is the portion of the EM spectrum placed between microwaves and IR radiation. Although there is no complete consensus about its exact location (depending on the reference consulted, one can find that the lower and upper frequency limits are put either at 100 GHz – 10 THz (3 mm – 30 μm) or 300 GHz – 30 THz (1 mm – 10 μm), it encompasses the radiation with wavelengths ranging from a few tens to thousands of microns. This lack of consensus comes from the multidisciplinary character of the THz band, wherein scientists of diverse disciplines came together in this relatively new band. In one way or another, we set here in a practical way the limits of the THz band of 0.1 and 10 THz being aware that there is some overlap with the microwave regime at the lower limit, and with the FIR band at the upper limit (see Fig. 1.3).

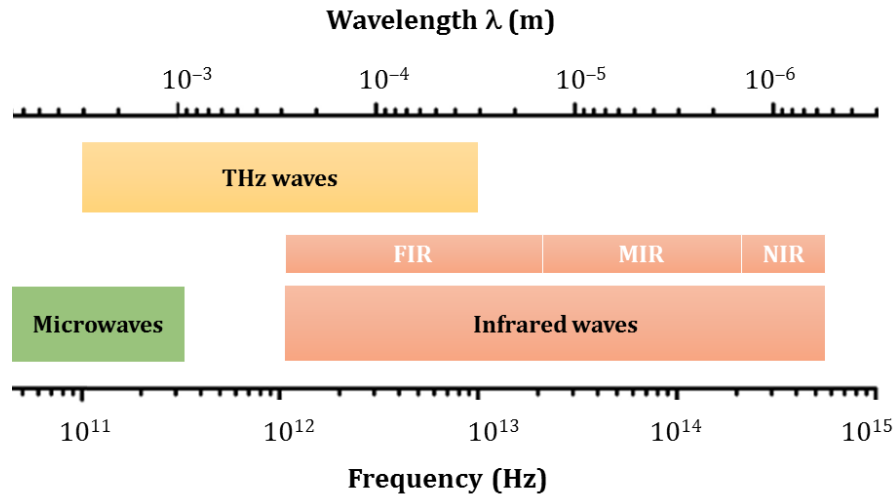


Figure 1.3: Portion of the electromagnetic spectrum covering microwaves, THz, and Infrared frequencies.

Historically, this band has been elusive, to the point that it was known as the “THz gap,” due to the difficulty to generate and detect this radiation efficiently at ambient temperature, and the typically high loss of materials at these frequencies. To make things worse, THz was largely eclipsed by the vast development of microwave and infrared technology. All these factors together restricted THz applications in the past to narrow specific niches mainly related with basic science like astronomy and spectroscopy [16], [17]. The classical sources of THz were based on bulky, expensive, and low efficiency solutions, including tube-based sources (carcinotrons, klystrons and inverse wave oscillators), and free electron lasers (FELs). As for the THz detection mode, it used to be based on bolometers in which cryogenic cooling was necessary in order to achieve good sensitivity levels.

However, a series of recent breakthroughs, such as more efficient THz sources working at ambient temperature like QCLs, or the improvement of classical microwave up-converters based on solid state multipliers gave rise to important advances. It is also worth mentioning the use of devices such as photoconductive antennas (PCAs), since they are the key elements on which commercial instruments like Terahertz Time Domain Spectrometers (THz-TDS) are usually based. A photoconductive antenna usually consists of a thin semiconductor layer with two metallic patches on it (dipole antenna) through which an optical pulse is incident. Because the laser photons have a higher energy than the energy gap of the semiconductor, they are absorbed by the film, generating photoconductors. These photoconductors are accelerated, producing a transient current that drives the dipole antenna and is ultimately re-emitted as a THz frequency pulse [18]. PCAs can also be used as THz detectors. Broadband THz radiation can also be generated by the use of non-linear properties in crystals. Optical rectification (OR), for example, refers to the development of a direct current (DC) or low frequency polarization when intense laser beams propagate through a crystal. This linear electro-optic effect describes a change in polarization of a crystal from an applied electric field [19]. When the applied electric field is delivered by a femtosecond pulse width laser, the mixing of different frequency components produces a beating polarization, which results in the emission of electromagnetic waves in the THz region [19]. Concerning the detection techniques, cheaper receivers such as those based on

photomixing or microwave heterodyne detection had a great contribution to the improvement of THz systems. An extensive variety of review articles treating the generation and detection of THz waves can be found in the literature [20]–[25]. These technological advances opened the way to several potential applications. In space applications, THz has a key role in cosmos research, among other fields, since much of the space radiation is in this band (cosmic background radiation) [26]. In addition, THz waves have very attractive characteristics for communications. The requested data rate in wireless communications will soon reach from 100 Gbit/s up to 1 Tbps, which will require systems with ultra-high bandwidths of several tens of GHz that are only available above 200 GHz. This is why both academia and the technology industry are focusing attention on the development of the so-called THz communications, which are expected to play a vital role in future wireless networks [27], [28].

THz radiation has some characteristics that make it a suitable technology for sensing applications, complementing or enhancing conventional solutions [29]–[32]. Unlike X-rays used in medical diagnosis, THz waves are non-ionizing and do not damage biological tissues, a property of utmost importance for health applications and critical for biodetection in general [21], [29], [33]. Moreover, THz waves are sensitive to weak resonances such as hydrogen bonds, van der Waals forces, and non-bonding (hydrophobic) interactions not detectable by classical MIR spectroscopy, offering new means for substance detection and opening new paths for identification of macromolecules like amino acids, proteins, RNA, or DNA in biological and/or medical investigation [29], [34], [35]. Furthermore, THz instrumentation gives both magnitude and phase information, allowing for a direct extraction of the refractive index and attenuation constant of the materials or substances under test. In addition, the strong sensitivity of THz waves to water is perhaps the most exploited feature in biomedical applications, and has been intensely investigated due to the promising perspectives it offers in cancer detection [36]–[40] and also in other diseases like otitis media [41]. Finally, THz waves can penetrate materials composed of non-polar molecules such as paper, plastic, and textile materials (opaque to visible and NIR waves), enabling easier security checks and safer inspection without direct contact between the operator and the measured substance. These properties have given rise to a powerful research line, and indeed, the list of biological applications of THz is extensive and in continuous development [29], [33], [42]–[45]. Although different technologies for THz sensors can be found in the literature, in this thesis, resonant structures based on metamaterials and metasurfaces will be proposed as ultrasensitive THz sensing devices for both thin film, biological, and chemical samples.

Detection techniques and instrumentation

Within the world of THz generation/detection systems, we can distinguish two main groups depending on the type of frequency conversion performed. On one hand, there are systems based on downconversion techniques, among which THz-TDS are placed. Regardless of the type of emitter/detector used, the operation of a THz-TDS works as shown in Fig. 1.4. The heart of any THz-TDS system relies on an ultrafast laser that emits a femtosecond pulse. This pulse is split at a beam splitter. One portion (“pump” beam) is directed to the THz emitter, generating a single-cycle of THz radiation. The THz radiation is collimated and radiated through the sample, and focused on the THz receiver. The other

portion of the pulse (“probe” beam), is directed through a variable delay stage before reaching the detector. This arrangement effectively samples the value of the THz field, with a resolution given by the laser width. By recording the detector value as a function of the delay time, the electric field (both magnitude and phase) of the THz radiation as a function of time is achieved.

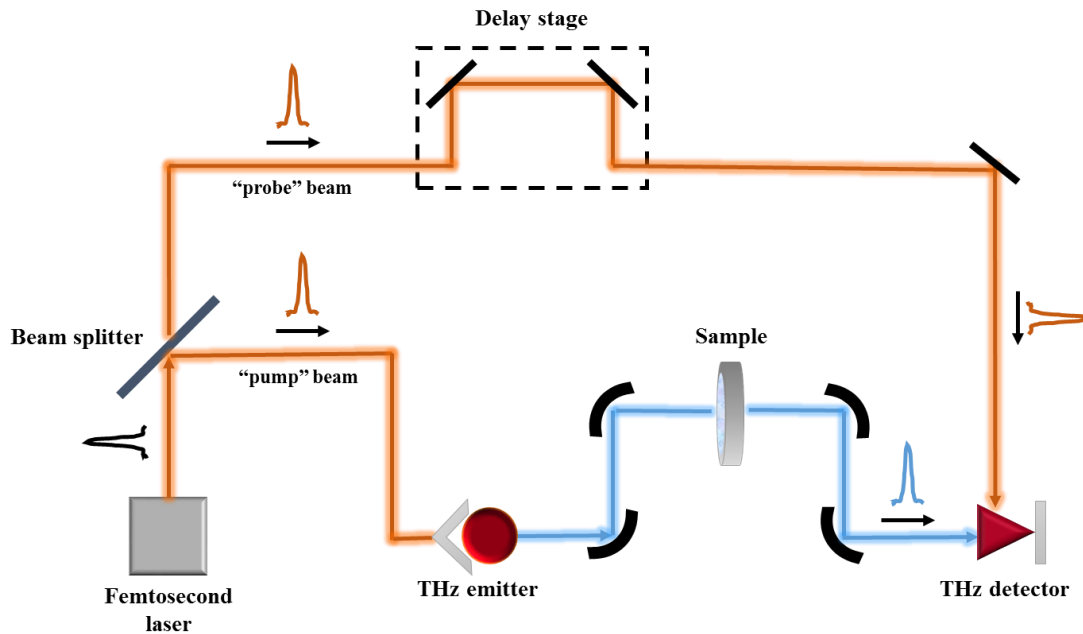


Figure 1.4: Schematic of a THz-TDS-based system and its components

Conversely, there are also upward frequency conversion systems, such as Vector Network Analyzers (VNAs). In a standard VNA, the underlying emission and detection mechanisms are based on microwave or millimeter-wave signals. The VNA generates an electromagnetic wave that is sent through the sample under test. The wave then reaches the detector, where the measurement results are used to calculate the complex transmission or reflection coefficients of the sample. For that, the VNA includes a tunable microwave source and a detector, frequency stabilization unit, data acquisition and data processing system. Commercial VNAs are typically limited to 60-70 GHz, so THz measurements require upconversion modules, usually by the use of multipliers. In this thesis, a VNA MVNA-8-350-4-based system has been used for the experimental measurements, which is shown at Fig. 1.5. In the MVNA, a millimeter-wave beam is generated by a corrugated horn antenna, and converted to higher frequencies by a Schottky diode harmonic mixer. Then, the signal generated goes through a quasi-optical bench formed by two pairs of elliptical mirrors that confine the signal beam and collimate it on the sample, avoiding diffraction. After that, another pair of mirrors focuses the beam into the receiving antenna, and the high frequency signal is processed in the heterodyne vector receiver.

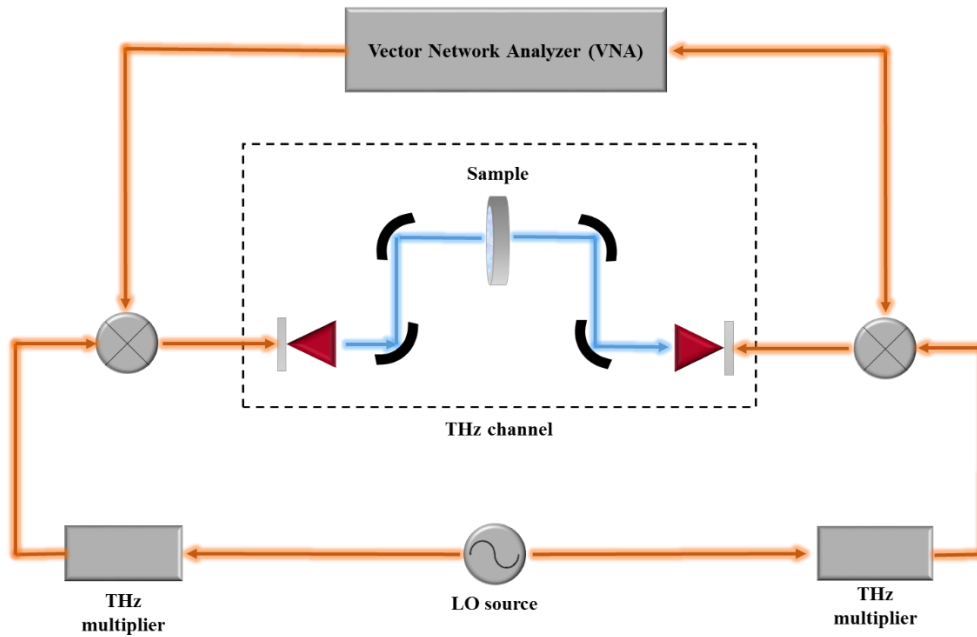


Figure 1.5: Architecture of the VNA-based system employed in this work

1.2. History of metamaterials and metasurfaces

The term metamaterials (MTMs) is a compound word and comes from the Greek prefix “*meta*” that means “beyond”. Therefore, the term “Metamaterials” refers to something that is beyond conventional materials, i.e. materials whose EM properties cannot be found in nature, but whose parameters can be engineered to obtain *à la carte* responses [46].

The first MTM definition was suggested by Roger M. Walser in 1999 as follows [47]: “*Metamaterials are macroscopic composites having a man-made, three-dimensional, periodic cellular architecture designed to produce an optimized combination, not available in nature, of two or more responses to specific excitation.*”. However, there is no universally accepted definition, and at the beginning, there was no consensus among different authors.

In a narrower sense, some consider a metamaterial to be a periodic structure whose unit cell period lattice maximum dimension is smaller than the wavelength with which it will work (sub-wavelength structures). In this way, the designed structure could be considered as an atom or molecule, and its properties could be modeled by means of constitutive parameters, permittivity (ϵ), and permeability (μ), exactly as it is done with atoms and molecules present in nature. Consequently, the principal idea of MTMs lies in using the same homogenization principle which consist in achieving the effective constitutive parameters (ϵ_{eff} , μ_{eff}) by introducing a periodic structure of unit cells known as meta-atoms (analogous to natural molecules and atoms) to obtain the global response of the metamaterial to EM waves (See Fig. 1.6).

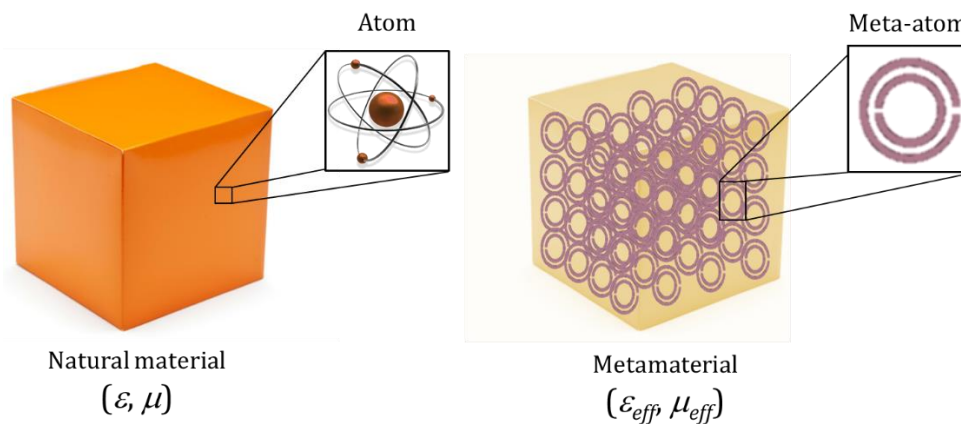


Figure 1.6: Schematic comparison between natural materials and metamaterials

Another important feature regarding MTMs is that their behavior on a global scale does not depend directly on the material composition, but rather on how these meta-atoms are distributed and structured in space. Thus, by changing the meta-atoms arrangement and/or geometry, it is possible to manipulate the effective parameters to obtain, for example, negative values of permittivity or permeability. In general, materials may be classified depending on the values of the real part of ϵ and μ into double-positive (DPS), epsilon-negative (ENG), double-negative (DNG) and mu-negative (MNG) media, as shown in Fig. 1.7.

The beginning of the study of exotic EM phenomena in artificial materials dates back to 1898, when Bose demonstrated, in the microwave range, a rotation of the EM wave polarization in structures with twisted geometries [48], now known as artificial chiral elements. Later in 1946 in the antenna community, Kock developed for the first time a lens antenna capable of focusing EM waves by using conductive plates (known as artificial dielectrics) [49].

However, the real interest in MTMs increased at the end of the 20th century, even though Veselago already theoretically predicted a medium with negative values of both ϵ and μ [50], and thus, a negative refractive index (n), in 1968. These characteristics lead to what we know as a left-handed medium (labeled as LHM in Fig. 1.7), in which the energy carried by the wave travels in the opposite direction as the wave propagates. In contrast, in almost all conventional dielectrics available in nature, the energy flows in the same direction as the propagation of the wave, giving rise to right-handed mediums (labeled as RHM in Fig. 1.7). Probably, the most fascinating consequence of LHM was its reverse effects, such as reverse Snell's law [51], or reverse Doppler effect [50].

Within a few decades, Pendry and his coworkers presented the first artificial MNG material. In its publication of 1999 [52], Pendry proposed the split ring resonator (SRR). The proposed single-cell SRR consisted of a pair of circular loops made of a non-magnetic metal, with partitions at opposite ends (shown in the fourth quadrant of Fig. 1.7). Since then, the SRR has been the most important and most frequently studied meta-atom exhibiting this type of response. Today, there is a wide variety of SRR designs: circular SRRs, nested SRRs, single SRRs, spiral SRRs, or squared SRRs, among others [53].

The first experimental demonstration of MTMs was carried out in 2000, when Smith and coworkers developed the first artificial DNG material (See Fig. 1.7) by combining a wire

medium (ENG) and a set of SRR elements (MNG) [54]. From then on, multiple theoretical and experimental works were reported, among which the proposal of the perfect lens concept introduced by Pendry [3], or the first experimental demonstration of a negative refractive index in microwaves by Shelby *et al.* [55], are worth mentioning. These experiments evolved these concepts to the development of “superlenses”, with the ability to overcome the diffraction limit [56]; or the invisibility cloak, which contemplates the possibility of guiding EM waves around an object, allowing its concealment [57]. In the context of cloaking, the experimental realization drew the attention of the scientific community. Even though the initial studies had imperfections with bulky devices that targeted mostly the lower-frequency part of the spectrum, principally microwaves [58], more experiments were later proposed in other EM regimes [59]–[61].

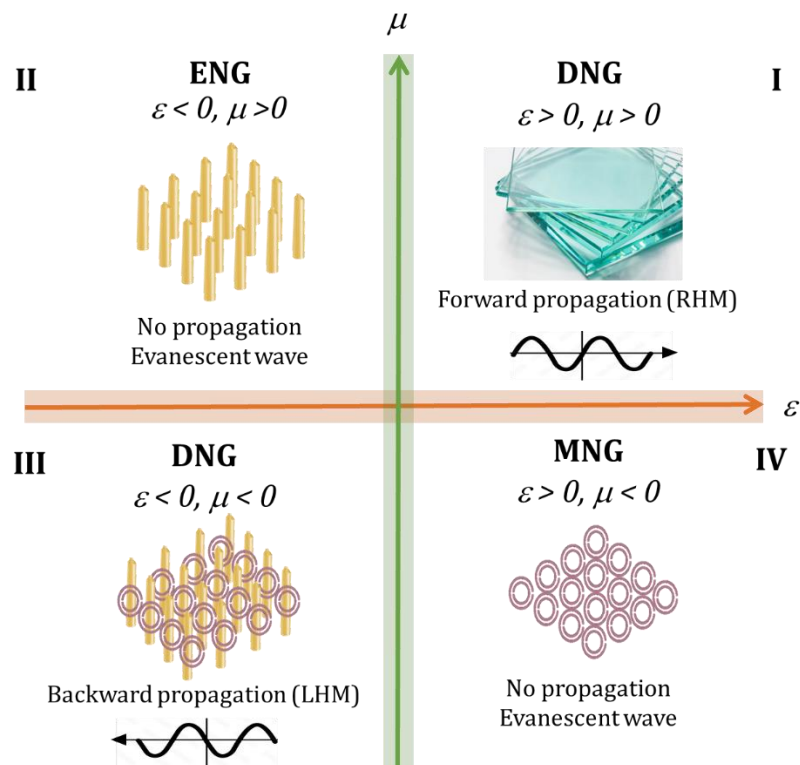


Figure 1.7: Materials classification in the ε - μ plane (real part).

Nowadays, metamaterials research has progressively leaned towards metasurfaces, their two-dimensional version. Hence, thin substrate slabs with an array of subwavelength resonating elements patterned on the surface are used instead of the volumetric structures used in the early days of its discovery. From this perspective, much more compact and manageable designs can be achieved [62]–[65].

Despite having appeared in some previous works [66], [67], the term metasurface acquired its maximum splendor after the work of Yu *et al.* in 2011, with the design of a two-dimensional array of non-uniform and gradient metasurfaces consisting of an array of V-antennas, able to modify the phase variation and steer the incident wave in a desired manner. This made it possible to break the limitations of standard optical components, which rely on the gradual accumulation of phase along the optical path to change the wave front of the propagating light, and to revise Snell's laws of reflection and refraction to

rewrite and rename them as generalized Snell's laws. Since then, metasurfaces have given rise to a new wave of revolutionary applications in the whole EM spectrum like ultrathin carpet cloaks [61], antireflection temporal coatings [68], analog computing [69], or even time-dependent metasurfaces capable of changing the direction of the energy propagation of EM waves, known as temporal aiming [70].

Regarding the THz region, a large number of THz metasurfaces have also been proposed for several applications. According to [71], THz metasurfaces can be divided into three categories depending on its modulation function: spectrum modulation, wavefront modulation, or polarization modulation.

Based on the electromagnetic resonance, metamaterials provide an effective way to manipulate the EM spectrum. Metasurfaces for spectral modulation can be used as filters, absorbers, or sensing devices for the modulation of THz transmission, reflection, or absorption spectrum. At the top of Fig. 1.8. are plotted two examples of spectrum modulation metasurfaces consisting of a tunable multiband THz absorber composed of a kind of periodic array square graphene ring with a Jerusalem cross graphene sheet (top left) [72]; and a wide band metasurface-based band pass filter working in the THz defined based on random hill climbing algorithm (top right) [73].

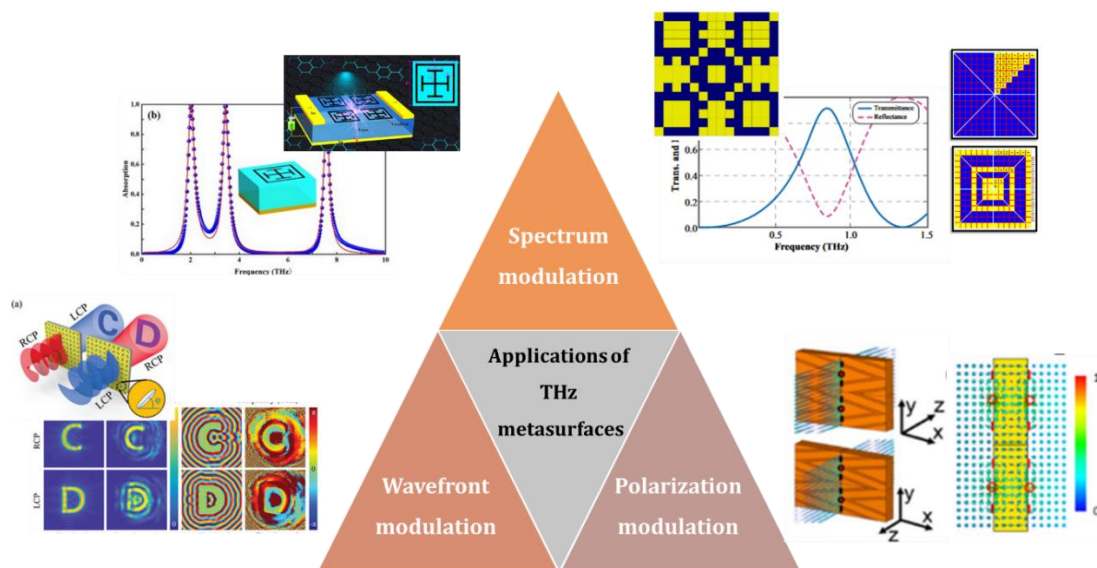


Figure 1.8: Examples of different applications of metasurfaces working on the THz band, including a perfect metasurface absorber [72] (top left), a digital metasurface filter [73] (top right), a Polarization selective amplitude holographic multiplexing metasurface [74] (bottom left), and a zigzag metasurface acting as a THz Half-Wave Plate device [75] (bottom right).

Since Yu *et al* proposed the generalized law of reflection and refraction [51], more and more metasurfaces used for wavefront modulation have been proposed and verified [76]. The basis of wavefront manipulation by a metasurface consist of the capability to modulate the intensity and phase distribution of THz waves. There are several wavefront modulation applications, among which can be highlighted focusing, special beam generation, or holographic imaging (see Fig. 1.8), to name a few [71].

Regarding functional metasurfaces, polarization modulators are also of great importance, allowing us to shape the polarization state of THz waves. In this category, many devices have been proposed such as polarizers, polarization filters, converters, or wave plates, among others. Fig. 1.8 shows, at the bottom right corner, a schematic of a quarter-wave plate (QWP) designed in [75] based on a zigzag metasurface to convert linear polarization in circular one in a very compact design.

In addition to those exciting realizations, metasurfaces are emerging as true game changers in the quest for designing ultrasensitive sensors all along the electromagnetic spectrum but with special relevance at THz frequencies.

In this thesis, we focus on the design of metasurfaces operating in the THz band, for sensing applications. In the following chapters, different designs for sensing thin-films, biological and chemical samples are presented and characterized.

1.3. Structure of the thesis

The objective of this thesis is to provide a detailed description of the main results obtained in the research work on MTMs-based sensing devices in the THz band and the use of spectroscopy techniques in the IR spectral region carried out by the author, covering the following main issues:

- Numerical and experimental design and study of different MTM-based structures for sensing purposes, covering thin-film, biological (fungi), and chemical (Polycyclic Aromatic Hydrocarbons, (PAH)) sensing.
- Geometric modification of meta-atom-based devices with the aim of improving the detection limit and sensitivity of these structures.
- Application of MIR spectroscopy for chemical analysis of oxidative compounds in foal meat.

Since this thesis has been conceived is a compilation of papers published in different journals throughout the thesis, this document has been structured in such a way that each chapter presents a review of the theoretical aspects and the state of the art of each topic to be addressed, followed by the article published by the author, including a small introduction containing the most striking results and conclusions of each work.

Chapters II to VI are devoted to the work carried out during these years. The published articles and a discussion for each of them are presented.

- Chapter II and III - THz Metasurfaces and Sensing: Labyrinth Metasurface Absorber

[PAPER A] - *Labyrinth Metasurface for Terahertz Thin Film Sensing*

A so-called labyrinth metasurface sensor working at THz is presented. The intricate geometry of the design leads to a high electric field confinement all over the structure surface, leading to ultrasensitive performance for thin-film sensing applications. The structure is coated with extremely thin analytes with thicknesses

varying from 24nm to 345nm of tin dioxide (SnO_2) and its sensing capabilities are numerically and experimentally evaluated.

[PAPER B] - *Labyrinth Metasurface for Biosensing Applications*

The same labyrinth metasurface is now rescaled in frequency to extend the previous concept towards biosensing applications, evaluating the performance of the labyrinth as a fungi detector.

[PAPER C] - *Metageometries for PAH Detection in Food Systems*

The labyrinth metasurface is, as a final step, experimentally tested for Polycyclic Aromatic Hydrocarbons THz detection and identification, with a design able to detect different concentrations and distinguish between different compounds at the same concentration.

- Chapter IV – Alternative Metasurface Designs

[PAPER D] - *Tripod-Loop Metasurfaces for THz-Sensing Applications*

Different devices based on metaatoms and called "tripod metasurfaces" are proposed and studied as thin film sensors. We carry out a comparison between different types of tripod metasurfaces by studying metastructures with increasingly complex geometries: from simple tripod metasurfaces formed by solid blades (arms) to a hollow tripod metasurface where it will be shown that the confinement of the electric field is much higher.

[PAPER E] - *THz Sensing with Anomalous Extraordinary Transmission Hole Arrays*

We demonstrate the superior performance of a different resonant regime of Subwavelength Hole Array (SHA) metasurfaces called anomalous extraordinary transmission (ET) by performing a numerical and experimental study of its behavior in thin-film sensing applications. First, a numerical analysis for the sensing behavior for both regular and anomalous polarizations in ideal structures is performed. Finally, we present a numerical and experimental analysis of the sensing capabilities of several SHAs loaded with dielectric films of different thicknesses, so that some of the structures support the anomalous ET resonance, and others are in the limit or do not support it at all.

- Chapter V – MIR spectroscopy for food quality determination

[PAPER E] - *Lipid and Protein Oxidation Marker Compounds in Horse Meat Determined by MIR Spectroscopy*

This work extends the study of marker compounds of lipid and protein oxidation in foal meat, using ATR-FT/MIR technology. Marker compounds were extracted from 23 foals and their absorbance spectra were measured to establish prediction models between them and the classical analysis of compound quantification. The same process is performed on raw meat samples, in order to determine if a previous extraction of the marker compounds is preferable before performing their MIR analysis.

Chapter VI contains some general conclusions of the presented work, as well as the current and future research lines.

To conclude, the list of references are given, followed by the author's merits achieved during this time.

Chapter II: THz Metasurfaces and Sensing

As explained in Chapter 1, THz radiation presents interesting characteristics that make it a suitable option for many applications, among which sensing can be highlighted. Nevertheless, a challenge still open is how to achieve reliable sensing when the measured sample amount is very small [77]. In this situation, the substance under test simply does not interact sufficiently with the electromagnetic waves inducing negligible changes in the response and making detection extremely difficult or even impossible with conventional techniques. This problem, which arises in every sensing application, is especially serious in the THz band because of its relatively long wavelength. This type of measurement is called thin-film sensing and becomes indispensable in the characterization of dangerous samples (i.e., toxic substances, explosives, etc.) that use very small amounts of the substance, or when the samples are functionalized because monolayers are easier to process as thin-films, such as in biological and chemical sensing.

In this context, metamaterials (and more specifically, metasurfaces) have emerged as true game changers in the quest towards designing ultrasensitive sensors all along the EM spectrum but with special relevance at THz frequencies. The key idea behind this type of sensors is to engineer (usually metallic) patterns with small details (slots or patches) to produce a strong field concentration at localized spots under an external source illumination. This intense field confinement enhances light-matter interaction with the analyte (i.e., the substance under test), giving rise to a strong change in the spectral response.

In this part of the thesis, we will summarize the advances achieved in THz sensing using metasurfaces from both a historical and application-oriented perspective. The initial part, is dedicated to the important topic of thin-film sensing using metasurfaces, due to its historical importance, as it was crucial in launching the topic and merging metamaterials and metasurfaces with sensing applications. Then, several strategies are highlighted, starting from the classical SRR arrays and the evolution of the topic towards more sophisticated structures such as metageometries. Then, we will focus on the important topic of biological sensing based on metasurfaces at THz frequencies and, finally, our contribution to this field will be presented, with the design of a metasurface with an intricate geometry, which we have named as *Labyrinth metasurface*.

2.1. Motivation of Thin-film Sensing

The characterization of very thin homogenous samples by THz radiation is attracting an increasing interest from the scientific community in recent years, especially in areas where measuring substances in a thin-film form becomes essential, as in biomedicine or biological sensing. In addition, thin-film sensing becomes crucial in situations where traditional THz sensing methods, such as THz-TDS, do not reach enough sensitivity to obtain sufficiently good results. Some of these circumstances, as mentioned in [77] are: when the amount of sample is very small (for instance, when our desire is to characterize biological samples, such as DNA, microorganisms, or when manipulating dangerous samples); when the sample is easier to be processed in thin-film form; when a thin-film sample has different properties from its bulk counterpart; when one can obtain better sensitivity using a thin film; or when the sample characterization is complementary to other thin-film techniques, such as atomic layer deposition.

Although different solutions have been proposed (resonators, plasmonic structures, etc.), metasurfaces have emerged as a revolutionary alternative due to their exciting properties. Metasurface-based sensors have been crucial in alleviating one of the biggest problems in THz thin-film and biological sensing, which is the stark difference between the typical analyte thickness or size of microorganisms ($\approx 1 \mu\text{m}$), and the wavelength at THz (≈ 10 to $1000 \mu\text{m}$), that makes this radiation largely myopic to these small details. Thus, classical THz spectroscopy of thin-film analytes and microorganisms needs thick samples or many individuals and the response is taken as an average, making it very difficult to distinguish subtle differences in complex film samples, not to mention the identification of a single microorganism in biosensing applications. Metasurface biosensors hold the promise to overcome these limitations taking advantage of the unprecedented freedom to engineer the metasurface parts properly. In addition, in metasurface devices, when radiating with THz waves on very thin samples, small changes occur in the spectral response with respect to the empty structure.

Therefore, one of the biggest challenges in thin-film sensing is to obtain designs with high sensitivity and figure of merit (FOM), which are the two main parameters for evaluating the quality of a sensing device. Although it can be defined in multiple ways and there is not a single universally accepted definition, generally speaking, the sensitivity represents the variation in frequency (or, in some cases amplitude) in the spectral response of a sensor device when an analyte (i.e., the substance under test) is deposited on it. Generally, a weak point of THz metasurface sensors literature is the lack of a universally adopted sensitivity metric, making it difficult to compare the performance of different devices. It must be taken into account that in the most common definitions, where the sensitivity depends on both the frequency shift and analyte thickness, the analyte refractive index is not taken into account, so analytes with higher refractive index tend to give better results. With the aim of clarifying this issue, here a definition that takes into account all these parameters is proposed, and the frequency sensitivity (FS) is defined as:

$$\text{FS} = \frac{\Delta f}{h_a n_a} \quad (2.1)$$

where $\Delta f = f_a - f_0$ with f_a the resonance frequency at each analyte thickness, h_a ; f_0 the resonance frequency of the empty structure; and n_a the refractive index of the analyte. In some occasions, the parameter used to sense is the change in the amplitude of a peak or a dip in the spectrum and the sensor quality is measured with the amplitude sensitivity, AS.

In our definition, we consider again both the analyte thickness and refractive index as shown in equation 2.2, where ΔA is the amplitude variation.

$$AS = \frac{\Delta A}{h_a n_a} \quad (2.2)$$

The FOM is a more accurate parameter defined as the ratio between the sensitivity and the full width at half maximum (FWHM). This parameter usually gives a better measure of the performance of a sensor because not only it is important to have a noticeable frequency shift in the spectral response but also to have resonances with narrow FWHM (narrow peaks or dips) to minimize the overlapping between the detection thresholds.

2.2. Evolution of metasurfaces towards sensing applications

The first metasurface design reported in the literature specifically used for thin-film sensing applications was proposed by Driscoll *et al.* in 2007 [78]. Their design consisted of a square periodic matrix of gold SRRs patterned on a silicon (Si) substrate of thickness equal to 1 mm and coated with a thin layer of 6 μm of benzocyclobutane, used as a low-loss adhesion layer for the metallization. The empty metasurface was experimentally measured in an Fourier-Transform Infrared (FTIR) spectrometer using TE-polarized radiation impinging at 45° and showed a resonance dip at 1.20 THz corresponding to the magnetic mode of the SRR (i.e., its fundamental quasi-static resonance) [79]. To evaluate the sensing performance, the metasurface was then covered with an homogeneous layer of Si nanospheres many times thinner than the skin depth of THz radiation, and a redshift of 0.05 THz was observed in the spectral response with respect to the empty structure. As the authors noted, the solution contained an insignificant amount of Si (they estimated it below 1 ng), so small that it would be undetectable using a standard transmission-amplitude experiment.

The SRR metasurface allowed the detection by transforming the typical transmission-amplitude change scheme to a new paradigm, where the parameter that changes is the spectral location of the metasurface resonance frequency (see Fig. 2.1.), which is often much more accurate.

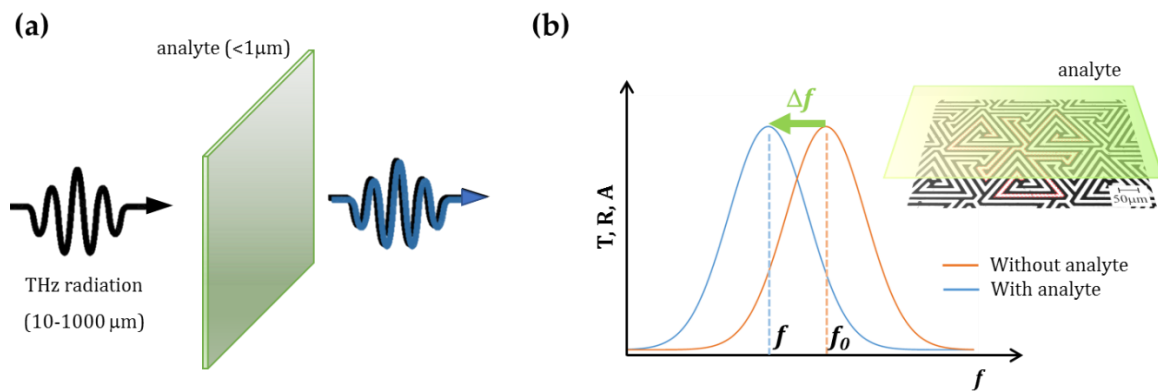


Figure 2.1: (a) THz thin-film sensing scheme and sample interaction with traditional spectroscopy methodologies. (b) THz thin-film sensing scheme using metamaterials.

This work was soon followed the same year by another one by Debus and coworkers [80], who proposed a metasurface made of asymmetric double split ring elements of 50 μm radius and two gaps working at 0.875 THz. The rationale behind this new particle was to break the symmetry by adding a second gap in the ring, opening the possibility to excite additional resonant modes. The study was based uniquely on numerical simulations, and it was observed that when the metasurface was coated with a dielectric material of permittivity 3.2 (typical for organic systems) and thickness of 10 nm (corresponding to a typical monomolecular film) covering completely the area of the structure, a redshift of 0.005 THz appeared in the spectral response of the reflection coefficient magnitude. However, the most interesting aspect of this work was the observation that placing the analyte only in the ring gaps, which are the zones of highest electric field concentration, led to a shift of 0.004 THz, comparable to the previous case but using a much smaller amount of material. Obviously, this strategy is optimal in terms of sensitivity, as it leads to a similar performance with a significantly smaller volume of analyte.

Both works were pioneering in the emerging topic of thin-film sensing using metasurfaces and, indeed, the strategy since then has evolved but using practically the same principles. Since then, numerous studies have been carried out with respect to metasurfaces, which have revealed some key insights for the design of more efficient devices.

O'Hara *et al.* performed in [81] a systematic study of the sensing performance of SRR metasurfaces as a function of the dielectric thickness. The SRR elements were made of aluminum with thickness 200 nm laying on 0.64 mm thick Si substrates, with a photoresist layer deposited on the top. Although its thickness was gradually varied up to 90 μm , it was observed that the frequency shift saturated at approximately 16 μm and no further significant shifts were observed afterward. This suggests that a critical feature in the sensing performance of a metasurface sensor is the effect of the substrate permittivity and its thickness.

Intending to better understand the concept of frequency shift saturation, we have plotted the frequency behavior of one of the structures designed in this thesis [82], that will be fully studied in further sections. Fig. 2.2 shows the reflection coefficient of the empty metasurface (black line), and when it is coated with different analyte thicknesses, ranging from a few nanometers to 40 μm . Panel (b) represents the frequency shift obtained from each reflection coefficient. As shown there, for very small values of analyte thickness the variation between different thicknesses is quite high (greater curve slope). However, as the analyte thickness increases, it reaches a point where it saturates (orange area), being practically impossible to discern between thicknesses from that point on.

This was addressed in detail subsequently in [83] by analyzing two types of planar THz metamaterials manufactured on ultrathin silicon nitride (SiN_x) substrates and bulk Si substrates. The main idea behind this study was that high-permittivity substrates contribute a large capacitance to the resonator, hiding the spectral variation (typically a shift of a dip or peak) induced by the changes in the capacitance due to the analyte. In the thorough investigation done in that work, it was demonstrated that ultrathin substrates led to an order of magnitude improvement in the sensitivity of planar THz metasurface sensors.

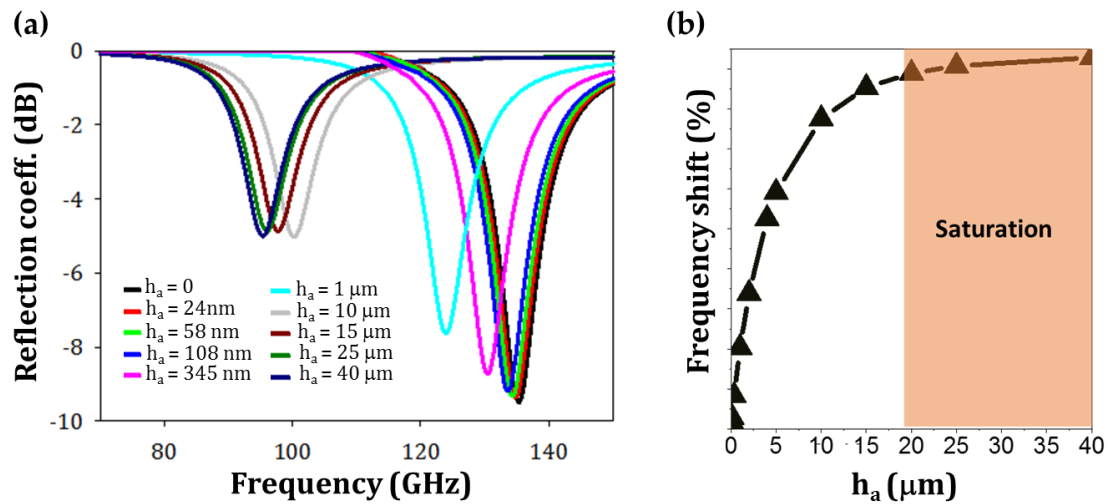


Figure 2.2: (a) Reflection coefficient when the metasurface is loaded with different analyte thicknesses, from 0 to 40 μ m. (b) Frequency shift representation as a function of the analyte thicknesses, with saturated region in orange.

A challenge in reliable sensing is to achieve a high quality factor resonance and hence improve the sensitivity. A problem with the typically used far-field setups is that they require a minimal area of analyte deposited on the metasurface. This is even worse due to the fundamental limitation imposed by diffraction which restricts the smallest possible beam waist size to approximately half-wavelength in free space, although in practice the beam waist is usually larger. A direct consequence of this setup is that one needs a large volume of analyte to cover fully the area of excited resonators. This collective excitation causes resonance broadening due to enhanced scattering, decreasing ultimately the quality factor. This limitation was overcome by Withayachumnankul and coworkers in 2012 by proposing a near-field experimental setup using a SRR metasurface sensor operating at 0.4 THz [84]. The main concept is that with a near-field setup only a small number of resonators participate in the resonance process and therefore the analyte area can be reduced. The improvement of the quality factor comes as a consequence of the weak near-field interactions among a reduced number of resonators, leading to an effective sub-diffraction sensing capability. Putting these ideas into test, a successful detection of a thin-film with a thickness of only $\lambda/375$ was achieved.

In a further step towards improving the performance of THz metasurface sensors, it was found that absorbers working in reflection have better performances than metasurfaces working in transmission. This was firstly analyzed in detail in [85] by comparing the behavior of metasurfaces working in absorption and transmission. The basic principle of operation of the proposed devices was based on the concept of perfect metamaterial absorbers that evolve from metamaterial absorbers and whose main mission is to minimize the reflection, enhancing this way the absorption by enforcing impedance matching to free space. At the same time, transmission can be avoided by using a metallic ground plane. With this configuration, the electromagnetic field can be locally stored inside the structure, thus improving the interaction with the analyte under test. Another advantage of the use of a ground plane is that it prevents the electric field decay inside high-index substrates leading to an enhanced interaction between the incident wave and the analyte. To date, similar studies have confirmed the effectiveness of working in a reflection configuration [86], and designs based on perfect absorbers are gaining increasing support in the scientific community, allowing multispectral and flexible designs to be obtained [69], [86]–[89].

Aside from the previously mentioned near-field operation [84], another strategy to increase the quality factor of metasurface sensors is based on the use of high-order resonances supported by asymmetric resonators following the strategy already pointed out in one of the pioneering articles [80]. This idea was further followed in [90] by Singh *et al.* who achieved high quality factor sensing by exploiting quadrupole and Fano resonances excited by breaking the symmetry of the metamaterial unit cells. The symmetry breaking was realized by an array of asymmetric split ring resonators made of aluminum, 200 nm thick, laying on a high-resistivity Si substrate, 0.5 mm thick, by using photolithography. The asymmetry in the resonators was introduced by displacing the lower gap 5 μm from the central vertical axis. The characterization of the structure was done using a broadband THz-TDS working in transmission mode at normal incidence. Depending on the polarization of the incident wave, either the quadrupole or the Fano resonance could be excited. The first one happened at 1.14 THz, whereas the second was located at 0.52 THz for the empty structure. It is worth mentioning that the quadrupole resonance was tuned to coincide with the onset of the first diffraction order to enhance the quality factor. Interestingly, the performance of the Fano resonance was found to be better suited for sensing purposes, as it led to higher sensitivity values. This important aspect could be attributed to the different electric field mode profiles in the capacitive gaps of the resonators. In a subsequent step, a simulation analysis reducing the Si thickness was carried out to evaluate the effect of the substrate. With this study, it was noticed that the sensitivity of the Fano resonance could be enhanced by a factor of two and that of the quadrupole resonance by a factor of three when the substrate thickness was below 20 μm for a 1 μm thick analyte. This can be explained because of the stronger interaction of the analyte layer with the electric field in the gaps when the metasurface is implemented on ultrathin substrates. Nevertheless, high quality factor resonances are not restricted to asymmetric structures. Rather, a narrowband response (and hence high quality factor) can be found in simple symmetric structures but introducing the asymmetry in the excitation by impinging, for instance, at oblique incidence [91].

The path of Fano-based sensing was further extended using more refined and disruptive concepts such as toroidal resonances. Concretely, Gupta *et al.* presented in 2017 a metamaterial device based on a planar toroidal dipole [92]. Originally, toroidal resonances are related with currents flowing on a torus surface. To implement the toroidal characteristic in two dimensions, Gupta *et al.* proposed a 2D metasurface made of mirrored asymmetric split ring resonators coupled through a toroidal moment due to an anti-aligned set of magnetic dipoles. In the context of sensing platforms, an interesting feature of toroidal resonances is that they have a remarkably high quality factor. Hence, the toroidal metasurface introduces an improvement in both sensitivity and FOM with respect to typical sensing metasurfaces based on traditional uniform (as opposite to mirrored) Fano resonator arrays.

There are currently many examples of THz metasurface sensors with very good performance in thin-film sensing applications, able to achieve high sensitivity as well as FOM values for thicknesses as fine as a few tens of nanometers. However, those designs suffer severe restrictions when the thickness of the thin-film analyte falls below 10 nm due to the large dimensional difference between the thickness and THz wavelength. This fact renders metasurface designs based on conventional photolithography unable to detect extremely subwavelength analytes due to the insufficient interaction between the electromagnetic wave and the material.

To enhance this interaction, one should be able to squeeze the electric field within a very small volume and implement environments with a high electric field strength, increasing

the light–matter interaction. In fact, this is at the core of the metasurface sensors discipline and the main reason for their success all along the electromagnetic spectrum. The problem is that it is intrinsically difficult to create sub-nanometer gaps uniformly distributed on a length scale of a few dozen microns using conventional manufacturing techniques.

This limitation can be circumvented by other manufacturing techniques different from classical photolithography, such as the one known as atomic layer lithography (ATL). ATL is based on atomic layer deposition and able to produce sub-nanometer details in large areas, of the order of millimeters or even centimeters, by the combinations of electron beam lithography (EBL) or ion beam milling, and atomic layer deposition (ALD). The key aspect of ATL is that the sub-nanometer dimension is decoupled from the rest of the pattern. This way, it is possible to manufacture structures in the centimeter-scale with gaps in the atomic scale [93], [94].

The first report on this type of manufacturing was presented in [93] and, thanks to the ultrathin gap created, the authors were able to increase the local surface-enhanced Raman scattering by a factor of 10^9 when the nanogap size was 5 nm.

A drawback of the previous structure is that the elements were hollow (i.e., slits or holes) and the nanogap was placed in the perimeter of the aperture (i.e., in the case of the holes is a narrow ring slot around the hole). Therefore, transmission measurements suffered from a significant background due to the direct transmission through the central aperture. In addition, the structural dimensions were not suited for THz frequencies. Those issues were addressed in [94] by implementing a new planarization scheme to obtain structures where all the apertures were nanogaps, avoiding any other hollow. This way, a structure consisting of metallic islands separated by alumina nanogaps was obtained. It is important to remark that this manufacturing technique can be applied to large areas because the overall footprint is defined by standard lithography, whereas the nanogap size depends uniquely on atomic layer deposition, which can have nanometer resolution. Applying this method to the THz characterization of the structures, an extraordinary field enhancement factor as high as 25 000 was estimated from the experimental measurements for a 1 nm nanogap structure.

These more complex manufacturing techniques open interesting avenues in thin-film sensing applications with exquisite sensitivity, as demonstrated in many works and reviews available in the literature [95]–[99].

In summary, new manufacturing techniques, among which ATL stands out, allow the design of increasingly complex structures based on nanogaps, which translates into the possibility of detecting ultrathin films with excellent sensitivity values and field confinement. This opens the door to designs capable of detecting materials with atomically thin thicknesses, such as graphene, or some biological samples. Nevertheless, we have seen that these techniques are much more complex, time-consuming, and expensive than conventional procedures. In this thesis, all the designs have been manufactured by classical procedures, and tried to achieve higher sensitivities by focusing on the pattern geometries.

2.3. Biological Sensing with Metasurfaces

Biological sensing has always attracted a great interest from the scientific community, for obvious reasons. The fundamental process for chemical analysis and medical diagnosis is based on the specific interaction between molecules. THz radiation has expanded the possibilities of biomolecular detection, thanks to its sensitivity to weak intermolecular interactions, giving access to significant information about the chemical composition of

substances and/or biomolecules not available using traditional detection methods such as IR spectroscopy. In addition, THz radiation has proven to be a non-invasive, contactless, and non-ionizing technique innocuous to living organisms exposed to it. Moreover, THz radiation is very sensitive to water, making it a good option for cancer and tumor treatments, since the tumor cells contain different aqueous percentages than healthy cells. Hence, nowadays THz technology stands out as a competitive option for replacing or complementing other techniques that have proven to be harmful, such as X-rays. This facts, added to its strategic location in the middle of the EM spectrum that allows for an extrapolation of concepts borrowed from other bands, has led to a fast technological development of biosensing devices in this range, and the biological-related THz research activity has spread throughout the world covering a wide variety of fields such as diagnosis of diseases [100]–[103], detection of protein concentrations [104]–[106], DNA sequencing [107]–[109], detection of cancer cells and tumors [39], [110]–[113], or detection of microorganisms [114]–[118], among others. In this regard, metasurfaces are probably one of the most successful realizations, as they respond to changes in the refractive index of the device, a measurement that is relatively easy and cheap to perform, allowing for a quantitative and kinetic measurement of molecular interactions [119]. Fig. 2.3 shows a scheme with different real biosensing applications of THz metasurface-based devices available in the literature. Further information can be found in [45].

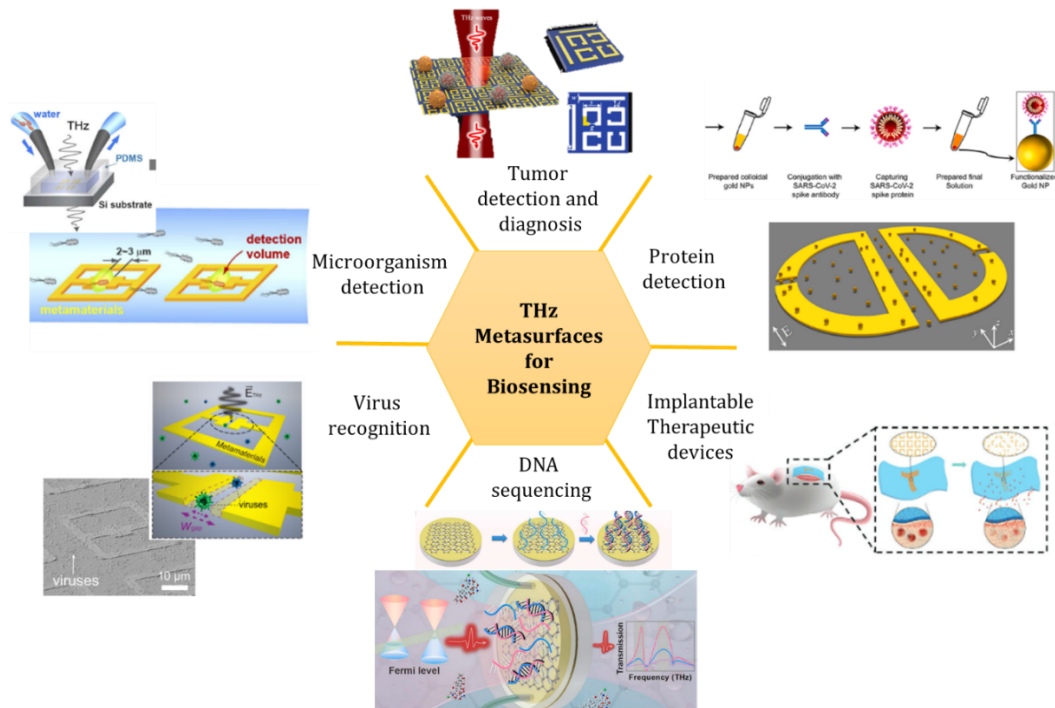


Figure 2.3: Examples of different biosensing applications using THz metasurfaces such as tumor detection and diagnosis [112], protein detection [104], skin implantable devices [120], DNA sequencing [107], virus recognition [121], and microorganism detection [116].

A pioneering antecedent of metasurface biosensors can be found in the infrared range in the work of Brolo *et al.* who in 2004 proposed the use of arrays of nanoholes in a gold film to monitor the binding of organic and biological molecules to the metallic surface [122]. This line was continued at THz by Debus *et al.*, in the report already discussed in the

previous section [80]. There, a thin layer of 10 nm of a dielectric slab with a permittivity typical of organic systems was used as analyte material, with good results in terms of sensitivity. From that work to the present, many articles have been published in this field. For example, a new method of analyte deposition by 3D printing was used in [123] to develop a label-free biosensor based on the resonant transmission of a metallic mesh with the objective of detecting a small amount of protein horseradish peroxidase. The obtained results demonstrated that the designed device could achieve a sensitivity equal to that of a conventional method based on the use of antibody-labeled horseradish protein. These results gave an evidence that metasurface sensors at THz are a cost-effective alternative for protein detection in biomedicine applications.

As in thin-film applications, the geometrical design and effect of the substrate on the performance of metasurface biosensors is also relevant in biosensing and thus it has been exhaustively analyzed. One well-known study that is often cited in research on substrate effect is that of Wu *et al.* (2013), where two different substrates of Si ($\epsilon = 11.56$) and quartz ($\epsilon = 4$) were compared in a label-free and specific sensor for streptavidin-agarose [124]. This sensor was fabricated by the functionalization of octadecanethiols and biotins in the THz range, and its behavior was numerically and experimentally tested by the study of the first two resonant modes present in the designed metasurface. Interestingly, it was shown that the frequency shift towards lower frequencies was larger in the case of the second dip, and this was more evident for the quartz substrate. These results highlight the importance of the choice of the substrate materials when designing a biosensor, corroborating the findings of the thin-film metasurface sensors.

The previous papers, among others, led to a surge of interest in the possibilities of metasurfaces for biosensing. Since then, numerous studies have been carried out in order to detect multiple types of substances, such as proteins, amino acids, and sugars. Among all these substances, there are some that present special interest for health. For example, carbohydrates perform essential roles in most living organisms in energy metabolism processes, or cell to cell communications. Nevertheless, they lead to an increment of the blood sugar, and it is very important to have control on the intake amount to avoid hyperglycemia and illnesses related to it. This control becomes even more important in patients suffering from carbohydrate-specific diseases such as diabetes. Therefore, finding new ways to detect and differentiate sugars is of great scientific and practical interest. This is the case of the work presented in [125] where a nano-slot antenna array working in the THz range was presented for selective carbohydrate detection and discrimination method, able to discern molecules with concentrations ranging from hundreds to tens of moles. In this work, two different antennas were designed to selectively detect fructose and glucose respectively, by matching the fundamental antenna resonance with the absorption peak of each substance. These results give evidence of the fact that these antennas, specifically designed for a certain sugar molecule, work properly for the targeted molecule with strong absorption features at the design frequency, but are insensitive to other molecules. Therefore, this type of sensor presents an efficient way to isolate molecules of interest by simply engineering the antenna at the optimal frequency.

As we have seen up to now, the detection of some biomolecules is of great importance as they might be related to specific diseases and an early identification can be crucial to treat them in time. Antibiotics have revolutionized healthcare and are one of the main factors for the rise of life expectancy during the last century. In fact, they are essential in the treatment of infections and fighting bacteria or other pathogenic microorganisms. Recently, an antibiotics-loaded flexible metamaterial device as a degradable antibacterial skin patch was designed by Sun and coworkers, for controlled drug release when doped with appropriate

pharmaceutical molecules [126]. However, an excessive use of antibiotics can generate bacterial resistance decreasing the treatment effectiveness leading ultimately to a serious health risk. In order to keep a safe health environment, a proper control of the residues of antibiotics present in food becomes of vital importance. In recent years, it has been shown that metasurfaces are an interesting option in this field, with high sensitivity in the detection of some kinds of antibiotics [105], [127], [128].

Aside from the detection of molecules, drugs, or proteins, the study and sequencing of DNA and RNA has become very important in recent years. To begin with, many human genetic diseases are caused by single-base mutations in the genetic information. Since DNA molecule mutations are extremely difficult to differentiate and the existing methods are invariably complex and time-consuming, new alternatives based on THz devices and metamaterials are being proposed nowadays [107], [108]. Moreover, the study of transgenic foods has also become very important, and there is a great debate about whether its use is beneficial or not for human health. Transgenic foods are those that have been produced from an organism modified by genetic engineering and to which genes from another organism have been incorporated to produce the desired characteristics. According to the World Health Organization (WHO), the transgenic foods available in the market have passed risk assessments and are unlikely to pose health risks. However, it seems important to perform more exhaustive studies and monitoring, field where metasurfaces are also emerging as a good alternative [129], [130].

Microorganisms such as fungi, bacteria, or viruses are the cause of many human diseases, so the demand for tools to detect them in a quick and effective manner has grown and is continuously increasing over the years. Usually, the methods used for this purpose are very slow due to the growth time of the bacteria (from days to weeks). Although some techniques, such as molecular methods or mass spectrometry, have managed to reduce the time necessary for correct detection, they are still relatively complex and difficult to apply in the point-of-care.

Metasurfaces operating in the THz regime are an emerging alternative in this regard, as they have already shown a great potential in high-speed and on-site detection of microorganisms. One of the first examples was found in 2014, where a metasurface-based sensor for the high-speed detection of live microorganisms was numerically and experimentally studied [115]. The structure proposed consisted of metallic arrays of a square ring with a gap in the center deposited over a Si substrate. The advantage of this type of structure with respect to direct detection without a metasurface is that the size of the microorganisms is very similar to the micro-gaps of the resonators. In this way, the microorganisms that are placed in the metallic gap will undergo a high interaction with the incident wave due to the high electric field intensity in those areas, when the metasurface is at resonance, causing important changes in the frequency response. In the same work, a study in a dry environment was conducted varying the number of microorganisms (N) of penicillin in the gap area, from 0 to 5. Several transmission spectra were obtained, obtaining in all the cases a measurable frequency shift. As the authors mentioned, one of the advantages of sensing microorganisms is that they usually can be cleaned. Once the measurement of the resulting spectrum was obtained, the structure was treated with a fungicide, and the resulting spectrum returned to the original, showing the possibility to reuse metasurface sensors [115]. Since then, this has been addressed by the scientific community, and new designs for sensing microorganisms such as bacteria and/or fungi have been presented in recent years [116]–[118].

Even though it has been demonstrated that properly designed metasurfaces are capable of efficiently detecting microorganisms such as fungi or bacteria, the detection of viruses is

more complicated due to their extremely small size, typically less than 100 nm. This would imply the creation of new metasurfaces with a metal gap size 10^3 orders of magnitude lower than the designs produced for the detection of bacteria, adding some difficulty to the manufacturing process. However, the technological improvements in manufacturing techniques allow us to design smaller metallic structures, that demonstrate the great potentials of virus detection with metamaterial devices [114], [131]–[133].

Regarding cancer and tumor diseases, Basal cell carcinoma (BCC) is the most common type of skin cancer as about eight out of ten cases of skin cancer are BCCs. These cancers tend to grow slowly, and although it is very rare for BCC to spread to other parts of the body, if a BCC is left untreated, it can spread to nearby areas and affect the bones as well as other tissues under the skin. Detecting cancer when it is in its early stages is often critical as it allows for the possibility of having more treatment options with better life expectancy. Current diagnosis of BCC is usually based on visual inspections, skin biopsies, or histologic techniques. Among the histological techniques, Moh's micrographic surgery has proven to be the best reported method for this application [134]. This technique allows identifying the direction of tumor spread without the need for extensive excisions and has reported cure rates of 99% for primary tumors and 96% for secondary tumors after 5 years of treatment. This is a type of controlled microscopic surgery, in which the patient remains in the operating room while the study of the extracted tissue is carried out. This technique allows the removal of the exact cancerous tissue, saving the healthy tissue. The main disadvantage is that Moh's micrographic surgery is very expensive and time-consuming.

Over the years, other imaging techniques have been proposed. The use of high-frequency ultrasound allows an axial and lateral resolution of 80 and 200 μm , respectively, and has a penetration depth of 7 mm [135]. However, it does not have chemical specificity, so it is not able to differentiate between healthy and diseased cells. Magnetic resonance is only effective if the tumor extends more than 15 mm below the surface [136]. Among the disadvantages of this technique is the need of the whole subject for inspection, as well as the fact that it is an expensive and time-consuming technique. Several NIR imaging techniques such as confocal microscopy have also been studied, able to provide a high resolution in real time with values of axial and lateral resolution of 4 and 2 μm [137]. The disadvantage is that this technique provides a very low penetration depth of just a few hundreds of micrometers.

The first report of THz spectroscopy applied for ex vivo cancer detection was published several years ago using THz pulsed imaging (TPI) technique with the purpose of differentiating between BCC and normal tissue [138]. For that, both a BCC and a healthy sample of the same patient were analyzed and images were taken in both visible and THz range. As mentioned in the work, THz images gave a lot more information. These results are explained due to the fact that BCC absorbs more water and therefore shows an increased THz absorption in comparison with normal tissue. The results of this study show that the level of contrast obtained by means of TPI is higher than that obtained by histology techniques. After this work, other studies were published for ex vivo skin cancer detection by the use of TPI. However, it was in [139] where a systematic in vivo study of the response of THz radiation to normal skin was conducted in order to evaluate the interaction of THz radiation with normal skin on the hand palm.

Expanding the reach of metasurface sensors, structures based on metasurfaces in detection and distinction between healthy and cancer cells have also been developed in recent years for many applications, such as the detection of apoptosis in oral cancer cells [140], monitoring of living cervical cancer cells [113], or detection of malignant glioma cells [112], among others.

2.4. Our work (A, B): From Meta-atoms to Metageometries

Metasurfaces operating in the THz band have been shown to have great potential for very thin-film and biochemical sensing applications, as seen in the examples above. Although all the previous examples reported here work well as sensing platforms, they present some limitations in their sensitivity and FOM.

Although it has been seen that fabrication techniques such as ATL can enhance the electric field concentration by a high percentage, this procedure is time-consuming, and difficult to implement for complex patterned designs. Thus, in this section of the thesis we address a solution that allows the implementation of much more sensitive sensors, without resorting to complex fabrication techniques.

The main disadvantage of meta-atom-based devices is that the metasurface resonances are very localized at discrete points of the surface (see Fig. 2.4, panel (a)). This makes it difficult to detect any analyte when deposited in areas with not enough interaction with the surface electric field. A stronger interaction with the dielectric analyte and hence better performance can be possible by enhancing the electric field confinement in the surrounding of the metallic parts of the structure. To tackle this challenge, more complicated geometries can be designed to distribute the electric field more evenly over the entire surface.

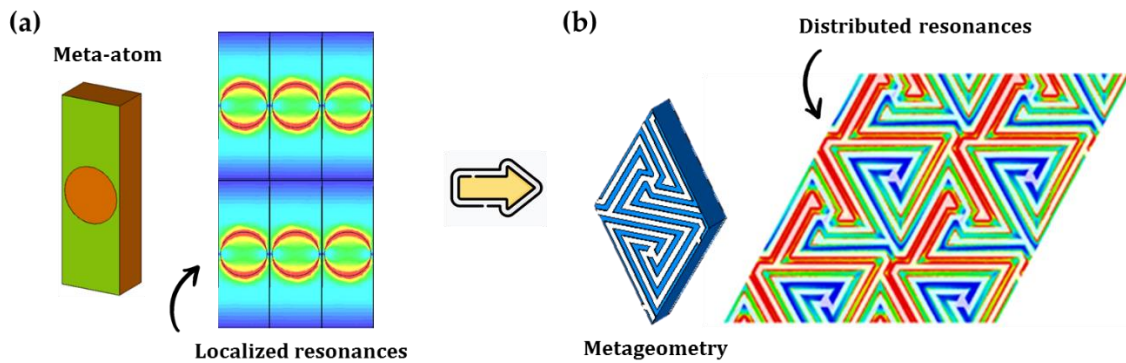


Figure 2.4: (a) Electric field distribution of a meta-atom-based structure, with localized resonances. (b) Electric field distribution in a metageometry, with distributed resonances.

[PAPER A]: Labyrinth metasurface for thin-film sensing

In our work [PAPER A], we propose a paradigm shift from classical meta-atoms to more elaborated metageometries resulting in an ultrasensitive performance. Our design is known as *Labyrinth* metasurface (see Fig. 2.5) due to its intricate labyrinth pattern that produces a high electric field confinement on the whole surface of the structure, and not only at discrete. The major improvement of having this electric field distribution over classical meta-atom devices is that the place where the analyte is deposited becomes no longer so critical. Thus, wherever the analyte falls, there will be enough interaction with the metasurface resulting in an improved sensitivity and FOM, as well as in the ability to detect much smaller analyte concentrations, or thicknesses.

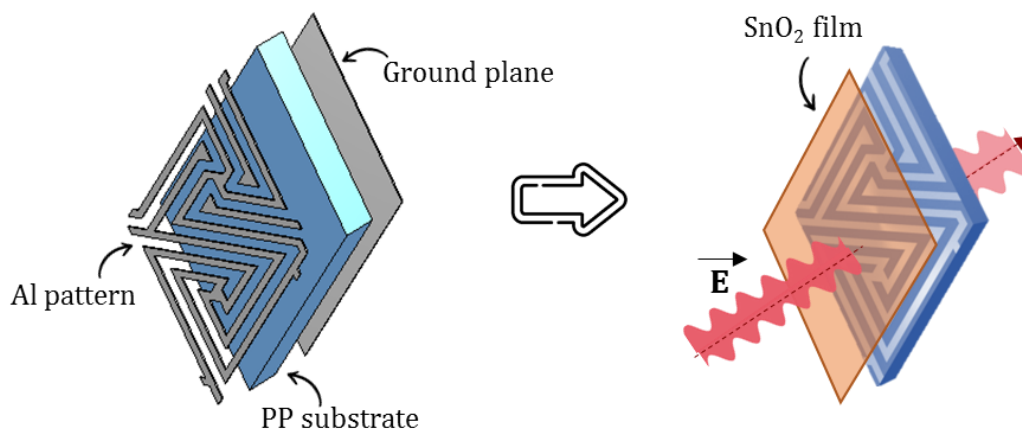


Figure 2.5: Schematic of the layers composing the designed labyrinth structure (left). Schematic of the designed structure when coating its surface with a thin-film layer.

The work done in [PAPER A] can be divided in the following steps:

- We made an extensive numerical study of the metasurface behavior as an absorber. First, we studied the simulated spectral transmittance of the labyrinth metasurface without ground plane at different angles of incidence, showing excellent angular stability.
- We added a ground plane to the labyrinth metasurface and consider the reflection coefficient in the following steps. We analyzed the metasurface absorber without any analyte on top assuming normal incidence and both vertical and horizontal polarizations, and proved again that the response is independent of the polarization angle (for the next steps, vertical polarization was chosen).
- The sensing capability of the labyrinth metasurface as a thin-film sensor was numerically and experimentally evaluated. For that, we coated its surface with thin tin dioxide (SnO_2) films, with dielectric permittivity, $\epsilon = 4$, and thicknesses ranging from 24 nm ($1.1 \times 10^{-5} \lambda_0$) to 345 nm ($15.6 \times 10^{-5} \lambda_0$).
- With the achieved results, the labyrinth metasurface is able to discriminate differences in SnO_2 thickness of less than 25 nm even for a relatively low dielectric constant.

Author contribution to this work:

- Numerical simulations obtained with the commercial simulator CST Studio Suite.
- Experimental characterization with an ABmm Vector Network Analyser (VNA) MVNA-8-350-4 equipped with a quasioptical bench working in the reflection configuration.
- Results validation and graphical representation.
- Manuscript preparation and writing

Artículo eliminado por restricciones de derechos de autor

Jáuregui-López, I., Rodríguez-Ulibarri, P., Urrutia, A., Kuznetsov, S.A. and Beruete, M. (2018), Labyrinth Metasurface Absorber for Ultra-High-Sensitivity Terahertz Thin Film Sensing. *Phys. Status Solidi RRL*, 12: 1800375. <https://doi.org/10.1002/pssr.201800375>

[PAPER B]: Labyrinth metasurface for fungi detection

Motivated by the great results obtained with the previous work, in [PAPER B] we extended the scope of metageometries towards biosensing applications, performing a thorough numerical analysis of the labyrinth metasurface as a fungi detector. The reason for choosing fungi as an analyte is that it is one of the preferred analytes in the biological sensing literature, due to its size, which is comparable to the gaps of metasurfaces operating at these frequencies (see Fig. 2.6), as well as its ease of modeling and experimental handling. Due to the small size of fungi elements ($1\text{-}2\ \mu\text{m}$), we had to downscale the labyrinth design reported in [PAPER A] by approximately 6.7 times to put the absorption resonance within the frequency range of $0.6\text{-}1\ \text{THz}$, and have metasurface gaps of a size similar to that of the fungi elements, thus enhancing its detection (see Fig. 2.6), as follows:

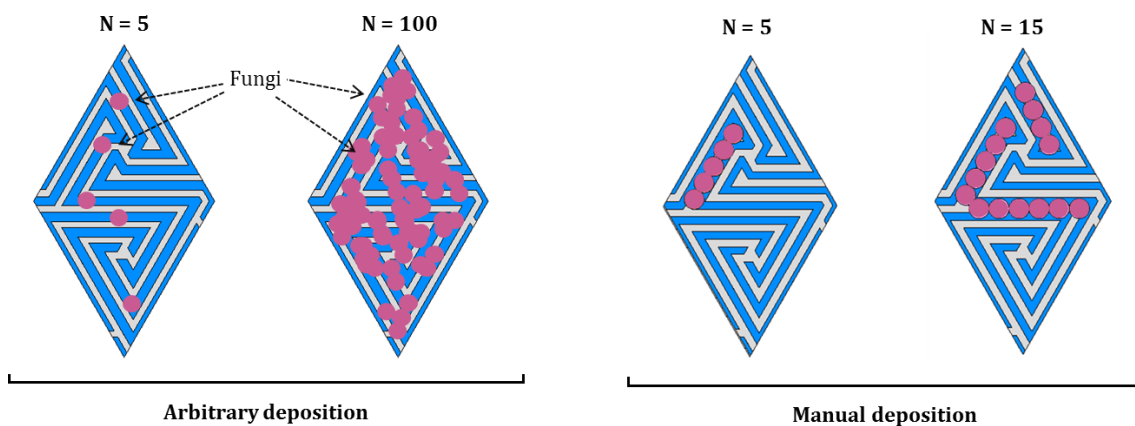


Figure 2.6: From view of the designed labyrinth when coating its surface with fungi elements arbitrarily distributed (left), and when placing the elements manually (right).

- As a first step, we made a statistical numerical study in order to guarantee that the results have adequate repeatability. Several simulations were done for different number of fungi elements distributed arbitrarily in the surface of the labyrinth metasensor, ranging from $N = 5$, to $N = 100$.
- Once the repeatability of the results and the correct detection thresholds were ensured, the sensing capability was evaluated by obtaining the sensitivity and FOM values, showing that the labyrinth metasensor is able to detect just a few number of fungi elements with good results in comparison with other works available in the literature.
- For the above results, the elements were arbitrarily deposited on the surface. However, in order to know the maximum performance of this structure, a discrete number of fungi elements of $N = 5$ and $N = 15$ were manually deposited in the micro-gap of the metasurface, where the electric field concentration is maximum, showing that the frequency shift of the resonance was much larger in this case, and demonstrating the high importance of the analyte location over the surface.

The great performance of the labyrinth metasurface achieved in both previous works demonstrates that the use of convoluted metageometries instead of meta-atoms improves



the electric field concentration within the surface and not only at discrete points. These new type of structures where the enhanced electric field is distributed over a much larger surface area of the device, allow us to detect analytes up to 5 times thinner than the operating wavelength. Moreover, metageometries can be of high interest for biological sensing when the amount of sample under measurement is relatively small. However, the technological aspects of the device fabrication are more complex at higher frequencies, especially with such intricate designs.

Author contribution to this work:

- Design of the structure at the operational frequency of at 0.856 THz.
- Randomizing function creation for the fungi arbitrary deposition with Matlab software.
- Numerical simulations obtained with the commercial simulator CST Studio Suite.
- Results validation and graphical representation.
- Manuscript preparation and writing.

Article

Labyrinth Metasurface for Biosensing Applications: Numerical Study on the New Paradigm of Metageometries

Irati Jáuregui-López ^{1,2}, Pablo Rodríguez-Ulibarri ¹ , Sergei A. Kuznetsov ^{3,4}, Carlos Quemada ¹ and Miguel Beruete ^{1,2,5,*} 

¹ Antennas Group-TERALAB, Universidad Pública de Navarra, Campus Arrosadía, 31006 Pamplona, Spain; irati.jauregui@unavarra.es (I.J.-L.); pabloru86@gmail.com (P.R.-U.); carlos.quemada@unavarra.es (C.Q.)

² Multispectral Biosensing Group, Navarrabiomed, Complejo Hospitalario de Navarra (CHN), Universidad Pública de Navarra (UPNA), IdiSNA. Irunlarrea 3, 31008 Pamplona, Navarra, Spain

³ Rzhanov Institute of Semiconductor Physics SB RAS, Novosibirsk Branch “TDIAM”, Lavrentiev Ave. 2/1, 630090 Novosibirsk, Russia; SAKuznetsov@nsm.nsu.ru

⁴ Novosibirsk State University, Pirogova St. 2, 630090 Novosibirsk, Russia

⁵ Institute of Smart Cities (ISC), Public University of Navarra, 31006 Pamplona, Spain

* Correspondence: miguel.beruete@unavarra.es; Tel.: +34-948-169-727

Received: 13 September 2019; Accepted: 9 October 2019; Published: 11 October 2019



Abstract: The use of metasurfaces operating in the terahertz regime as biosensor devices has attracted increased interest in recent years due to their enhanced sensitivity and more accurate detection capability. Typical designs are based on the replica of relatively simple unit cells, usually called metaatoms. In a previous paper, we proposed a new paradigm for ultrasensitive thin-film sensors based on complex unit cells, called generically metageometries or labyrinth metasurfaces. Here, we extend this concept towards biosensing, evaluating the performance of the labyrinth as a fungi detector. The sensing capabilities are numerically evaluated and a comparison with previous works in this field is performed, showing that metageometries improve the performance compared to metaatoms both in sensitivity and figure of merit, by a factor of more than four. In particular, we find that it is able to detect five fungi elements scattered on the unit cell, equivalent to a concentration of only $0.004/\mu\text{m}^2$.

Keywords: metasurface; terahertz; biosensor

1. Introduction

Due to its importance in human health as well as basic research, biological sensing, or biosensing, is gaining an increased interest amongst the scientific community. Biological sensing refers to the measurement of biological or chemical parameters and is based on the specific interaction between the entity under test (usually called analyte) and the sensing platform itself [1]. Most biomolecules have characteristic vibrational modes in the terahertz (THz) range (0.1–10 THz), which makes this band an excellent candidate for the development of new biosensing devices, or as an aid to complement and enrich the performance of existing ones [2]. Contrary to other traditional techniques, such as X-rays, THz radiation is non-ionizing and therefore harmless to living organisms. Some other advantages of THz waves are their sensitivity to water, making it suitable for tumor or cancer detection and diagnosis, since tumor cells contain a different water percentage than healthy cells [3]. For these reasons, THz waves have been investigated in a wide variety of biosensing applications, such as diseases diagnosis [4], DNA sequencing [5], detection of antibiotics [6] and protein concentrations [7], and detection of bacteria [8] and viruses [9], among others.

Metamaterials can be defined as artificial materials engineered to present desired electromagnetic properties by controlling their shape and geometry. They are usually composed of an array of resonators much smaller than the operational wavelength. As a consequence of their reduced electrical size, they produce high electric field confinement at localized spots giving rise to strong changes in the spectral response, a property that can be exploited in sensing applications [1]. In the last years, they have been proposed to implement high quality biosensing devices. Metasurfaces—the planar version of metamaterials—have also emerged as an excellent alternative in the design of label-free sensing devices in biological applications [10]. They are very sensitive to changes in the refractive index near the structure, making possible a relatively cheap and easy way to detect samples deposited on the surface, with a great potential in sensitive label-free detection. In this way, metasurface sensors overcome the limitations of classical techniques [11], such as time-domain spectroscopy, where the major problem is the difference in sizes between the wavelength of the THz wave ($\sim 10\text{--}1000\ \mu\text{m}$), and the thickness of the sample to be analyzed ($<1\ \mu\text{m}$), sometimes causing the sample to be invisible to the radiation. With the use of metasurfaces this problem is solved since sensing is based on the response of the structure itself, instead of measuring the sample response. As discussed in [12] there are other popular strategies for THz sensors, such as waveguides (both dielectric and metallic) and plasmonic structures. A crucial advantage of metasurface sensors is the flexibility they have to adapt to experimental setups, with direct wave illumination. This simplicity along with their enhanced sensitivity have put them in the vanguard of THz sensing applications. To date, metasurfaces operating in the THz regime have also shown promising results in microorganism biosensing, with designs capable of detecting very low concentrations of bacteria [8], yeast [13], and viruses [9,14].

Since their first conception, many different designs have been proposed, from the simplest designs [15,16], to more complex ones including graphene [17], or combination of slot antenna arrays with silver nanowires [14]. Whichever the structure employed, the main challenge in biosensing applications is how to achieve a high quality sensor when the analyte has an extremely small size compared to the wavelength, and hence it does not interact sufficiently with the radiating waves. The main goal of metasurface sensors is to provide high electric field confinement within the structure and enhance the detection of small analytes [10]. In order to address this challenge, a new paradigm shift from metaatoms (metasurfaces with discrete resonators) to more elaborated metageometries has been recently proposed [18]. Metageometries are designed to have the electric field highly confined all along the surface and not only at discrete points, which is a clear advantage for sensing applications compared to the “metaatom” approach. A further discussion comparing the performance of different metasurface sensor geometries at THz can be found in a recent review [10].

In a previous work [18], we demonstrated the excellent performance of metageometries in thin-film sensing applications by means of a labyrinth metasurface absorber working at THz. This structure is able to detect thin-films with a thickness of 10^{-5} times less than the operation wavelength, improving largely the results of metaatom-based sensors realized with the same manufacturing techniques. In this paper, we extend the scope of metageometries towards biosensing applications, performing a thorough numerical analysis of the labyrinth metasurface as a fungi sensor and compare its performance with previous works [8]. Our results demonstrate that the labyrinth metasurface is also promising in biosensing applications.

2. Materials and Methods

The metasurface sensor investigated in this work was designed to operate in absorption and was configured as a tri-layer structure with a metallic labyrinth pattern deposited on a flexible polypropylene (PP) slab $29\ \mu\text{m}$ thick with back metallization (ground plane or GP), as shown in Figure 1. The geometry of the labyrinth pattern, which utilizes convoluted-shape apertures arranged on a triangular lattice, was taken from [18] and then downscaled by approximately 6.7 times to put the absorption resonance within the frequency range of 0.6–1 THz. The relevant metasurface dimensions are periodicity, $d = 36.4\ \mu\text{m}$; distance between metallic strips, $s = 1.5\ \mu\text{m}$; strip width $w = 1.5\ \mu\text{m}$;

metallization thickness $t = 0.4 \mu\text{m}$. In a practical implementation, the small-scale thin-film structure of this kind should be supported by a massive wafer (e.g., fabricated on top of a carrying silicon substrate). Evidently, thanks to the GP layer that blocks the transmission, the presence of the wafer would not affect the sensor's performance.

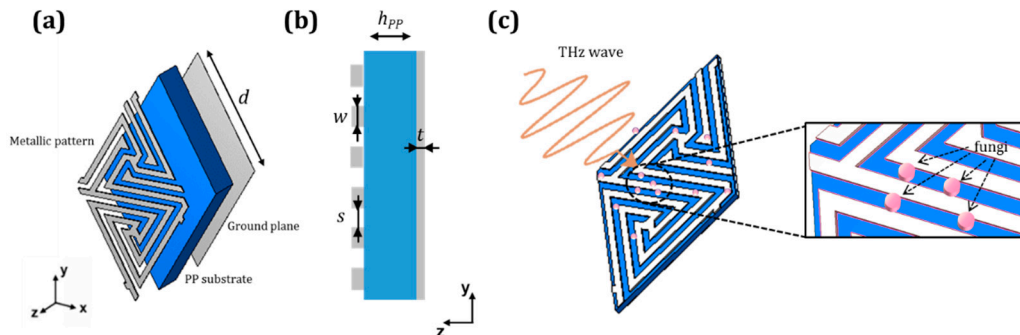


Figure 1. Front (a) and cross-sectional (b) views of the designed labyrinth metasurface unit cell. Metallization is shown in gray and polypropylene (PP) substrate in blue. Relevant dimensions: $h_{PP} = 29 \mu\text{m}$, $d = 36.4 \mu\text{m}$, $t = 0.4 \mu\text{m}$, $s = 1.5 \mu\text{m}$; $w = 1.5 \mu\text{m}$. (c) Schematic of the labyrinth metasurface working as a fungi metasensor. Fungi are modeled as cylinders of radius $r_f = 2 \mu\text{m}$, height $h_f = 1 \mu\text{m}$, and dielectric permittivity $\epsilon_f = 8$ and are randomly distributed on the unit cell surface.

The designed labyrinth metasurface was simulated in the band of 0.6–1 THz using the commercial simulator CST Microwave Studio®. To model the labyrinth metasurface as an infinite array, the regime of Floquet ports and periodic boundary conditions applied to the designed unit cell was employed. PP was modeled as a low-loss dielectric with a relative permittivity $\epsilon_{PP} = 2.25 \cdot (1 - j \cdot 10^{-3})$ extrapolated from our previous study [18,19]. The metallic layers of the labyrinth pattern and GP were modeled as a lossy metal with electrical conductivity $\sigma = 1.5 \times 10^7 \text{ S/m}$ which mimics aluminum (Al) deposited on PP; as found in [20], this value is reduced compared to the nominal conductivity of bulk Al due to inherent surface roughness and granularities of PP films [19]. The excitation of the metasurface was done at normal incidence and vertical polarization, as shown in Figure 1c. It is worth noting that the labyrinth geometry is polarization insensitive under normal illumination [18]. The response of the analyte-free structure exhibits a narrow dip in the reflection coefficient at 0.856 THz (see the black curve in Figure 2c).

The performance of the labyrinth metasurface as a biosensor was evaluated numerically by placing fungi onto the patterned layer of the metasurface. The reason for using fungi as analyte is that their size, of the order of micrometers [8], is similar to the metasurface gaps, so they can be “trapped” in those gaps where high electric field confinement occurs, thereby enabling high sensitivity detection. Fungi were represented as dielectric cylinders with a radius $r_f = 2 \mu\text{m}$, height $h_f = 1 \mu\text{m}$ and dielectric permittivity of $\epsilon_f = 8$, following the model obtained for yeast reported in [8]. Fungi elements were arbitrarily scattered within the unit cell using a randomizing function for the fungi position in both x and y axes, ensuring that all the cylinders fall within the cell limits. We considered possible fungi overlapping since this may occur in a real deposition scenario. Note that, due to computational restraints, in our approximation we are assuming the same fungi distribution for all unit cells of the structure, which is not completely realistic in practical sensing applications. An analysis of the whole structure would be preferable but extremely demanding in computation resources. The approximation done here gives a good hint about the performance of the labyrinth metasurface and allows for a sufficiently accurate analysis of its potential as biosensor. The deposition thresholds (i.e., number of cylinders deposited in each case) were chosen after a thorough study, selecting the cases to avoid overlap between the response of different concentrations of fungi.

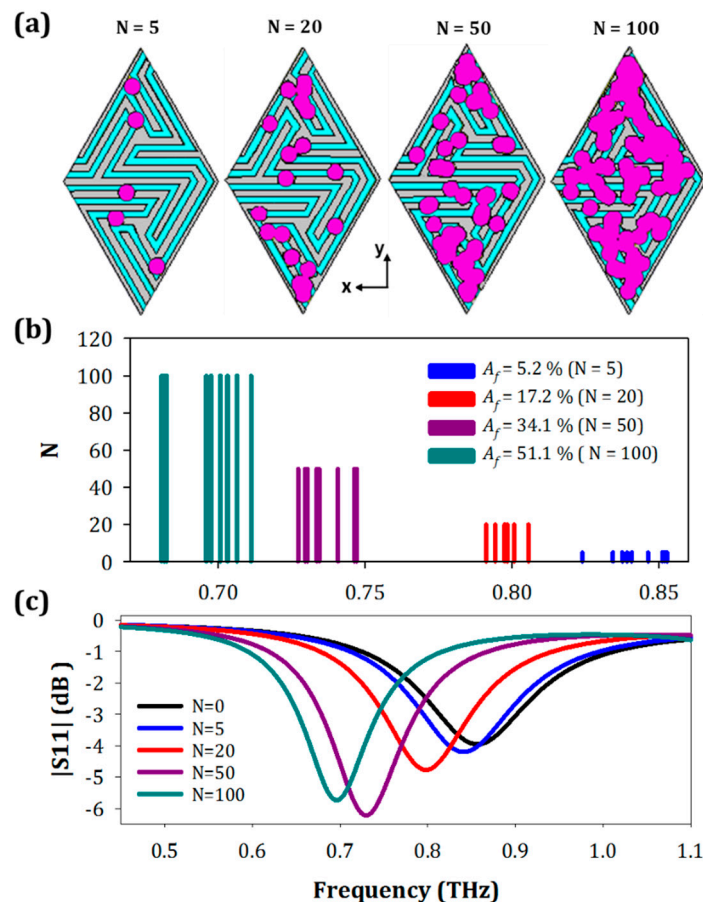


Figure 2. (a) Front view of the structure with $N = 5; 20; 50; 100$ fungi (purple cylinders). (b) Resonance frequency for all the simulations carried out for different fungi concentrations: $N = 5$ (blue curve), $N = 20$ (red curve), $N = 50$ (purple curve), and $N = 100$ (dark cyan curve). (c) Reflection coefficient for different fungi concentrations, cases nearest to the mean values.

3. Results and Discussion

As a first step, we performed a statistical numerical study in order to guarantee that the results have adequate repeatability. The number of fungi was varied from $N = 5$ to $N = 100$ elements and 10 different simulations were done in each case. A schematic of the fungi location over the surface is shown in Figure 2. For the sake of clarity, only the four most significant results are presented in Figure 2, $N = 5, 20, 50$, and 100 . Note that our main objective is to find the minimal amount of sample detectable by the proposed metasensor.

As can be observed in Figure 2b, for an identical number of fungi the resonance frequency experiences slight variations depending on the fungi position within the unit cell. This is explained by a non-uniform electric field distribution over the metasurface unit cell. Despite these variations, the detection thresholds were chosen to avoid overlap between consecutive cases allowing for an unambiguous detection. To get a better description of the metasurface performance, the results of Figure 2b were represented in terms of a fractional area defined as $A_f = A_0/A_T$, where A_0 represents the area occupied by the microorganisms (extracted directly from the simulator), and A_T the total area of the metasensor surface (calculated analytically). Since A_0 has some variations, depending on the fungi overlap, we took an average of all cases, obtaining mean fractional areas of 5.23% ($N = 5$), 17.2% ($N = 20$), 34.1% ($N = 50$), and 51.13% ($N = 100$).

The spectral performance of the labyrinth metasensor can be grasped from the selected representative curves of Figure 2c. To select these curves, we calculated in the first place the mean value of the resonance frequency for each N . Afterwards, we looked for the simulation case

whose resonance frequency was closer to the calculated mean resonance frequency value. These are the curves represented in the figure. From the simulation results of Figure 2b,c, we find that the maximum resonance frequency shift happens for $N = 100$, with a variation of nearly 19% (from 856 to 696 GHz) and a standard deviation of 10.3 GHz. The minimum is obtained for $N = 5$, with a resonance frequency shift of 1.6% and a standard deviation of 8.5 GHz. These results suggest that the metasensor designed is able to discriminate small concentrations of microorganisms deposited on top.

In order to characterize quantitatively the performance of the structure, we calculated its sensitivity (S) and figure of merit (FOM). Although there are many different definitions for the sensitivity in the literature, see [10,21], almost all of them link the resonance frequency shift with some other parameter that indicates the quantity of sample deposited on the metasensor. Thus, in this work we defined the sensitivity as $S = \Delta f / A_f \cdot n$ where $\Delta f = f_N - f_0$, with f_N the resonance frequency for each fungi concentration, N , and f_0 the resonance frequency without the analyte; A_f the fractional area occupied by the fungi; and n the refractive index of the fungi. The FOM is a more refined parameter defined as the ratio between the sensitivity and the full width at half minimum (FWHM) in frequency dimensions: $FOM = S / FWHM$, which takes into account the spectral linewidth of different curves, making structures with a small FWHM more appropriate for biosensing applications, as in that case, the discrepancy between different curves becomes easier to detect. Thus, a narrower spectral line will lead to higher FOM values. With these definitions, we obtained a mean sensitivity of 80 GHz/RIU, and a mean FOM of 0.85 (RIU)^{-1} , where RIU stands for refractive index units (RIU). All the values of fractional area, resonance frequency, sensitivity, and FOM for each fungi concentration are summarized in Table 1, at the end of this section. The remaining results and specific values for every simulated case are presented in the Supplementary Material.

Table 1. Comparison of the most relevant performance parameters of the labyrinth metasurface structure, for different numbers of fungi deposited on top. The cases highlighted with (*) correspond to fungi placed in the regions of maximum field intensity.

N	Fractional Area (%)	Δf (GHz)	Δf (%)	Standard Deviation	Sensitivity (GHz/RIU)	FOM (RIU) ⁻¹
0	0	856	-	-	-	-
5	5.23	842	1.64	8.5	67.3	0.73
20	17.21	797	6.85	5	85.2	0.89
50	34.08	736	13.94	7.5	87.6	0.92
100	51.13	696	18.68	10.3	78.2	0.87
5 *	5.48	778	9.02	-	351.9	2
15 *	16.45	722	15.64	-	203.4	1.36

To evaluate more deeply the labyrinth metasensor, we compared its performance with other sensors found in the literature. We chose for this comparison the work presented in [8], which is one of the most significant in terms of microorganism detection using metasurfaces, due to the high sensitivity values achieved. Therein, a metaatom-based metasurface made of a square ring with a gap at the center unit cell was used to detect different types of fungi. Microorganisms were deposited arbitrarily at a minimal density of $0.09/\mu\text{m}^2$ (calculated as the ratio between the average number of microorganisms in the capacitive gap of the metasurface, and the gap area) and showed a displacement of the resonant frequency of 9 GHz (corresponding to 1% of the resonant frequency of the bare structure). In our case, we arbitrarily deposited fungi elements at a minimal density of $0.004/\mu\text{m}^2$ (corresponding to $N = 5$ fungi and calculated as the ratio between the fungi elements and the total surface area), and we obtained a frequency shift of 14 GHz (1.6% of the resonant frequency). This means a large improvement of the previous work, as we get a larger shift with a much lower density.

To find the maximum performance of the designed structure in [8], $N = 5$ fungi elements were deposited in the micro-gap of the metasurface, where the electric field concentration is maximum. In that case, Park et al. [8] achieved a frequency shift of 2% (~15 GHz). Applying a similar procedure to the labyrinth metasurface, we find that with the deposition of $N = 5$ fungi elements in the area

of maximum electric field magnitude (see Figure 3a), a frequency shift of 9% (77 GHz) is obtained, improving the previous results by a factor of more than 4.

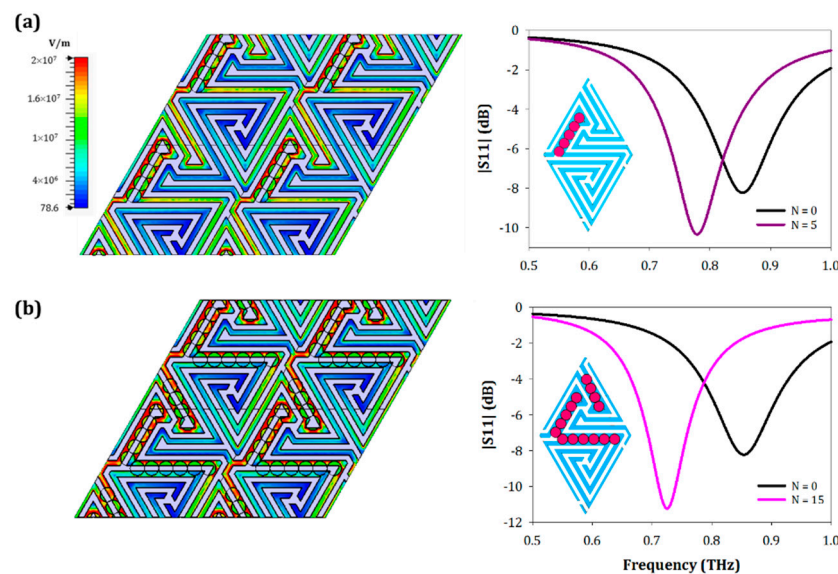


Figure 3. (a) Electric field distribution over the labyrinth surface for the designed structure with $N = 5$ ($A_f = 5.48\%$) fungi placed at the regions of maximum electric field confinement (left) and reflection coefficient comparison with the bare structure (right). (b) Electric field distribution (left) and reflection coefficient (right) when placing $N = 15$ ($A_f = 16.45\%$) fungi elements in the places where the electric field confinement is maximum (pink curve), and comparison with the bare structure (black curve).

This excellent performance is due to the intricate geometry of the metasensor, which provokes a strong electric field confinement between the adjacent metallic strips of the surface, scattered within the unit cell area and not concentrated at discrete spots. In fact, as it can be seen in Figure 3, there are more regions with high electric field confinement. If we cover systematically all these zones with $N = 15$ fungi elements, as shown in Figure 3b, the frequency shift of the resonance is much larger. Thus, with only 15 fungi elements, which represent a fractional area of 16.45%, we obtain a frequency shift of 134 GHz similar to the case of $N = 100$ fungi elements analyzed above, demonstrating the importance of the element's location. We obtained sensitivity and FOM values that are well above those obtained with a much larger number of randomly deposited fungi elements. Concretely, we reached a maximum sensitivity of 351.9 GHz/RIU, and a maximum FOM of 2 (RIU)^{-1} for the case of coating the surface with $N = 5$ fungi placed in the microgap of the surface. If we look at the comparison described in Table 1, we can verify that the values for this case almost triple those obtained in the rest of the study. It is also noticed that the sensitivity and FOM values are greater for the case of $N = 5$ fungi instead of $N = 15$ fungi ordered in the area of interest. Although the frequency shift is larger in the second case, the fractional area occupied is also higher, causing a decrease in the sensitivity.

4. Conclusions

To conclude, we reported here a labyrinth metasurface operating at THz with high sensitivity and FOM working as a fungi biosensor. The use of convoluted metageometries instead of metaatoms improves the electric field concentration within the surface and not only at discrete points. The behavior of the structure was numerically tested obtaining a mean sensitivity of 80 GHz/RIU, and a mean FOM of 0.85 (RIU)^{-1} when depositing different fungi concentrations, from $N = 5$ to $N = 100$ arbitrarily at random positions. Furthermore, a study of the electric field distribution over the metasensor surface was done. By identifying the regions of high electric field concentration, it was determined that with a number of fungi elements as low as $N = 5$, a high frequency shift of 9% (77 GHz) is obtained, improving previous works based on metaatoms by a factor of more than 4. Moreover, depositing $N = 15$ fungi

along all the area where the electric field distribution is maximum, a frequency shift of 134 GHz is achieved, similar to the case of having $N = 100$ fungi elements at random positions. This highlights the importance of the fungi location in the device and the better performance of metageometry-based designs in comparison with classical structures utilizing metaatoms. These new structures, where the enhanced electric field is distributed over a much larger surface area of the device, can be of high interest for biological sensing when the amount of sample under measurement is relatively small.

The study presented in this work is limited to numerical investigations. Fabricating the proposed metasurface biosensor and its experimental testing is under consideration now. The technological aspects of the sensor's fabrication, as well as the issues of sensor's viability and contamination of the substrate, are beyond the scope of this paper and will be published elsewhere.

Supplementary Materials: The following are available online at <http://www.mdpi.com/1424-8220/19/20/4396/s1>, Table S1: Frequency resonance for all the simulations carried out for each fungi concentration, average and typical deviation for each case.

Author Contributions: Conceptualization, M.B.; methodology, I.J.-L., P.R.-U., and M.B.; software, I.J.-L. and M.B.; validation, I.J.-L., P.R.-U., S.A.K., and M.B.; formal analysis, I.J.-L.; investigation, I.J.-L., P.R.-U., C.Q., and M.B.; resources, M.B.; writing—original draft preparation, I.J.-L., and M.B.; writing—review and editing, I.J.-L., P.R.-U., S.A.K., C.Q., and M.B.; visualization, I.J.-L., P.R.-U. and M.B.; supervision, P.R.-U. and M.B.; project administration, M.B.; funding acquisition, M.B. and S.A.K.

Funding: This research was funded by the Spanish Ministerio de Ciencia, Innovación y Universidades, Project RTI2018-094475-B-I00 (MCIU/AEI/FEDER, UE) and partially by the Russian Science Foundation, Project 19-12-00103.

Conflicts of Interest: The authors declare no conflict of interest. The funders had no role in the design of the study; in the collection, analyses, or interpretation of data; in the writing of the manuscript, or in the decision to publish the results.

References

1. Xu, W.; Xie, L.; Ying, Y. Mechanisms and applications of terahertz metamaterial sensing: a review. *Nanoscale* **2017**, *9*, 13864–13878. [[CrossRef](#)] [[PubMed](#)]
2. Son, J.-H. *Terahertz Biomedical Science & Technology*, 1st ed.; Soo, J.-H., Ed.; CRC Press: Boca Raton, FL, USA, 2014; ISBN 9781466570450.
3. Pickwell, E.; Wallace, V.P. Biomedical applications of terahertz technology. *J. Phys. D. Appl. Phys.* **2006**, *39*, R301–R310. [[CrossRef](#)]
4. Woodward, R.M.; Wallace, V.P.; Pye, R.J.; Cole, B.E.; Arnone, D.D.; Linfield, E.H.; Pepper, M. Terahertz pulse imaging of ex vivo basal cell carcinoma. *J. Invest. Dermatol.* **2003**, *120*, 72–78. [[CrossRef](#)]
5. Yang, Y.; Xu, D.; Zhang, W. High-sensitivity and label-free identification of a transgenic genome using a terahertz meta-biosensor. *Opt. Express* **2018**, *26*, 31589. [[CrossRef](#)] [[PubMed](#)]
6. Xie, L.; Gao, W.; Shu, J.; Ying, Y.; Kono, J. Extraordinary sensitivity enhancement by metasurfaces in terahertz detection of antibiotics. *Sci. Rep.* **2015**, *5*, 8671. [[CrossRef](#)] [[PubMed](#)]
7. Bui, T.S.; Dao, T.D.; Dang, L.H.; Vu, L.D.; Ohi, A.; Nabatame, T.; Lee, Y.; Nagao, T.; Hoang, C.V. Metamaterial-enhanced vibrational absorption spectroscopy for the detection of protein molecules. *Sci. Rep.* **2016**, *6*, 32123. [[CrossRef](#)] [[PubMed](#)]
8. Park, S.J.; Hong, J.T.; Choi, S.J.; Kim, H.S.; Park, W.K.; Han, S.T.; Park, J.Y.; Lee, S.; Kim, D.S.; Ahn, Y.H. Detection of microorganisms using terahertz metamaterials. *Sci. Rep.* **2014**, *4*, 4988. [[CrossRef](#)] [[PubMed](#)]
9. Park, S.J.; Cha, S.H.; Shin, G.A.; Ahn, Y.H. Sensing viruses using terahertz nano-gap metamaterials. *Biomed. Opt. Express* **2017**, *8*, 3551. [[CrossRef](#)] [[PubMed](#)]
10. Beruete, M.; Jáuregui-López, I. Terahertz Sensing Based on Metasurfaces. *Adv. Opt. Mater.* **2019**, 1900721. [[CrossRef](#)]
11. Jáuregui-López, I.; Rodríguez-Ulibarri, P.; Kuznetsov, S.A.; Nikolaev, N.A.; Beruete, M. THz Sensing With Anomalous Extraordinary Optical Transmission Hole Arrays. *Sensors* **2018**, *18*, 3848. [[CrossRef](#)] [[PubMed](#)]
12. Rodríguez-Ulibarri, P.; Beruete, M. Sensing at Terahertz Frequencies. In *Fiber Optic Sensors (Smart Sensors, Measurement and Instrumentation vol 21)*; Matías, I.R., Ikezawa, S., Corres, J., Eds.; Springer International Publishing: Cham, Switzerland, 2017; Volume 21, pp. 301–327.

13. Park, S.J.; Son, B.H.; Choi, S.J.; Kim, H.S.; Ahn, Y.H. Sensitive detection of yeast using terahertz slot antennas. *Opt. Express* **2014**, *22*, 30467. [[CrossRef](#)] [[PubMed](#)]
14. Hong, J.T.; Jun, S.W.; Cha, S.H.; Park, J.Y.; Lee, S.; Shin, G.A.; Ahn, Y.H. Enhanced sensitivity in THz plasmonic sensors with silver nanowires. *Sci. Rep.* **2018**, *8*, 1–8. [[CrossRef](#)] [[PubMed](#)]
15. Singh, R.; Cao, W.; Al-Naib, I.A.I.; Cong, L.; Withayachumnankul, W.; Zhang, W. Ultrasensitive terahertz sensing with high-Q Fano resonances in metasurfaces. *Appl. Phys. Lett.* **2014**, *105*, 171101. [[CrossRef](#)]
16. Gupta, M.; Srivastava, Y.K.; Manjappa, M.; Singh, R. Sensing with toroidal metamaterial. *Appl. Phys. Lett.* **2017**, *110*, 121108. [[CrossRef](#)]
17. Xu, W.; Xie, L.; Zhu, J.; Tang, L.; Singh, R.; Wang, C.; Ma, Y.; Chen, H.T.; Ying, Y. Terahertz biosensing with a graphene-metamaterial heterostructure platform. *Carbon N. Y.* **2019**, *141*, 247–252. [[CrossRef](#)]
18. Jáuregui-López, I.; Rodríguez-Ulibarri, P.; Urrutia, A.; Kuznetsov, S.A.; Beruete, M. Labyrinth Metasurface Absorber for Ultra-High-Sensitivity Terahertz Thin Film Sensing. *Phys. status solidi - Rapid Res. Lett.* **2018**, *12*, 1800375. [[CrossRef](#)]
19. Navarro-Cía, M.; Kuznetsov, S.A.; Aznabet, M.; Beruete, M.; Falcone, F.; Sorolla, M. Route for Bulk Millimeter Wave and Terahertz Metamaterial Design. *IEEE J. Quantum Electron.* **2011**, *47*, 375–385. [[CrossRef](#)]
20. Kuznetsov, S.A.; Paulish, A.G.; Navarro-Cía, M.; Arzhannikov, A.V. Selective Pyroelectric Detection of Millimetre Waves Using Ultra-Thin Metasurface Absorbers. *Sci. Rep.* **2016**, *6*, 21079. [[CrossRef](#)] [[PubMed](#)]
21. Tao, H.; Strikwerda, A.C.; Liu, M.; Mondia, J.P.; Ekmekci, E.; Fan, K.; Kaplan, D.L.; Padilla, W.J.; Zhang, X.; Averitt, R.D.; et al. Performance enhancement of terahertz metamaterials on ultrathin substrates for sensing applications. *Appl. Phys. Lett.* **2010**, *97*, 261909. [[CrossRef](#)]



© 2019 by the authors. Licensee MDPI, Basel, Switzerland. This article is an open access article distributed under the terms and conditions of the Creative Commons Attribution (CC BY) license (<http://creativecommons.org/licenses/by/4.0/>).

Chapter III: Metasurfaces for Food Safety

In this part of the thesis we change our sensing target to chemical substances, specifically Polycyclic Aromatic Hydrocarbons, that have shown to have a detrimental effect on human health. This chapter provides an introduction to these substances, and puts into context the interest in their effective detection. As final part, we present our own contribution to the topic.

3.1. Polycyclic Aromatic Hydrocarbons (PAHs) – What are they?

Polycyclic Aromatic Hydrocarbons (PAHs) encompass hundreds of organic compounds containing two or more fused aromatic rings, composed of carbon and hydrogen atoms. Depending on the number of aromatic rings in a compound, they can be classified into light or heavy. Thus, compounds with 2-3 rings, extremely volatiles, comprise light PAHs; whereas less volatile compounds with more than 4 rings are classified as larger or heavy PAHs [141], [142]. These PAHs are non-biodegradable, persist in the environment, and are classified as harmful to human health. The pyrolytic process of formation of these compounds depends fundamentally on three factors (high temperatures, low O₂ levels, and the presence of organic matter), resulting in incomplete combustion [143]. This process generates a mixture of PAHs that tend to accumulate in the environment, affecting the air or water among others, and entering the food chain.

Of the total human exposure to these compounds, more than 80% is through food consumption, especially in non-smokers [142]. This food contamination may be due to two main factors: environmental contamination, and food processing [141]. Environmental contamination leads to a concentration of PAHs in the atmosphere (water, air), which ends up in vegetation. In turn, this vegetation acts as feed for livestock or aquatic species and therefore leads to contamination of meat and marine products and their derivatives. On the other hand, PAHs can also be generated during food processing, especially in processes involving fuel partial combustion [141], [143], high temperature preparations [144], [145], and cooking involving direct exposure to flames [145], [146].

At the turn of the century, the Scientific Committee on Food, on the basis of their occurrence and toxic effects, selected 33 individual PAHs from the several hundred environmentally persistent compounds that presented risks to human health [147]. In recent years, the International Agency for Research on Cancer (IARC), the Agency for Toxic Substances and Disease Register (ATS-DR), the US Environmental Protection Agency (EPA), the Scientific Committee on Food (SCF), the Joint Food and Agriculture Organization (FAO)/World Health Organization (WHO) Expert Committee on Food Additives (JECFA), and the European Union (EU) have classified PAHs regarding their carcinogenic and mutagenic properties of PAHs present in food (see Table 3.1). Among all of them, The European Commission (EC) has identified four major PAHs (PAH4) in foods: benz[a]anthracene (BaA), chrysene (Chr), benzo[b]fluoranthene (BbF), and benzo[a]pyrene (BaP) [148]. Within this group, the IARC classifies BaP as carcinogenic to humans (group 1), whereas BaA, BbF, and Chr, are classified as possibly carcinogenic to humans (group 2B).

3.1.1. Health risks and regulation

PAHs have a lipophilic nature, which means that they have an increased solubility in fats. This lipophilic nature allows them to be easily attached to the cell membrane, producing structural changes in the cells that can affect their normal behavior [149]. This is why foods with a high fat content are excellent delivery systems for these molecules, and allow their absorption by the intestinal tract [150], [151]. Recently, Emel Oz [151] evaluated the formation of BaP and PAH4 in several barbecued meatballs formulated with different animal fats (beef intermuscular and/or sheep tail). The study showed that the use of different animal fat significantly affected the amount of BaP and PAH4, with quantification values that ranged between 2.33–4.30 and 8.41–15.48 ng/g, respectively. It was also shown

that using a mixture of intermuscular and sheep tail fat reduced the PAH formation in about 46% compared with the meatballs made only with sheep tail fat, which have a higher proportion of polyunsaturated fatty acids.

Table 3.1. Chemical, carcinogenic, and mutagenic properties of PAHs.

Compound name	Abbreviation	Chemical Formula	Genotoxicity	IARC classification ^a
Acenaphthene	ACE	C ₁₂ H ₁₀	Questionable	Not evaluated
Acenaphthylene	ACY	C ₁₂ H ₁₀	Questionable	Not evaluated
Anthracene	ANT	C ₁₄ H ₁₀	Negative	3
Benz(a)anthracene	BaA	C ₁₈ H ₁₂	Positive	2B
Benzo(b)fluoranthene	BbF	C ₂₀ H ₁₂	Positive	2B
Benzo(k)fluoranthene	BkF	C ₂₀ H ₁₂	Positive	2B
Benzo(g,h,i)perylene	BPe	C ₂₂ H ₁₂	Positive	3
Benzo(a)pyrene	BaP	C ₂₀ H ₁₂	Positive	1
Chrysene	Chr	C ₁₈ H ₁₂	Positive	2B
Dibenz(a,h)anthracene	DBA	C ₂₂ H ₁₄	Positive	2A
Fluoranthene	FLT	C ₁₆ H ₁₀	Positive	3
Flourene	FLR	C ₁₃ H ₁₀	Negative	3
Indeno(1,2,3-cd)pyrene	IcP	C ₂₂ H ₁₂	Positive	2B
Phenanthrene	PHN	C ₁₄ H ₁₀	Questionable	3
Pyrene	PYR	C ₁₆ H ₁₀	Questionable	3
Naphthalene	NAP	C ₁₀ H ₈	Positive	2B

^a 1 – Carcinogenic, 2A – Probably carcinogenic, 2B – Possibly carcinogenic and 3 – Not classifiable
Adapted from [142].

Chronic human exposure to PAHs favors the growth or the prevalence of some diseases such as lung cancer (in smokers), or intestinal diseases (in non-smokers). The toxic effects of PAHs depend largely on the duration and mode of exposure [152]. Although the ability of PAHs to induce short-term effects is unclear, exposure to high levels may result in eye irritation, nausea, diarrhea, or confusion. Specifically, Naphthalene (NAP) and BaP are direct skin irritants, and may cause allergic reactions in animals and humans [152], [153]. Long-term adverse effects (chronic exposure) include decreased immune system, liver and kidney damage, respiratory problems, asthma, cataracts, and abnormalities in lung function. In addition, NAP can cause red blood cell rupture if inhaled or ingested in large amounts [152], [154]. One of the main concerns about this is the ability of some PAHs reactive metabolites (toxic substances produced by the body during the breakdown of food)

to bind to cellular proteins and DNA, leading to mutations, malformations, tumors, and/or cancer [152], [154], [155]. BaP was the first carcinogenic chemical discovered, and is the most common PAH that causes cancer in animals and, until 2008, the European Food Safety Authority (EFSA) used it as the only marker for the occurrence of PAHs in food [143]. However, in 2011 the EU amended the previous legislation through the EU Regulation No 835/2011, which introduced the maximum permitted levels of BaP, but also the sum of PAH4 in foodstuff, with 5 µg/kg and 35 µg/kg being the maximum levels allowed for BaP and PAH4, respectively [148].

3.1.2. Factors affecting food contamination

Food contamination can occur at different stages, from agriculture, with contamination of water, air, etc., which will result in contamination of livestock pasture; to the processing or cooking techniques of the food itself. It is therefore essential to know the content of harmful compounds in raw and unprocessed foods before scrutinizing processing/cooking techniques alone [151], [156]. Regarding processing and cooking, PAH formation depends on the type of product and its processing method, as well as other factors such as the combustible type, the oxygen levels, or the smoke generator used in the process.

Cooking techniques

The use of heat sources in the cooking of food provides several benefits, among which the following are noteworthy [157]:

- Improved sensory quality, due to changes in odor, taste, or visual appearance in contrast to the raw food.
- An improvement in nutritional quality, and it provides an aid to food digestibility and nutrient bioavailability (the rate and amount at which that nutrient, or part of it, is absorbed and becomes available at its site of action).
- Enhancement of microbiological quality by the elimination of bacteria and other organisms harmful to health.

However, some processes can lead to the formation of harmful compounds, PAHs among others, especially if they involve high temperatures [144], [158]. Cooking techniques involving heat sources can be classified in two major types: dry and wet cooking. Dry cooking refers to a direct exposure of food to heat without a thermal transfer medium, such as water or oil, and comprises the procedures of baking, roasting, grilling, or microwave use. On the contrary, wet cooking refers to the thermal food procedures using a liquid transfer medium, and comprises procedures such as boiling, poaching, stewing, braising, or steaming [157]. Regarding this, many studies have been carried out concerning the PAHs formation in various cooking methods, where almost all of them agree in the fact that wet cooking techniques are safer than dry cooking ones [156], [159]–[161].

Due to the public concern about PAH contamination, the FAO and the WHO also published a code of good practice that establishes variables that influence PAH contamination, as well as guidelines to make some cooking techniques safer [162]. In addition to the recommended cooking methods, techniques and strategies mentioned in this

document, there are other specific procedures that have shown to reduce PAH levels in food, among which the following can be highlighted:

a) Marinades

Marinating meats and fish is a very common practice used to improve the flavor, aroma and texture of products. Moreover, this technique has also been shown to have effects on the formation of PAHs, depending on the ingredients used in this pretreatment [143], [150]. Thus, marinating with ingredients that present antioxidant properties, such as spices, garlic, or onion, as well as acidic ingredients such as fruit juice, or some herbs and teas [146], have been shown to inhibit the formation of PAHs [144], [158], [163]. Conversely, other type of ingredients such as alkalines (pH > 7.5) or some oils (sodium bicarbonate, palm/sunflower oil, etc.) have been shown to produce an increase in the total amount of PAH compounds in some foods when using them in marinades [146], [164].

b) Use of additives

The addition of additives such as some water-soluble vitamins (especially pyridoxamine), molar sugar in an adequate quantity (9-15%), or sulfur-containing (like sodium bisulfite) organic compounds and nitrites have shown to mitigate the formation of heterocyclic amines during cooking processes, as explained in more detail in [165].

c) Washing/peeling

According to the EC, the JECFA, and other studies, suggest that washing the surface of smoked fish, or peeling the surface of smoked or grilled products also help to reduce the dietary amount of PAH levels in food [146], [147], [162], therefore making it safer for consumption.

d) Irradiation

Irradiation at some frequencies may also have beneficial effects in contamination levels. Gamma irradiation effects on different PAH have been investigated when irradiating wheat grains [166], or pea seeds [167]. More recently, a study carried out by Rosinka [168] measured the influence of UV radiation on PAHs in wastewater, showing that after UV radiation, a total decrease of 66.1% in the total amount of PAH concentration was achieved.

e) Packaging

The effect of the packaging material used to preserve some foods or liquids, plastics specially, may also have an effect on PAH contents. Several studies have shown that the use of different types of plastics in the packaging and preservation of food products can reduce contamination, because PAHs tend to adhere to these types of materials, especially to high-density and low-density polyethylene (HDPE and LDPE) [169], [170].

3.1.3. Detection and quantification techniques. Chromatography

Due to their great importance, PAHs have been extensively studied throughout history and there is a wide range of methods for their analysis. At present, the most widely used technique for the determination and quantification of these compounds, is chromatography.

Chromatography is an analytical technique for separation and quantification of the components of a mixture. The system is composed of two phases: the stationary phase (SP),

which hinders the passage of the components through the system; and the mobile phase (MP), which contains the sample. The different components of the MP pass through the system at different speeds, with different retention times depending on each component. It is essential that the retention time of the analyte differs from that of the other sample components. To evaluate the quality of this process, there are three key factors: the speed of the process, the economic cost of the process, and the efficiency in the separation of the components [171], [172].

Although there are several chromatographic techniques, the most commonly used for PAHs are gas chromatography (GC) and liquid chromatography (HPLC). The general operating scheme, as well as the parts of which the chromatograph equipment is composed, are shown in Figure 3.1.

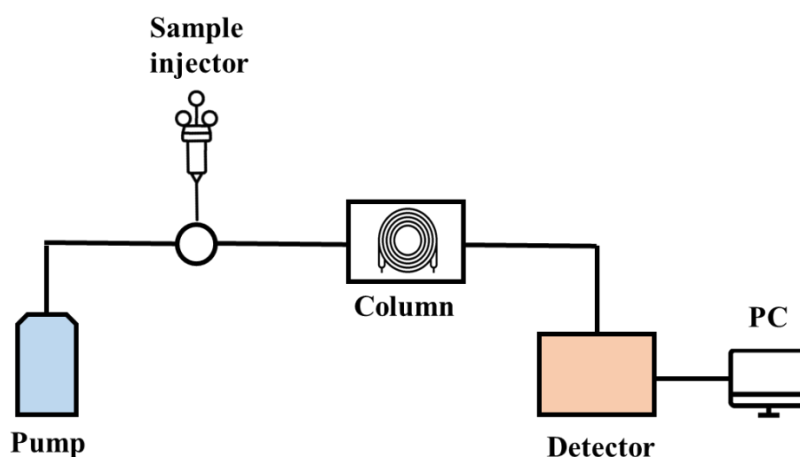


Figure 3.1: Scheme of the parts composing a chromatographic equipment. Adapted from [172].

The MP is the carrier substance of the mixture in charge of conducting it through the system. Depending on the technique used, this MP will be liquid (HPLC) or gaseous (GC). The SP, on the other hand, can be in solid (liquid-solid chromatography or gas-solid chromatography) or liquid (liquid-liquid chromatography or gas-liquid chromatography) state. The most important part of this equipment is the column, since it is the place where the separation of the different components of the mixture takes place. This column contains the SP inside, which will act as a resistor for the components of the mixture. There are two different types of columns: open tubular or capillary; and packed. The separation will be favored by the difference in chemical properties between the different molecules of the sample, as well as by their relative affinity for the SP of the column itself. The pump is the part of the equipment in charge of providing the column with a constant flow of MP. This MP may be pumped at constant speed or not, depending on the type of components in the sample to be analyzed. The injector is responsible for introducing the sample under analysis into the MP stream. Thus, once it reaches the column, the different components of the mixture will leave the column (elute from the column) at different retention times, allowing the detector to analyze each of the components independently. As for the detector, it can be of different types in both techniques (GC and HPLC), the most common being the mass spectrometer in GC, which analyzes the components by their mass-to-charge ratio; and the fluorescence detector in HPLC, which is more selective than other types because few substances emit fluorescence (some PAHs do) [173]–[175].

Because in GC the MP is gaseous (a single gas or a mixture of gases: He, Ar, N₂, H₂), most of the time the pump is replaced by a bottle containing the carrier gas(es) at the given pressure. Although this technique offers high resolution, in the case of PAHs it is difficult to

achieve PAH fragmentation without damaging the SP of the column. High temperatures would not affect PAHs (because of their high thermal stability) but they could decompose, or evaporate, the SF [172].

In contrast, the MP is liquid in the case of HPLC, so the use of a pump is necessary for the MP to flow through the column. In this technique, the sample is sometimes first passed through a pre-column in order to filter out larger particles and protect the column from chemical contaminants and particles. Thus, HPLC technique increases the separation efficiency and shortens the elution time (time it takes for the solute to enter and leave the column) without losing resolution; however, the process is more complicated and expensive [172].

There are several studies that have employed these techniques as well as multiple combinations and variants of them by the use of different stages and/or type of detectors, with results that reach very high sensitivities and can be consulted in different reviews [143], [150], but this is beyond the scope of this work.

3.2. Our work (PAPER C): Metasensor for PAH detection and identification

PAHs, when presented in food systems, have been shown to have a potential detrimental effect on human health due to its genotoxicity, and can be carcinogenic to animals and humans if the exposure to them occurs in large concentrations, or chronically. Because of this, since their discovery, they have arisen great interest within governmental and regulatory institutions that have studied them exhaustively and have regulated the maximum quantities allowed in foodstuffs. This field has also motivated a large part of the scientific community, especially those dedicated to biochemistry, health, and food technology, to search for the best alternatives for its control in human consumption. Thus, in this part of the thesis our aim is to join two very different fields of study, such as metamaterials engineering and food safety, proposing new methodologies for PAH detection and quantification, and studying their usefulness in comparison with the current official techniques.

In our work [PAPER C], we use the labyrinth metasurface designed in [PAPER A] and try to detect and identify different PAH compounds. Thus, the main objective of this work is to use this metageometry as a possible alternative to chromatography, in PAH determination. For this purpose, we made a complete experimental work, where the following tasks were undertaken:

1. **Choosing target compounds (analytes):** the compounds chosen for the study were those identified as PAH4 group (BaP, BaA, BbF, and Chr), due to their consideration within the current regulations as the most dangerous compounds and present in foodstuff.
2. **Choosing physical state of the analyte:** after making several initial tests with the pure compounds (provided by Scharlab), and making measurements with those compounds in solid state (powder), or dissolved in different solvent types, it was concluded that the most efficient way to calculate concentration and volumes (so that all measurements were made under the same conditions), was with the compounds in solution form.

3. **Choosing the best solvent:** different polar (acetone, acetonitrile) and non-polar solvents (ethyl acetate, ciclohexane) were measured alone. After testing the behavior of all of them (evaporation process and effect on the metasurface resonance, ease of cleaning, possible damages caused to the metasurface materials, etc.), a mixture of cyclohexane-ethyl acetate in a proportion of 9:1 was chosen.
4. **Choosing measurable PAH concentrations:** for each of the PAHs, lower concentrations were measured each time until the lowest level of detection allowed by our labyrinth metasurface was identified. This lowest value was of 100 $\mu\text{g}/\text{ml}$ (ppm) in the case of BaP, BaA, and Chr; and 250 ppm in the case of BbF.

For each measured compound, we poured 300 μL of the solutions at different concentrations (100 ppm, 250 ppm, 500 ppm, and 250 ppm, 500 ppm, and 1000 ppm in the case of BaP, BaA, Chr; and BbF, respectively) and let the solvent evaporate by air-drying the sample for 10 minutes. After the solvent evaporation and because the concentrations used were quite high, traces of the analyte could be observed on the surface of the metasensor, as shown in Fig. 3.2.



Figure 3.2: Images of a BbF sample on the labyrinth metasurface at concentrations of 250 ppm (left), 500 ppm (center), and 1000 ppm (right).

The results shown in this work are still very far from even approaching the legal detection levels (order of $\mu\text{g}/\mu\text{l}$). However, we wanted to open a door to the design of other possible methodologies in the detection and identification of hazardous substances present in human food. Although a much more exhaustive study is needed, by taking the design of metasurfaces to higher frequencies, it could be possible to improve the minimum detectable concentrations, getting results closer to conventional techniques.

Author contribution to this work:

- Experimental design and Sample preparation.
- Experimental characterization with an ABmm Vector Network Analyser (VNA) MVNA-8-350-4 equipped with an horizontal quasioptical bench working in the reflection configuration.
- Results validation and graphical representation.
- Manuscript preparation and writing.

Artículo eliminado por restricciones de derechos de autor

I. Jáuregui-López, K. Insausti, M. -J. Beriain and M. Beruete, "Metageometries for Polycyclic Aromatic Hydrocarbon Detection at THz Range in Food Systems," in *IEEE Sensors Letters*, vol. 5, no. 5, pp. 1-4, May 2021, Art no. 3500604, doi: 10.1109/LSENS.2021.3066698.

Chapter IV: Alternative Metasurface Designs

Up to this point, we have made an extensive review of different metasurfaces based on the paradigm of metageometries. In this section, we explore other sensor models based on alternative designs. In the first paper, we focus on the modification of the geometry of basic structures based on meta-atoms to improve the concentration of the electric field on the entire sensing surface, thus improving the metasensor sensitivity levels without the use of complex manufacture techniques.

The second paper explores the physical phenomenon of extraordinary transmission (ET), testing its potential in sensing applications through the design of structures based on subwavelength hole arrays (SHAs).

4.1. Alternative meta-atom designs

Up to this point of the thesis, we have seen that the world of metasurface design for sensing applications is very broad, and is gaining more and more importance within the research community. Whatever the type of metasensor employed, one of the biggest challenges of THz sensing is how to achieve a high-quality device in terms of sensitivity and FOM.

As seen in the previous chapters, metageometries have become a very good option to achieve these high values of sensitivity and FOM, due to the way in which the electric field is distributed along its entire surface. Although having been demonstrated to present clear advantages in terms of quality achieved in sensing applications, they are also more elaborated, and difficult to manufacture, especially at high frequencies.

We must bear in mind that in order to develop a sensing device with which to be able to detect minute thicknesses, or even living organisms as efficiently as possible, we must be able to adapt to the design of structures of similar dimensions to our targets. This implies working with designs in which the track thickness is, most of the time, less than 1 μm . In structures with intricate geometries, this process becomes tedious and complicated.

4.2. Our work (D): Sensitivity enhancement on tripod-based metasurfaces

In this work [PAPER D], we start from a very simple metasurface consisting of a tripod-based meta-atom (we called this tripod metasurfaces). Its geometry consists of three blades separated from each other by 120 degrees, as shown in Fig. 4.1.

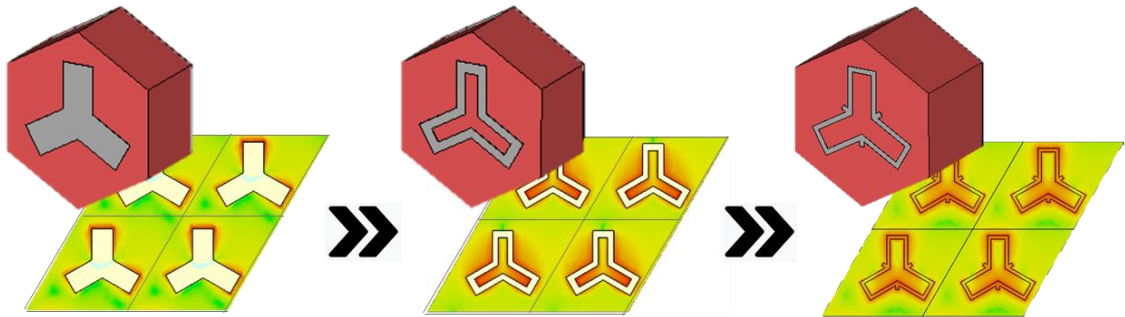


Figure 4.1. (a) Representation of the changes introduced in the tripod metasurface in [PAPER D].

We carry out modifications to its geometry to improve its detection limit and its sensitivity in thin-film sensing applications based on this design. Our objective is to obtain designs based on meta-structures that are easy to design and manufacture but whose electric field is distributed over the unit cell as much as possible. For this purpose, the design procedure in this work was done as follows:

- **Choosing a starting design:** as an initial point, we designed a solid tripod metasurface consisting of a layer of aluminum metallic blades printed over a 150 μm thick PP substrate with back metallization acting as a ground plane.
- **Hollow tripods:** another design of the same pattern of blades was made, but this time we performed a hollowed design. As shown in Fig. 4.1, by creating a cavity

between the blades, the electric field is highly concentrated inside it, resulting in an important improvement of the sensitivity.

- **Refining the design:** after several tests and modifications that are detailed in the work, as a final step, we resized the tracks widths of our design and incorporated some arms, achieving a significant increase in the field concentration and therefore, in the final sensitivity.

As a final step, we made a comparison with other similar designs found in the literature, showing that our final tripod design was on the top of the list.

According with the results achieved in this work, we corroborated that the higher the electric field concentration on the surfaces, the larger the frequency shift and sensitivity results, what emphasizes the importance of the use of metageometries with complex geometries for sensing purposes.

Author contribution to this work:

- Design of the tripod-loop initial and improved structures.
- Numerical simulations obtained with the commercial simulator CST Studio Suite.
- Results validation and graphical representation.
- Manuscript preparation and writing.

Article

Tripod-Loop Metasurfaces for Terahertz-Sensing Applications: A Comparison

Irati Jáuregui-López ^{1,2}, Bakhtiyar Orazbayev ³, Victor Pacheco-Peña ⁴  and Miguel Beruete ^{1,2,*} 

¹ Antennas Group-TERALAB, Universidad Pública de Navarra (UPNA), 31006 Pamplona, Navarra, Spain; irati.jauregui@unavarra.es

² Multispectral Biosensing Group, Navarrabiomed, Complejo Hospitalario de Navarra (CHN), Universidad Pública de Navarra (UPNA), IdiSNA, 31008 Pamplona, Navarra, Spain

³ Laboratory of Wave Engineering, École Polytechnique Fédérale de Lausanne (EPFL), 1015 Lausanne, Switzerland; bakhtiyar.orazbayev@epfl.ch

⁴ School of Mathematics, Statistics and Physics, Newcastle University, Newcastle Upon Tyne NE1 7RU, UK; Victor.Pacheco-Pena@newcastle.ac.uk

* Correspondence: miguel.beruete@unavarra.es

Received: 21 July 2020; Accepted: 15 September 2020; Published: 18 September 2020



Abstract: The high electric field intensity achieved on the surface of sensors based on metasurfaces (metasensors) makes them an excellent alternative for sensing applications where the volume of the sample to be identified is tiny (for instance, thin-film sensing devices). Various shapes and geometries have been proposed recently for the design of these metasensors unit-cells (meta-atoms) such as split ring resonators or hole arrays, among others. In this paper, we propose, design, and evaluate two types of tripod metasurfaces with different complexity in their geometry. An in-depth comparison of their performance is presented when using them as thin-film sensor devices. The meta-atoms of the proposed metasensors consist of a simple tripod and a hollow tripod structure. From numerical calculations, it is shown that the best geometry to perform thin-film sensing is the compact hollow tripod (due to the highest electric field on its surface) with a mean sensitivity of $3.72 \times 10^{-5} \text{ nm}^{-1}$. Different modifications are made to this structure to improve this value, such as introducing arms in the design and rotating the metallic pattern 30 degrees. The best sensitivity achieved for extremely thin film analytes (5–25 nm thick) has an average value of $1.42 \times 10^{-4} \text{ nm}$, which translates into an extremely high improvement of 381% with respect to the initial hollow tripod structure. Finally, a comparison with other designs found in the literature shows that our design is at the top of the ranking, improving the overall performance by more than one order of magnitude. These results highlight the importance of using metastructures with more complex geometries so that a higher electric field intensity distribution and, therefore, designs with better performance can be obtained.

Keywords: terahertz; metasurfaces; tripod; thin-film; sensing; metasensors

1. Introduction

The use of metasurfaces operating in the terahertz (THz) band for sensing applications has gained increased attention in the last few years. This is because of the recent and unprecedented advances achieved in the development of technology in this spectral region [0.1–10 THz], such as more efficient sources and detectors added to commercial instrumentation like THz time-domain spectrometers (THz-TDS) [1]. The particular characteristics of the THz band such as the sensitivity to weak molecular interactions, water absorption, and penetrability through non-polar materials, have attracted the attention of the scientific community in a wide variety of fields such as security,

medicine, communications [2], as well as sensing applications [3–9]. Metasurfaces are usually designed by assembling arrays of subwavelength resonators (meta-atoms), whose electromagnetic response can be arbitrarily manipulated by selecting the best suitable materials, geometries, and spatial arrangement. Of particular interest in sensing applications is the fact that meta-atoms produce a high electric field intensity at their resonance frequency, leading to an enhancement of the interaction of any substance or analyte under analysis placed on, or at the vicinity of, the metasurface. As a result of such light–matter interaction enhancement, observable changes in its frequency response arise. This is advantageous compared to traditional detection methods, whose main weakness lies in the difference of wavelength and analyte size: the THz wavelength size is of the order of tens to thousands of microns, whereas typical analyte sample sizes are often below one micrometer [4,5,9–12]. For this reason, there is usually not enough interaction between the radiation and the sample, and thus, the sensing becomes very difficult or even impossible.

Thin-film sensing is of high interest in practical applications, especially when measuring substances in a thin homogeneous sample becomes essential or when the sample amount is too small. Additionally, it can be used for situations in which it is easier to process a thin-film form of the sample due to the nature of the substance, such as in biological and chemical sensing [13]. There are different examples in the literature of metasurfaces designed to perform this type of sensing such as designs based on split-ring resonators (SRRs) [10,14,15], crosses [8,16], metastructures that exploit very sharp resonances such as Fano devices or hole arrays [10,17], or more complex geometries or materials such as graphene-based metasurfaces [18]. There are recent reviews that summarize all this information and the different types of device proposed in the literature [5]. Whichever the type of metasensor employed, one of the biggest challenges of THz thin-film sensing is how to achieve a high-quality device in terms of sensitivity (a parameter that gives a measure of the frequency shift compared to the response of the empty structure) and figure of merit (FOM, that relates the sensitivity and resonance linewidth). In practice, it is found that the higher the electric field confinement, the higher the sensitivity and FOM [4]. The main advantage of metastructures based on meta-atoms lies in the ease of their design and manufacture since their unit-cell geometries are not very complex. Meta-atoms based on crosses or SRRs have been extensively studied in other works [8–10,12,14–16].

Motivated by the promising capabilities of metasurfaces for sensing and their importance for thin-film detection at THz frequencies, in this work we propose metasensors using meta-atoms with a geometry consisting of three blades separated from each other by 120 degrees, called “tripod metasurfaces”. An in-depth comparison between different types of tripod-loop metasurfaces is performed by studying metastructures with increasingly complex geometries: from simple tripod metasurfaces made of solid blades (arms) to a hollow tripod metasurface where the electric field confinement will be shown to be much higher. To carry out a qualitative comparison, we study the behavior of both metastructures as thin-film sensing devices. As a final step, we analyze more complex tripod metastructures, to which we add arms or rotations in the metallic pattern (hollow tripod + arms, hollow tripod + arms, rotated) and compare their performance with other designs found in the literature.

2. Materials and Methods

The metasensors proposed in this work are designed to operate in absorption within the THz band of 0.4–0.7 THz. All metastructures were configured as tri-layer designs consisting of a layer of aluminum (Al) metallic blades printed over a 150 μm thick polypropylene (PP) substrate with back metallization acting as a ground plane. It is important to note that metals within the designed THz frequency range can still be considered as conductors that can be modeled using finite conductivity [4,19], hence the back metallic sheet acts as a reflecting layer. The structure dimensions are: periodicity, $d = 162.5 \mu\text{m}$; distance between metallic strips, $a = 26 \mu\text{m}$; metallic strips width, $g = 9.5 \mu\text{m}$; metallic layers thickness, $t = 0.4 \mu\text{m}$; and blade width, $w = 58.5 \mu\text{m}$; as shown in Figure 1.

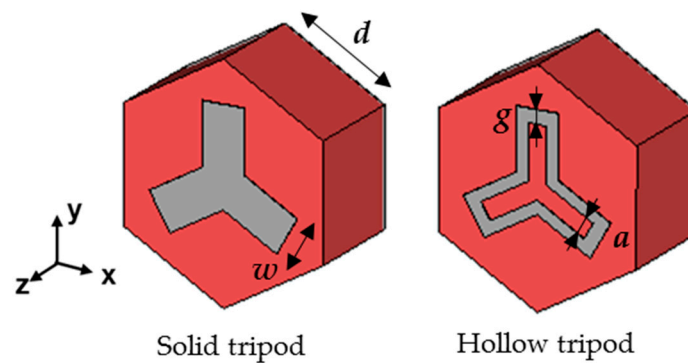


Figure 1. Front view of the designed tripod metasurfaces unit cells. Metallization is represented in grey and polypropylene (PP) substrate in red.

The designed metasurfaces are simulated using the commercial simulator CST Microwave Studio™. Floquet ports and periodic boundary conditions are applied to the designed unit cells to model the metasurfaces as an infinitely replicated array. The PP substrate was modeled as a low-loss dielectric with a complex relative permittivity $\epsilon_{PP} = 2.25(1 - j10^{-3})$. The aluminum used for the pattern and the ground plane was modeled as a lossy metal with electrical conductivity $\sigma = 1.5 \times 10^7$ S/m, as in [4,19] with the nominal conductivity of aluminum reduced to account for losses due to roughness. The metasurfaces were illuminated under normal incidence using a vertically polarized (E_y) plane wave. To evaluate the performance of the designed metasurfaces working as thin-film sensors, their outer face was coated with different thin-film thicknesses, ranging from 200 nm to 800 nm. The dielectric permittivity of the analyte used for this purpose was $\epsilon_a = 8$, as this value has been used in other studies dealing with biosensing applications [19,20].

3. Results and Discussion

The numerical results of the reflection coefficient for the designed metasensors are shown in Figure 2. As shown in the figure (black curves), the response of the analyte-free metastructures exhibits a dip in the reflection coefficient at 551 GHz (hollow tripod, Figure 2b) and 620 GHz (solid tripod, Figure 2a). Before coating the surfaces with different analyte thicknesses, a study of the electric field distribution over the surface of the analyte-free structure was carried out, and the results are shown as insets in the same figure. As shown in Figure 2a,b, there are apparent differences between both metastructures. While in the solid tripod metastructure (Figure 2a) the electric field is confined only at the tips of the metallic blades, in the hollow tripod structure, the electric field is also confined inside the hollow blades, due to the capacitance generated between the metallic strips (see Figure 2b).

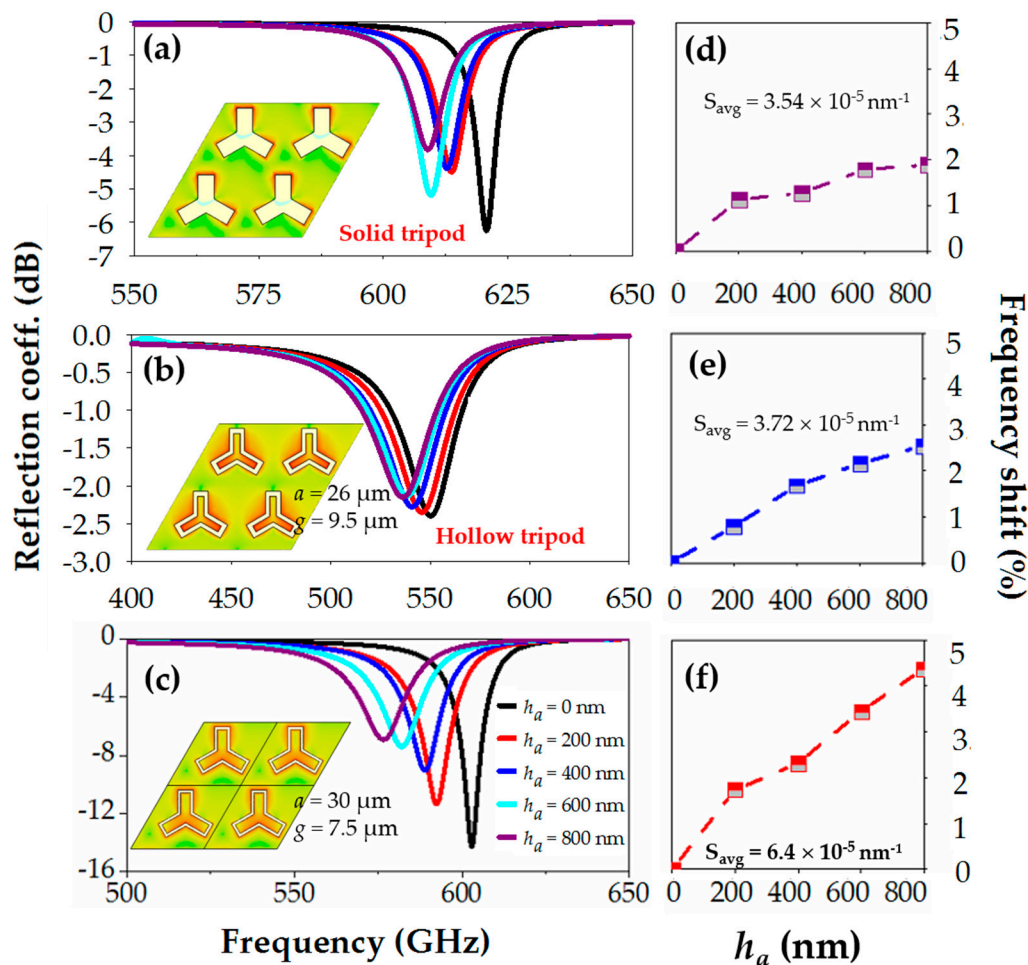


Figure 2. Reflection coefficient for different analyte thicknesses: 0 nm (black line), 200 nm (red line), 400 nm (blue line), 600 nm (cyan line), and 800 nm (dark pink line), for the solid tripod structure (a), and the hollow tripod structures (b,c). Insets: electric field magnitude over the empty (analyte-free) tripod metasurfaces. Frequency shift as a function of the analyte thickness, for extremely thin analytes with average sensitivity for the solid tripod structure (d), and the hollow tripod structures (e,f).

When using this type of unit cells for sensing applications, it becomes essential to have the maximum possible electric field concentration to increase the sensitivity to dielectric changes in the vicinity of its surface. The sensing performance of both metastructures was studied by coating them with a dielectric thin-film acting as an analyte, with dielectric permittivity $\epsilon_a = 8$, and thicknesses ranging from $h_a = 200$ nm to $h_a = 800$ nm. The reflection spectra for the different analyte thicknesses are plotted in Figure 2a,c. As observed, a redshift of the resonance dip occurs when the analyte thickness increases, as expected. For completeness, this frequency shift as a function of the analyte thickness is plotted in Figure 2d,e where the redshift is clearly shown. To obtain a quantitative estimation of the sensing performance, we calculate the sensitivity of each structure, defined as $S = (\Delta f/f_0)/h_a$ and measured in nm^{-1} , where $\Delta f = f - f_0$, with f the resonance frequency for each analyte thickness, h_a , and f_0 the resonance frequency without the analyte. With this definition, we obtain an average sensitivity of $3.54 \times 10^{-5} \text{ nm}^{-1}$ for the solid tripod structure, and an average sensitivity of $3.72 \times 10^{-5} \text{ nm}^{-1}$ for the hollow tripod structure. These results translate into an improvement of the hollow structure of approximately 5% with respect to the solid tripod. As mentioned above, this can be because the electric field confinement is more distributed along the surface of the hollow tripod, making it more sensitive to changes in the refractive index around the surface of the structure.

The previous results suggest that one of the most critical factors for a good sensing device is to have large electric field confinement. To verify this, new metastructures were designed, based on the hollow tripod. First, we modify the strip width g (see dimensions in Figure 1) and the gap between strips, a , to optimize these parameters, and to achieve as deep a resonance as possible. Based on this analysis, it was found that the best dimensions are those in the inset of Figure 2e with: $a = 30 \mu\text{m}$ and $g = 7.5 \mu\text{m}$. As observed in the curves of the reflection coefficient for different analyte thicknesses (Figure 2c), the frequency shift obtained is significantly larger than in the previous cases. Specifically, a maximum frequency shift of 4.36% is achieved for an analyte thickness of 800 nm (Figure 2f). This provides a mean sensitivity of $6.4 \times 10^{-5} \text{ nm}^{-1}$, giving rise to a 172% improvement regarding the hollow structure. In addition to being easy to design and manufacture, this structure is largely insensitive to the angle of polarization (as shown in the Supplementary Material), which is advantageous for sensing applications where it is vitally important to position the sample in the correct alignment.

Once the optimal dimensions of the structure have been found, we continue this work by introducing changes in the design to improve the sensitivity and, therefore, the quality of the metasensor device. One way to enhance the electric field concentration is by adding arms to each of the three vertexes of the metallic pattern, as shown in the insets of Figure 3. In order to know the optimal length of these arms, we performed a parameter sweep of their length. The length of the arms (l_{arm}) varied from $5 \mu\text{m}$ up to the maximum, limited by the size of the unit cell, see Figure 3. The best results were achieved for an arm's length equal to or less than $10 \mu\text{m}$, obtaining a higher quality factor resonance in the bare structure. Thus, due to the greater ease of manufacture, we have chosen an arm's length of $10 \mu\text{m}$.

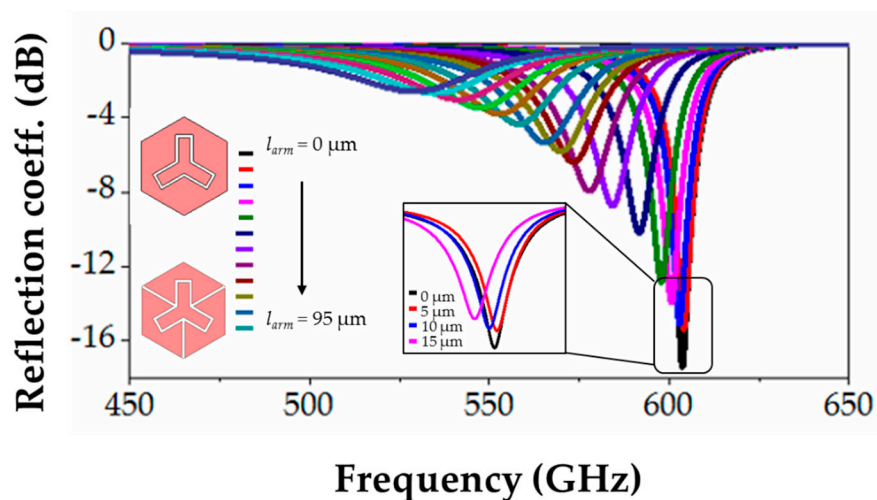


Figure 3. Reflection coefficient for different arm lengths (linear sweep from 0 to $95 \mu\text{m}$) of the hollow tripod structure. Insets: schematic representation for arm lengths of $0 \mu\text{m}$ (top) and $95 \mu\text{m}$ (bottom).

To compare the sensitivity achieved with the previous metastructures, we coated the new design with the same analyte thicknesses as before, obtaining the reflection coefficient results plotted in Figure 4a. When varying the analyte thickness between 200 and 800 nm, a maximum frequency shift of 5.09 GHz was obtained (see Figure 4c) with a mean sensitivity of $7.32 \times 10^{-5} \text{ nm}^{-1}$, leading to an improvement of 196% with respect to the hollow tripod. As can be observed in Figure 4a, this structure allows us to detect much thinner thicknesses than 200 nm, so we coated the structure with very thin films, with thicknesses ranging from 5 nm to 25 nm. The reflection coefficient and corresponding frequency shifts for these thicknesses can be seen in the inset of Figure 4a. With these results, we calculate a mean sensitivity of $1.27 \times 10^{-4} \text{ nm}^{-1}$ (improvement of 341% respect to the hollow tripod structure, which is not able to detect such ultrathin thicknesses, as shown in the supplementary material). As a final step, we rotate the metallic pattern of the metasurface unit cell 30° to perform the last comparison. The reflection coefficient and frequency shift achieved are shown in Figure 4b,d.

As observed, the performance of this design is similar to the previous one (without rotation), which agrees with the results found in [21] for single particles (non-periodic) plasmonic tripods with C_3 rotational symmetry. If we calculate the maximum frequency shift and the mean sensitivity again, the resulting values are 5.1 GHz, and $7.35 \times 10^{-5} \text{ nm}^{-1}$ for analyte thicknesses between 200 and 800 nm, respectively, which are approximately identical to the previous case. The mean sensitivity with very thin films (5 to 25 nm) was also calculated obtaining a mean value of $1.42 \times 10^{-4} \text{ nm}^{-1}$, leading to an improvement of 381% with respect to the hollow tripod, and thus becoming the best option for sensing applications. Table 1 summarizes the maximum frequency shift and sensitivity achieved for the different metastructures studied in this work.

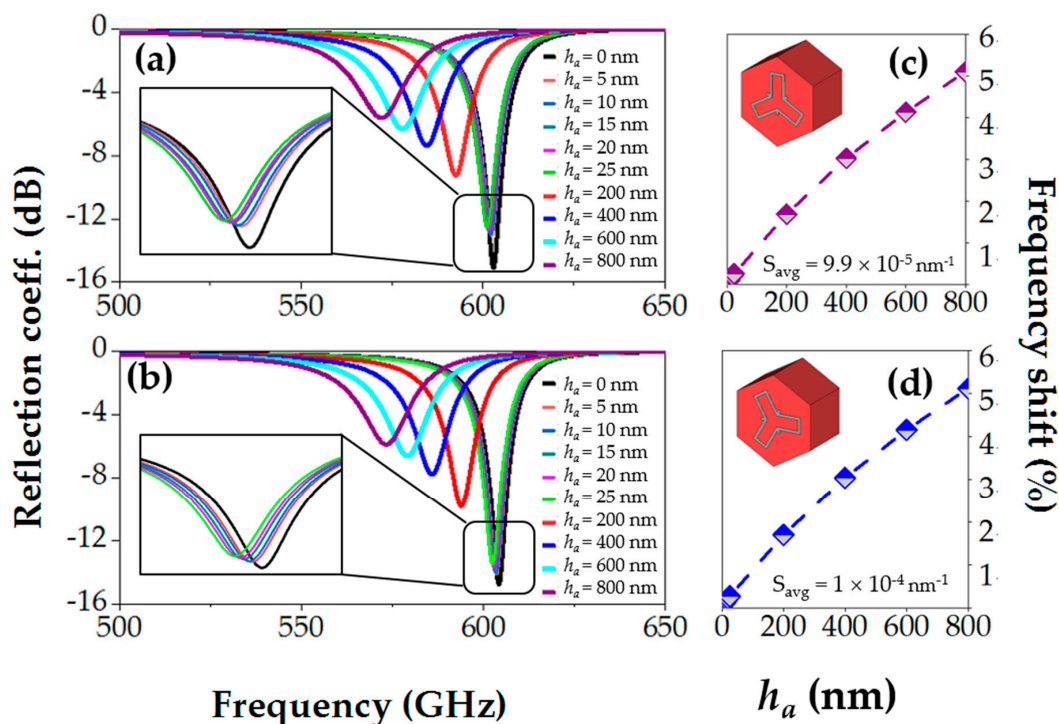


Figure 4. Reflection coefficient for different analyte thicknesses for the hollow tripod structure with arms (a), and the hollow tripod structure with arms, and rotated (b). Insets: zoom of the reflection coefficient for both metastructures and extremely thin film analytes (0–25 nm). Frequency shift as a function of the analyte thickness, with average sensitivity for the hollow tripod structure with arms (c), and the hollow tripod structure with arms, and rotated (d).

Table 1. Comparison of the most relevant quality parameters of the three tripod-metastuctures studied in this work when working as thin-film sensors where the analyte thickness deposited varies between 200 and 800 nm (top), and for ultra-thin analytes between 5 and 25 nm (bottom).

h_a (nm)	Tripod Structure	Δf max (%)	Mean Sensitivity (nm^{-1})
200–800	Solid	1.89	3.54×10^{-5}
	Hollow $a = 26 \mu\text{m}$	2.55	3.72×10^{-5}
	Hollow $a = 30 \mu\text{m}$	4.36	6.40×10^{-5}
	Hollow + arms	5.09	7.32×10^{-5}
	Hollow + arms, rotated	5.11	7.35×10^{-5}
5–25	Hollow + arms	0.50	1.27×10^{-4}
	Hollow + arms, rotated	0.60	1.42×10^{-4}

As a final step, a comparison with other works found in the literature was carried out, in which similar designs in terms of complexity and dimensions were analyzed (note that we tried to keep

the dimensions compatible with standard photolithography techniques). To make a fair comparison of all designs, we used a new sensitivity definition that also takes into account the operational frequency, and the analyte refractive index (otherwise, we would be benefiting those works in which the refractive index is higher) as $S = (\Delta f/f_0)/(h_a \cdot n_a)$, with h_a the analyte thickness, and n_a the analyte refractive index. This comparison can be seen in Table 2. As shown, this work could be on the top of the ranking, achieving a high sensitivity for thicknesses of analyte several orders lower than other designs. A possible explanation for this better performance could be that the hollow tripod has a field distribution with more distributed hot spots along the unit cell and not concentrated at small areas, similar to what happened in our previous paper [4].

Table 2. Comparison of different values of sensitivity achieved in different works, calculated as $S = (\Delta f/f_0)/(h_a \cdot n_a)$, with h_a the analyte thickness and n_a the analyte refractive index, in refractive index units (RIU), and ordered chronologically.

Reference	h_a (nm)	n_a (RIU)	f_0 (GHz)	Δf (GHz)	Sensitivity (nm·RIU) ⁻¹
Ref [22], 2018	2000	1.01	2250	16	3.52×10^{-6}
Ref [23], 2018	16 000	1.6	2260	200	3.45×10^{-6}
Ref [24], 2019	250	1.6	396	1	6.3×10^{-6}
Ref [7], 2019	10 000	1.4	1550	10	4.6×10^{-7}
Ref [12], 2019	7	8	1000	3	5.35×10^{-5}
This work	5	$\sqrt{8}$	604	0.6	7×10^{-5}

4. Conclusions

To conclude, we have reported in this work three different tripod-based metasurfaces working as thin-film sensors in the THz band. We have shown that the higher electric field concentration on the surfaces, the larger the frequency shift, and sensitivity results. To corroborate this fact, two different metastructures have been initially studied, a solid tripod and a hollow tripod metasurface, with higher electric field confinement, obtaining average sensitivities of $3.54 \times 10^{-5} \text{ nm}^{-1}$ and $3.72 \times 10^{-5} \text{ nm}^{-1}$, respectively. Other metastructures have been designed, to improve the sensitivity, by changing the unit cell parameters, including additional elements in the metallic pattern of the unit cell, such as arms, or rotating the structure pattern, thus obtaining the best design with an average sensitivity of 1.42×10^{-4} when measuring extremely thin analytes, meaning an improvement of 381% with respect to the initial hollow tripod structure. Finally, we have performed a comparison with other designs found in the literature, with similar complexity and dimensions, showing that our designed structure is on top of the list, improving most of the previous works by more than one order of magnitude. These results emphasize the importance of using metastructures with complex geometries for sensing applications, in which the electric field is distributed throughout the surface and not only at discrete points, such as metageometries.

Supplementary Materials: The following are available online at <http://www.mdpi.com/2076-3417/10/18/6504/s1>: Figure S1: Spectral transmission of the simple tripod metasurface plotted as a function of the polarization angle. Figure S2: Reflection coefficient for different ultrathin analyte thicknesses.

Author Contributions: Conceptualization, I.J.-L., B.O., V.P.-P. and M.B.; methodology, I.J.-L. and M.B.; software, I.J.-L.; validation, B.O., V.P.-P. and M.B.; formal analysis, I.J.-L., B.O., V.P.-P. and M.B.; investigation, I.J.-L., B.O., V.P.-P. and M.B.; resources, I.J.-L., B.O., V.P.-P. and M.B.; data curation, I.J.-L.; writing—original draft preparation, I.J.-L. and M.B.; writing—review and editing, I.J.-L., B.O., V.P.-P. and M.B.; visualization, I.J.-L.; supervision, B.O., V.P.-P. and M.B.; project administration, M.B.; funding acquisition, M.B. All authors have read and agreed to the published version of the manuscript.

Funding: This research was funded by Spanish Ministerio de Ciencia, Innovación y Universidades, Project RTI2018-094475-B-I00 (MCIU/AEI/FEDER,UE).

Conflicts of Interest: The authors declare no conflict of interest. The funders had no role in the design of the study; in the collection, analyses, or interpretation of data; in the writing of the manuscript; or in the decision to publish the results.

References

1. Ho, L.; Pepper, M.; Taday, P. Terahertz spectroscopy: Signatures and fingerprints. *Nat. Photon.* **2008**, *2*, 541–543. [[CrossRef](#)]
2. Saeedkia, D. *Handbook of Terahertz Technology for Imaging, Sensing and Communications*; WP Woodhead Publishing: Cambridge, UK, 2013; ISBN 9780857092359.
3. Yan, X.; Yang, M.; Zhang, Z.; Liang, L.; Wei, D.; Wang, M.; Zhang, M.; Wang, T.; Liu, L.; Xie, J.; et al. The terahertz electromagnetically induced transparency-like metamaterials for sensitive biosensors in the detection of cancer cells. *Biosens. Bioelectron.* **2019**, *126*, 485–492. [[CrossRef](#)] [[PubMed](#)]
4. Jáuregui-López, I.; Rodríguez-Ulibarri, P.; Urrutia, A.; Kuznetsov, S.A.; Beruete, M. Labyrinth Metasurface Absorber for Ultra-High-Sensitivity Terahertz Thin Film Sensing. *Phys. Status Solidi Rapid Res. Lett.* **2018**, *12*, 1800375. [[CrossRef](#)]
5. Beruete, M.; Jáuregui-López, I. Terahertz Sensing Based on Metasurfaces. *Adv. Opt. Mater.* **2019**, *1900721*, 1900721. [[CrossRef](#)]
6. Papari, G.P.; Koral, C.; Andreone, A. Encoded-enhancement of THz metasurface figure of merit for label-free sensing. *Sensors* **2019**, *19*, 2544. [[CrossRef](#)]
7. Islam, M.S.; Sultana, J.; Biabanifard, M.; Vafapour, Z.; Nine, M.J.; Dinovitser, A.; Cordeiro, C.M.B.; Ng, B.W.H.; Abbott, D. Tunable localized surface plasmon graphene metasurface for multiband superabsorption and terahertz sensing. *Carbon* **2020**, *158*, 559–567. [[CrossRef](#)]
8. Rodríguez-Ulibarri, P.; Kuznetsov, S.A.; Beruete, M. Wide angle terahertz sensing with a cross-dipole frequency selective surface. *Appl. Phys. Lett.* **2016**, *108*, 111104. [[CrossRef](#)]
9. Srivastava, Y.K.; Cong, L.; Singh, R. Dual-surface flexible THz Fano metasensor. *Appl. Phys. Lett.* **2017**, *111*, 1–6. [[CrossRef](#)]
10. Gupta, M.; Srivastava, Y.K.; Manjappa, M.; Singh, R. Sensing with toroidal metamaterial. *Appl. Phys. Lett.* **2017**, *110*, 121108. [[CrossRef](#)]
11. Hong, J.T.; Jun, S.W.; Cha, S.H.; Park, J.Y.; Lee, S.; Shin, G.A.; Ahn, Y.H. Enhanced sensitivity in THz plasmonic sensors with silver nanowires. *Sci. Rep.* **2018**, *8*, 1–8. [[CrossRef](#)]
12. Srivastava, Y.K.; Ako, R.T.; Gupta, M.; Bhaskaran, M.; Sriram, S.; Singh, R. Terahertz sensing of 7 nm dielectric film with bound states in the continuum metasurfaces. *Appl. Phys. Lett.* **2019**, *115*, 1–17. [[CrossRef](#)]
13. O'Hara, J.F.; Withayachumnankul, W.; Al-Naib, I.A.I. A Review on Thin-film Sensing with Terahertz Waves. *J. Infrared Millim. Terahertz Waves* **2012**, *33*, 245–291. [[CrossRef](#)]
14. Singh, R.; Cao, W.; Al-Naib, I.A.I.; Cong, L.; Withayachumnankul, W.; Zhang, W. Ultrasensitive terahertz sensing with high-Q Fano resonances in metasurfaces. *Appl. Phys. Lett.* **2014**, *105*, 171101. [[CrossRef](#)]
15. Kim, N.; In, S.; Lee, D.; Rhie, J.; Jeong, J.; Kim, D.S.; Park, N. Colossal Terahertz Field Enhancement Using Split-Ring Resonators with a Sub-10 nm Gap. *ACS Photon.* **2018**, *5*, 278–283. [[CrossRef](#)]
16. Cong, L.; Tan, S.; Yahiaoui, R.; Yan, F.; Zhang, W.; Singh, R. Experimental demonstration of ultrasensitive sensing with terahertz metamaterial absorbers: A comparison with the metasurfaces. *Appl. Phys. Lett.* **2015**, *106*, 031107. [[CrossRef](#)]
17. Jáuregui-López, I.; Rodríguez-Ulibarri, P.; Kuznetsov, S.A.; Nikolaev, N.A.; Beruete, M. THz Sensing With Anomalous Extraordinary Optical Transmission Hole Arrays. *Sensors* **2018**, *18*, 3848. [[CrossRef](#)]
18. Xu, W.; Xie, L.; Zhu, J.; Tang, L.; Singh, R.; Wang, C.; Ma, Y.; Chen, H.T.; Ying, Y. Terahertz biosensing with a graphene-metamaterial heterostructure platform. *Carbon* **2019**, *141*, 247–252. [[CrossRef](#)]
19. Jáuregui-López, I.; Rodríguez-Ulibarri, P.; Kuznetsov, S.A.; Quemada, C.; Beruete, M. Labyrinth Metasurface for Biosensing Applications: Numerical Study on the New Paradigm of Metageometries. *Sensors* **2019**, *19*, 4396. [[CrossRef](#)]
20. Park, S.J.; Hong, J.T.; Choi, S.J.; Kim, H.S.; Park, W.K.; Han, S.T.; Park, J.Y.; Lee, S.; Kim, D.S.; Ahn, Y.H. Detection of microorganisms using terahertz metamaterials. *Sci. Rep.* **2014**, *4*, 4988. [[CrossRef](#)]
21. Pacheco-Peña, V.; Fernández-Domínguez, A.I.; Luo, Y.; Beruete, M.; Navarro-Cía, M. Aluminum Nanotriods for Light-Matter Coupling Robust to Nanoemitter Orientation. *Laser Photon. Rev.* **2017**, *11*, 1700051. [[CrossRef](#)]
22. Jin, B.; Tan, W.; Zhang, C.; Wu, J.; Chen, J.; Zhang, S.; Wu, P. High-Performance Terahertz Sensing at Exceptional Points in a Bilayer Structure. *Adv. Theory Simul.* **2018**, *1*, 1800070. [[CrossRef](#)]

23. Janneh, M.; De Marcellis, A.; Palange, E.; Tenggara, A.T.; Byun, D. Design of a metasurface-based dual-band Terahertz perfect absorber with very high Q-factors for sensing applications. *Opt. Commun.* **2018**, *416*, 152–159. [[CrossRef](#)]
24. Al-Naib, I. Evaluation of amplitude difference referencing technique with terahertz metasurfaces for sub-micron analytes sensing. *J. King Saud Univ. Sci.* **2019**, *31*, 1384–1387. [[CrossRef](#)]



© 2020 by the authors. Licensee MDPI, Basel, Switzerland. This article is an open access article distributed under the terms and conditions of the Creative Commons Attribution (CC BY) license (<http://creativecommons.org/licenses/by/4.0/>).

4.3. Extraordinary Transmission Metasurfaces for sensing

4.3.1. Extraordinary transmission phenomena

An alternative way to design metasurface-based THz sensors with interesting and competitive characteristics is to exploit the so called extraordinary transmission, a phenomenon discovered in 1998 by T.W. Ebbesen [176]. After the first evidence of ET, extensive research has been conducted on it. ET is manifested as high transmittance peaks arising in the cutoff region of thin metallic plates perforated with a periodic matrix of subwavelength holes. In other words, ET can be defined as the ability to transmit waves through sub-wavelength holes drilled in a metal plate. Therefore, high transmittance is observed below the cutoff of the holes.

This first experimental realization was done for the first time in the infrared range [176] and was explained as a result of the coupling of the incident light to surface plasmon polaritons (SPPs), supported by the periodic metallic surface. At optical frequencies (as well as in microwaves and millimeter waves), metals are known to behave differently than at lower frequencies such as microwaves and millimeter waves. In fact, electrons are not attached to the nucleus, but move freely in the conduction band, as in a plasma medium. Thus, the finite conductivity model has to be modified by more accurate models, such as a Drude dispersion model. Particularly, Drude's effective permittivity, ε_d is defined as shown in equation 4.1:

$$\varepsilon_d(\omega) = \varepsilon_\infty - \frac{\omega_p^2}{\omega^2 - j\omega\gamma_c}, \quad (4.1)$$

where ω_p is the plasma frequency [$\varepsilon_d(\omega_p) \approx 0$] and γ_c is the collision frequency which accounts for damping effects due to the collision between electrons in motion.

However, it was soon noticed that the phenomenon of ET was more general and could exist in other frequency ranges such as microwaves and millimeter waves where metals admit both a Drude and a high conductivity model, although for simplicity they are usually described assuming high conductivity. Indeed, the theoretical derivation proposed by L. Martin-Moreno *et al.* in [177], already predicted similar peaks even with a perfect electric conductor metal model. This opened the way toward the replica of the ET resonance all along the electromagnetic spectrum. M. Beruete *et al.* [178] replicated the experiment in the millimeter wave range where SPPs could not take place, since at these frequencies metals are modeled by a classical finite conductivity model. Thus, the ET phenomenon was then explained in terms of classical complex wave theory, instead of a model based on SPPs excitation. Subsequently, a new perspective of equivalent circuit concepts was proposed in [179] by reducing the periodic problem to a single unit cell of an equivalent virtual waveguide with a circular diaphragm inside.

4.3.2. Subwavelength Hole Array metamaterials

Generally speaking, the fundamental difference between the metasurfaces studied up to this point and ET SHAs lies in the type of resonance supported by the structure. Conventional metasurface-based sensors rely on the excitation of local self-resonances supported by the unit cell elements. This means that the effect of the periodic structure is

second-order as, loosely speaking, the exact frequency location is marked by each resonator and the coupling between them mainly affects the resonance bandwidth. In contrast, the ET resonance is a collective effect that arises due to the interaction of the overall structure because, by definition, each element is non-resonating (recall that the extraordinary fact of this resonance is that the apertures are working in cutoff which inherently implies that the holes must be non-resonating). More specifically, the ET peak can be explained as the interaction between the incident wave and leaky-modes excited by the periodic hole matrix that run along the surface as they leak away energy from it [180]. In this sense, it is remarkable that the operation of metageometries such as the labyrinth metasurface mentioned before are midway between self-resonances and collective resonances. In fact, metageometries consist of the periodic replication of a unit cell but it is clear from the field analysis that the energy distribution is spread along the unit cell and not confined exclusively at some particular spots. In other words, there are internal interactions in the unit cell that contribute to the resonance process, and furthermore, although these interactions might change depending on the polarization of the incident wave, the frequency response remains unaltered, giving an indication of a collective response of the intricate structure that composes the unit cell.

Returning now to ET SHAs and focusing now on sensing applications, the first realization of a thin-film sensor based on this resonance operating at the THz band was published by Miyamaru *et al.* in 2006 [181]. The structure used in that work was a metal sheet 500 μm thick perforated with an array of circular holes with a diameter of 680 μm distributed along a triangular array with a periodicity of 1130 μm . To demonstrate the sensitivity of the metallic grid to variations near the surface, it was coated with two different paper sheets 240 μm thick, one clear and another printed. As the printed paper possessed an estimated ink thickness of less than 5 μm , the transmission response experienced a slight frequency shift to lower frequencies with respect to the bare paper. Remarkably, in the comparison between the bare hole array response and the hole array with a clear paper on top, it was noticed that the frequency response of both cases was almost identical. Thus, it was concluded that the structure was capable of detecting extremely small amounts of substance (ink) in thin films.

Miyamaru *et al.* also studied the effect of dielectric thin-films on the reflection properties of hole arrays in 2010 [182]. In particular, they investigated the dependence of the sensing performance of the structure on the SHA thickness and the side on which the analyte is deposited. They found that when working in transmission configuration the redshift in the frequency response was also accompanied by a significant attenuation as the thickness of the polypropylene was increased. This attenuation can be explained due to two different reasons: the cutoff effect of the metal holes and the mismatch between both sides of the structure. This effect does not become so important in the reflection spectrum, which shows that for sensing purposes, working in reflection configuration may be a better option in terms of signal-to-noise ratio. However, when placing the analyte film on the non-illuminated side of the metal, the reflection dip became very weak due to the fact that the contribution of that side of the structure is much smaller. This presents a huge disadvantage for high-sensitivity applications, even though this problem could be resolved by the use of thinner dielectric films, where the mismatch between both sides of the structure is reduced.

More recently, a study of a structure composed of two stacked hole arrays (i.e., the so-called fishnet structure) was also evaluated for thin-film sensing applications, by depositing a thin film overlayer and studying numerically and experimentally both the amplitude modulation and the frequency shift of the spectral response. This study by Yahiaoui *et al.*

[183] showed that both sensing strategies, amplitude and frequency modulation, could be successfully used for thin-film sensing purposes.

Up to this point, we have only considered SHAs with identical periodicity in both axes. Nevertheless, SHAs with a rectangular unit cell such as the one shown in Fig. 4.2 have a richer physical behavior and open novel possibilities for applications, among them sensing. One of the first reports on rectangular SHAs was published in the context of miniaturized and low-loss fishnet metamaterials [184].

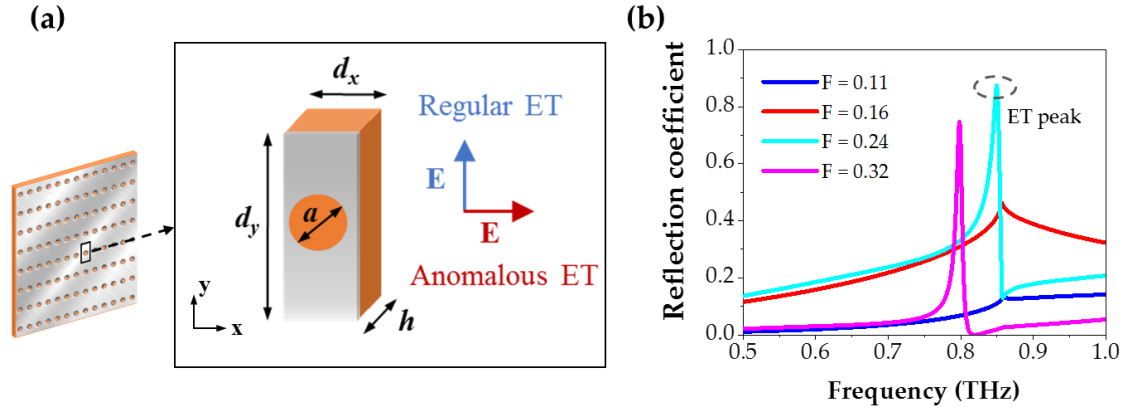


Figure 4.2. (a) Schematic representation of SHAs in rectangular lattice, and illustration of a single unit cell with relevant dimensions and polarization options. (b) Anomalous ET for SHA with $d_y = 350 \mu\text{m}$, and different slab thicknesses for $F = 0.11$, $F = 0.16$, $F = 0.24$, and $F = 0.32$.

However, the interest in rectangular SHAs spurred some years later while studying the frequency response of doubly periodic single-layer SHAs supported by a polypropylene slab. Interestingly, two different resonances were identified, each one of them corresponding to orthogonal polarizations along the two principal unit cell lattice vectors. The resonance associated with the polarization parallel to the large SHA periodicity was identified as the normal ET resonance, and thus it was termed as regular ET. It occurs when the distance between the holes in the structure is comparable to the wavelength and is much larger than the hole size, being unnecessary the presence of any substrate [182], [183], [185]. Additionally, if the structure is loaded with a dielectric slab and the polarization is parallel to the short SHA periodicity, an unexpected resonance peak was noticed in the spectrum. This came as a surprise because for this polarization the periodicity of the SHA would not be compatible with ET and, in fact, it did not appear in previous reports [184]. This fact led to the denomination of this resonance as “anomalous ET”. After several analytical and experimental studies, now it is clear that this phenomenon is tightly linked to the excitation of a grounded dielectric slab surface wave that becomes leaky due to the periodic structure [186], [187], and its appearance depends on the dielectric slab characteristics (h and ε) as well as the large SHA periodicity, d_y (see Fig. 4.2). Concretely, an auxiliary factor can be defined [186] as follows (equation 4.2):

$$F = \frac{h\sqrt{\varepsilon - 1}}{d_y} \quad (4.2)$$

Consequently, if $F > 0.25$, the spectrum will show a peak of transmission followed by a null (also known as Wood’s anomaly), as showed by the pink line of Fig. 4.2. Nonetheless, if

$F < 0.25$, a peak of transmission will not take place in the spectrum (blue and red line), but a local maximum can emerge at that frequency.

4.4. Our work (E): ET based Hole Array metasurface

The anomalous ET resonance contributes to the rich variety of possibilities offered by SHAs for the design and test of sensing devices. Before, we have seen examples where one can use one face or another for deposition, or excite different resonances or even use frequency or amplitude modulation for sensing. The question one can then ask is: what is the best strategy? The truth is that there is not a single optimal approach suitable for all cases and, rather, the best solution will depend on the application scenario.

In our work [PAPER E], we present a comprehensive analysis of the sensing capabilities of SHAs operating at both regular and anomalous ET by coating our SHA surface with different thicknesses of a photoresist material, ranging from 3 μm to 13 μm . For that, we tested different types of structures and deposition and polarization scenarios trying to discover the best one for thin-film sensing applications:

- **Two SHA designs:** we designed and manufactured two aluminum SHAs laying on polypropylene (PP) slabs of two different thicknesses, 50 and 75 μm . These two thicknesses allowed us to have a SHA where the anomalous ET resonance is deeply in cutoff (50 μm); and a second SHA where the anomalous ET is also below but near the cutoff condition (75 μm).
- **Two polarization options:** we considered both vertical and horizontal polarizations in order to excite both regular and anomalous ET, respectively. With the results achieved, the anomalous ET resonance seemed to allow greater sensitivity values, and the possibility of sensing in amplitude in those cases in which the resonance is deeply in cutoff ($F \ll 0.25$).
- **Two deposition options:** one in which the analyte was placed on the non-patterned side of the SHA (physical equivalent to increasing the substrate thickness); and another where the analyte was deposited on the patterned side of the SHA (achieving better impedance matching of both sides of the structure), as shown in Fig. 4.3.

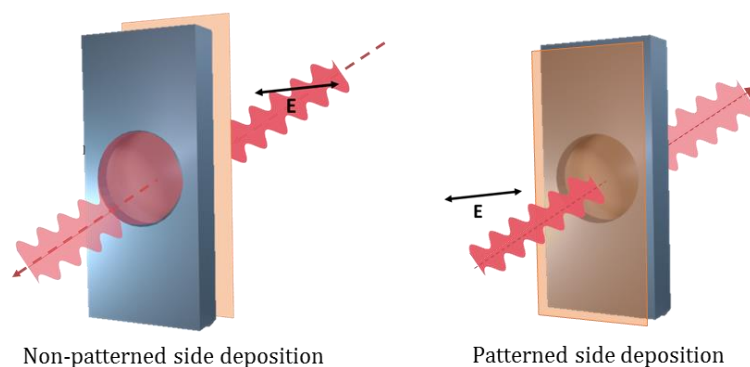


Figure 4.3. Schematic representation of designed SHAs and the two deposition methods employed in this work.

According to all the cases studied, the best performance (with a maximum frequency shift) was achieved when the analyte was deposited on the polypropylene side of the 75 μm thick metasurface. This result can be easily explained by considering the mentioned effect



of the substrate on the appearance of the anomalous ET resonance. As said above, to excite it, one needs a minimum substrate thickness and in the case considered, 75 μm is near but not sufficiently thick enough. Certainly, depositing the analyte on top of the substrate layer can be considered equivalent to increasing the overall dielectric thickness, breaking the cutoff condition, and exciting effectively the anomalous extraordinary transmission peak.

Author contribution to this work:

- Hole Array metasurfaces design.
- Numerical simulations obtained with the commercial simulator CST Studio Suite.
- Results validation and graphical representation.
- Manuscript preparation and writing.

Article

THz Sensing With Anomalous Extraordinary Optical Transmission Hole Arrays

Irati Jáuregui-López ¹, Pablo Rodríguez-Ulibarri ¹, Sergei A. Kuznetsov ^{2,3}, Nazar A. Nikolaev ⁴ 
and Miguel Beruete ^{1,5,*} 

¹ Antennas Group-TERALAB, Universidad Pública de Navarra, Campus Arrosadía, 31006 Pamplona, Spain; irati.jauregui@unavarra.es (I.J.-L.); pablo.rodriguez@unavarra.es (P.R.-U.)

² Rzhanov Institute of Semiconductor Physics SB RAS, Novosibirsk Branch “TDIAM”, Lavrentiev Ave. 2/1, 630090 Novosibirsk, Russia; SAKuznetsov@nsm.nsu.ru

³ Novosibirsk State University, Pirogova St. 2, 630090 Novosibirsk, Russia

⁴ Institute of Automation and Electrometry SB RAS, Koptyug Ave. 1, 630090 Novosibirsk, Russia; nazar@iae.nsk.su

⁵ Institute of Smart Cities Campus Arrosadía, 31006 Pamplona, Spain

* Correspondence: miguel.beruete@unavarra.es; Tel.: +34-948-169-727

Received: 1 October 2018; Accepted: 6 November 2018; Published: 9 November 2018



Abstract: Subwavelength hole array (HA) metasurfaces support the so-called extraordinary optical transmission (EOT) resonance that has already been exploited for sensing. In this work, we demonstrate the superior performance of a different resonant regime of HA metasurfaces called anomalous EOT, by doing a thorough numerical and experimental study of its ability in thin-film label-free sensing applications in the terahertz (THz) band. A comprehensive analysis using both the regular and anomalous EOT resonances is done by depositing thin layers of dielectric analyte slabs of different thicknesses on the structures in different scenarios. We carry out a detailed comparison and demonstrate that the best sensing performance is achieved when the structure operates in the anomalous EOT resonance and the analyte is deposited on the non-patterned side of the metasurface, improving by a factor between 2 and 3 the results of the EOT resonance in any of the considered scenarios. This can be explained by the comparatively narrower linewidth of the anomalous EOT resonance. The results presented expand the reach of subwavelength HAs for sensing applications by considering the anomalous EOT regime that is usually overlooked in the literature.

Keywords: metasurface; sensing; thin film; terahertz; anomalous EOT

1. Introduction

The discovery of extraordinary optical transmission (EOT) through a subwavelength hole array (HA) by Ebbesen et al. [1] contributed decisively to relaunch the topic of plasmonics opening new avenues towards the use of apertures much smaller than the operation wavelength [2,3]. Although initially interpreted as the coupling of light to surface plasmons, it was soon noticed that similar peaks could be obtained even with perfect conductors [2–4]. This enabled the replica of the phenomenon at frequencies in which metals do not follow a Drude model (typical of the plasmonic approach), such as millimeter-waves [5]. Nowadays, EOT has been found all along the electromagnetic spectrum [2,3] giving rise to disruptive technological applications such as structural color pixels [6,7], metamaterial devices [8–10], etc. Interestingly, the high field intensity near the subwavelength apertures at the EOT resonance has been exploited for sensing applications [11–13] and nowadays one can find in the literature several examples of EOT biosensors [14], sensors combining nanofluidics and nanoplasmonics [15], and even sensing platforms for a direct detection and monitoring of viruses [16].

There are excellent reviews in the recent literature accounting for the latest progress in this exciting and expanding topic [17–20].

Sensing applications are also gaining momentum in the terahertz (THz) range. This portion of the electromagnetic spectrum goes from 0.1 to 10 THz and is far less developed than the infrared (or microwaves) due to the historical difficulties in generating and detecting radiation at these frequencies. However, a series of breakthrough discoveries made this band accessible, bridging effectively the “THz gap” [21]. Currently, THz spectroscopy and imaging are emerging fields that find applications in a variety of sectors such as security, defense, pharmaceuticals, etc. [22,23]. THz spectroscopy is considered to be promising for label-free sensing of substances because this radiation is sensitive to weak molecular interactions, it can deeply penetrate optically opaque materials of non-polar structure and is crucial to detect and identify biological samples, explosives, plastics, semiconductors, superconductors, while having a non-ionizing impact on matter due to a low energy of electromagnetic quanta [24,25]. Nevertheless, a major limitation is the relatively large wavelength that makes THz waves largely myopic when the amount of the substance under test is very small. Metasurfaces (of which EOT HAs are a particular example) are revolutionizing sensing all along the electromagnetic spectrum and especially at THz [24–26], because they produce a high electric field intensity near the metasurface, enhancing the light-matter interaction with the substance analyzed and producing a sharp change in the spectral response, usually a shift of the metasurface resonance. This allows for a reliable detection even with minute amounts of analyte, a feature that is optimal for label-free thin-film sensing analysis.

The first example of a thin-film sensor based on EOT HAs operating at THz was reported in [27]. In [28], a thorough study of the sensing performance of a fishnet structure composed of two stacked EOT HAs was evaluated. The sensing capability was assessed in terms of both the amplitude modulation and the frequency shift of the EOT resonance, showing that both strategies could be used for thin-film sensing. Typical EOT sensors consist of HAs with a square unit cell. Nevertheless, as we demonstrated in the past, a rectangular unit cell provides a richer response allowing for the excitation of two different EOT resonances depending on the polarization of the wave, called regular and anomalous EOT [29]. As demonstrated in that paper and analyzed in depth in [30,31], the anomalous EOT resonance is excited when the wave is polarized along the short hole periodicity and the HA is loaded with a dielectric slab with a minimum thickness and permittivity. On the other hand, the regular EOT is the classical EOT resonance that happens for a polarization parallel to the long HA periodicity and can exist even in absence of a dielectric slab. It is worth mentioning that the effect of adding a dielectric layer to an EOT HA had been studied in the past [32,33], but always considering the effect on the regular EOT resonance. Up to now, anomalous EOT has been exploited to develop compact THz polarizers even with dual band operation [34,35], and has been combined with an artificial wire medium for an accurate control of the resonance [36]. In that paper, its potential as a biosensor was pointed out, although it was not realized in practice. Despite the fact that other types of sharp spectral peaks such as Fano resonances have been extensively exploited for metamaterial sensing [37–39], these structures usually suffer from frequency shift saturation when the analyte rises a few dozens of micrometers. Interestingly, there is no theoretical saturation in the anomalous EOT resonance frequency. Hence, the only limitation is the attenuation of the peak due to material loss.

In this paper, we perform a thorough analysis of the sensing capability of several HAs loaded with dielectric slabs of different thicknesses, in such a way that some of the structures support the anomalous EOT resonance whereas others are in the limit or do not support it at all. We start the analysis by comparing the features of anomalous and regular EOT in idealized structures, based on purely numerical simulations. Then, we do a thorough analysis of the sensing performance by considering realistic structures in a variety of scenarios. To do this, we deposit thin layers of a dielectric analyte on the structures, and calculate both the sensitivity and the Figure of Merit (FOM, a finer parameter to assess the performance of sensing devices) of each structure. We conclude the study by comparing quantitatively the results obtained both for the regular and anomalous EOT resonance

regimes and demonstrate that the optimal operation occurs at the anomalous EOT resonance with deposition on the non-patterned side.

2. Materials and Methods

As shown in the unit cell representation of Figure 1a, the metasurfaces studied in this work consist of a periodic array of circular holes etched on an aluminum (Al) layer of thickness $t = 0.4 \mu\text{m}$ laying on polypropylene (PP) slabs of two different thicknesses $h_{PP} = 50$ and $75 \mu\text{m}$. The PP film from GoodFellow Company [40], whose permittivity is evaluated as $\epsilon_{PP} \approx 2.25 \times (1 - j10^{-3})$ [41,42], was intentionally chosen as a substrate material to minimize the dielectric losses of the metasurfaces. The relevant dimensions of the HA unit cell are $d_x = 115.5 \mu\text{m}$, $d_y = 350 \mu\text{m}$ and a hole diameter of $a = 105 \mu\text{m}$. In this study the excitation of the HA was done at normal incidence using two different linear polarization states: parallel to the large period of the structure (d_y), which corresponds to the regular EOT resonance excitation [5]; and parallel to the short period of the metasurface (d_x), which, under the appropriate conditions, gives rise to the anomalous EOT resonance [29–31].

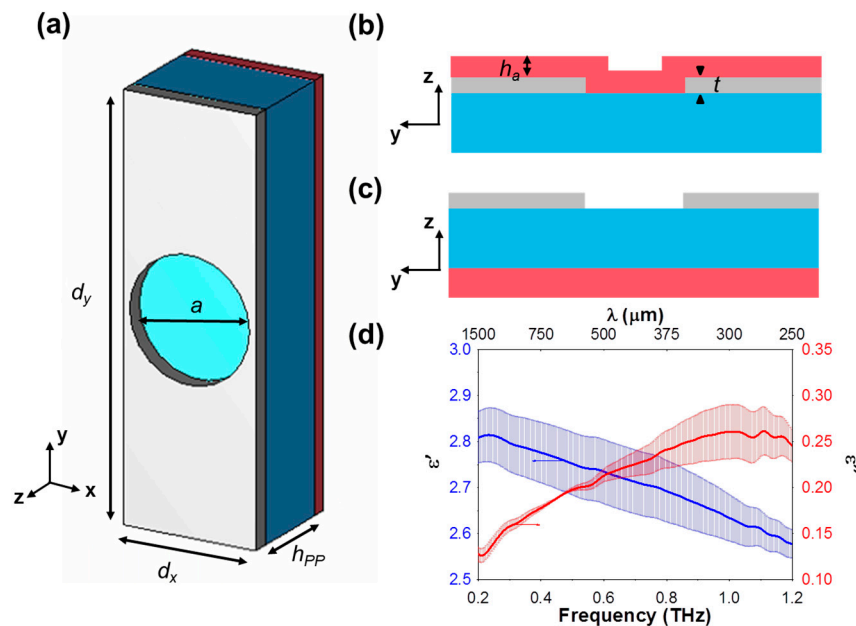


Figure 1. (a) Front view and (b,c) cross-section of the metasurface unit cell, showing the metallization (gray), PP substrate (blue) and analyte (red). Deposition of the analyte is done on the HA (b) and PP (c) faces. Dimensions: $d_x = 115.5 \mu\text{m}$, $d_y = 350 \mu\text{m}$, $a = 105 \mu\text{m}$, $h_{PP} = 50; 75 \mu\text{m}$, $t = 0.5 \mu\text{m}$, $h_a = 3; 7; 10; 13 \mu\text{m}$. (d) Measured frequency response of the complex analyte permittivity, with error bars: real (blue, left axis) and imaginary (red, right axis) components.

The sensing performance of the metasurfaces was evaluated by depositing a photoresist material (AR-P 3250 produced by ALLRESIST GmbH [43]) of variable thickness (from $3 \mu\text{m}$ to $13 \mu\text{m}$) on them, either on the PP or the HA side using a standard spin coating deposition technique. The photoresist complex permittivity, plotted in Figure 1d, was extracted experimentally from direct transmission measurements of a $100 \mu\text{m}$ thick liquid cell. In the initial study presented in the next section, a non-dispersive and lossless analyte with permittivity $\epsilon_a = 2.65$ was considered. This value was chosen as the mean value of the permittivity in the experimental frequency span.

All the design and numerical results in the paper were obtained using the commercial electromagnetic solver CST Microwave Studio®. To model the HA metasurface as an infinite array, the regime of Floquet ports and unit cell boundary conditions applied to the designed unit cell was employed. The Al-layer was modeled as a non-dispersive medium with conductivity $\sigma = 1.5 \times 10^7 \text{ S/m}$ whose value, according to our earlier study [42], was found to be reduced versus

the nominal conductivity of bulky Al due to inherent surface roughness and granularities of PP films [41]. After the design stage, the structures were fabricated via a standard contact photolithography technique [41,44,45] which was specifically adapted to flexible PP-film substrates, whose industrial production does not allow obtaining a liquid material suitable for posterior film deposition via spin coating. Al-metallization was sputtered onto the PP films by using a vacuum thermal deposition method. Prior to sputtering, the PP substrates were treated with a glow discharge in O₂ atmosphere to improve adhesion of Al to PP.

The experimental characterization of the designed HA metasurfaces was done on a custom-made terahertz time-domain spectrometer (THz-TDS) developed in the Laboratory of Information Optics at the Institute of Automation and Electrometry SB RAS (Novosibirsk, Russia). This instrument utilizes a conventional TDS scheme based on a mode-locked Er-fiber laser with a second harmonic generation module ($\lambda = 775$ nm, $\tau = 130$ fs, $P = 100$ mW) and a multi-slit photoconductive antenna iPCA-21-05-1000-800-h (Batop GmbH, Germany) used as an emitter of THz waves, which are further detected via electro-optic sampling [46]. The spectrometer enables the complex transmission measurements within the spectral range of 0.1–2.5 THz with a spectral resolution of 10 GHz and a dynamic range of more than 60 dB (@ 0.85 THz).

3. Results and Discussion

Before characterizing the sensing performance of the fabricated HA metasurfaces, we begin the study by analyzing the response of an ideal lossless structure. Thus, we model the metallic parts as perfect electric conductors with zero thickness and all dielectric materials are described only by a non-dispersive real permittivity with values $\epsilon_{PP} = 2.25$ and $\epsilon_a = 2.65$. We consider both vertical and horizontal polarizations in order to excite regular and anomalous EOT, respectively, and ascertain which of the two options offers the best results for sensing purposes. As discussed in [30,31] the appearance of the anomalous EOT depends on the dielectric slab characteristics (h_{PP} and ϵ_{PP}) as well as the large HA periodicity, d_y . More specifically, the anomalous EOT resonance cutoff can be calculated with the auxiliary factor $F = h_{PP}\sqrt{(\epsilon_{PP} - 1)}/d_y$, so that if $F \geq 0.25$, the anomalous EOT peak will appear. In this initial study we fix the thickness of the PP substrate at $h_{PP} = 78.25$ μm so that $F = 0.25$ and hence the anomalous EOT is exactly at cutoff. On the other hand, the regular EOT resonance exists even in absence of a dielectric substrate, so for this study a free-standing structure without PP substrate is considered.

As shown in Figure 2a,b (black line) in absence of analyte, the regular EOT resonance takes place at 0.81 THz, whereas the anomalous EOT resonance occurs at 0.84 THz. To evaluate the performance of each resonance in label-free thin-film sensing applications, a dielectric slab acting as an analyte with permittivity $\epsilon_a = 2.65$ and thickness ranging from $h_a = 3$ μm ($8.5 \times 10^{-3} \lambda_0$, where $\lambda_0 \sim 0.35$ mm) to 15 μm ($42.9 \times 10^{-3} \lambda_0$) with a step of 3 μm is added on top. In the anomalous EOT study, the analyte is put on the external face of the PP substrate, whereas, obviously, in the regular EOT case (free-standing) the analyte touches the holey metal. As the analyte thickness increases, the transmission peak redshifts for both resonances, see Figure 2. To have a quantitative assessment of the behavior, the wavelength shift is plotted as a function of h_a in panels (c) and (d). Comparing both plots, it is clear that the shift is stronger for the regular resonance, suggesting at first sight that this regime is more appropriate for sensing purposes. Nevertheless, to clarify this aspect we must carry out a formal evaluation of the performance in terms of the sensitivity (S) and Figure of Merit (FOM), represented in Figure 2e,f. The sensitivity is defined as the ratio between the variation of the resonance wavelength and the analyte thickness, $S = \Delta\lambda/h_a$. With this definition, the average sensitivity is equal to the slope of the regression lines in Figure 2c,d. However, in many cases this value alone is not enough to determine the quality of a sensor. That is why the more refined FOM parameter is usually preferred. The FOM relates the sensitivity and the full width at half minimum (FWHM) in wavelength dimensions, $\text{FOM} = S/\text{FWHM}$, and has units of mm^{-1} . A sensor with high quality factor would present a narrow spectral line and is able to achieve a relatively high FOM.

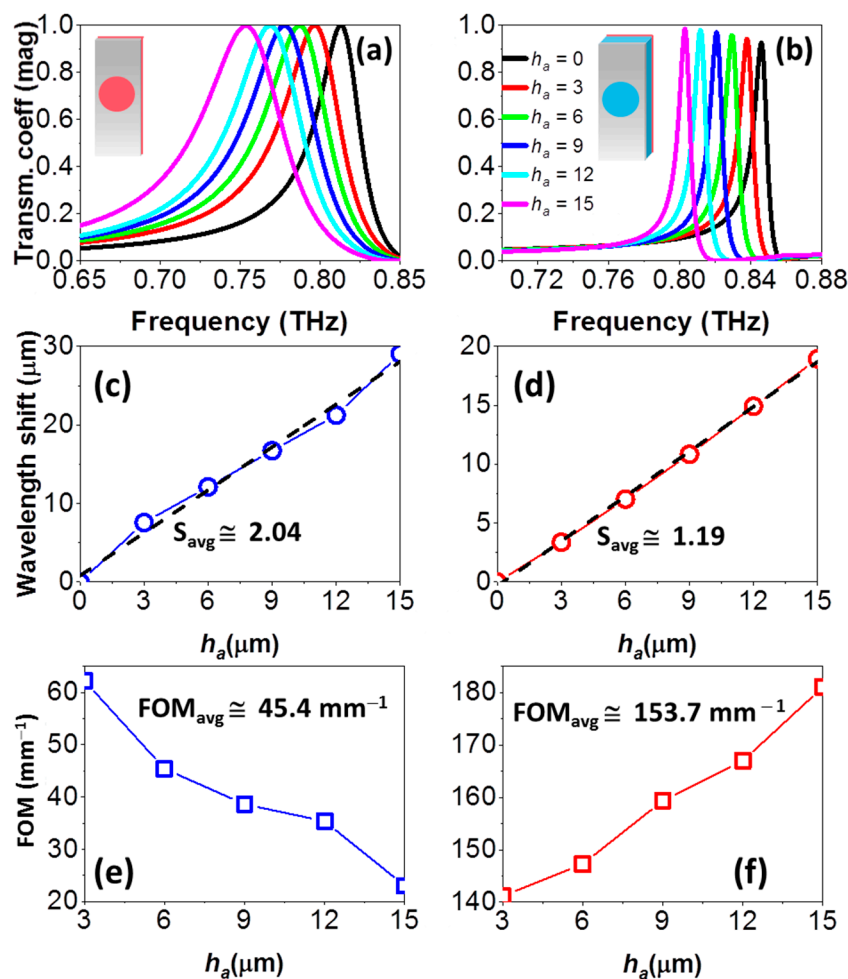


Figure 2. Transmission coefficient for the regular EOT (a) and anomalous EOT (b) resonance of an ideal lossless HA and several analyte thicknesses (in μm). (c) Wavelength shift as a function of the analyte thickness for extremely thin analytes, for the regular EOT resonance, calculated as $\Delta\lambda = \lambda_a - \lambda_0$, with λ_a the resonance wavelength at each h_a and λ_0 the resonance wavelength without the analyte. (d) Idem for the anomalous EOT. FOM as a function of the analyte thickness, for the regular (e) and anomalous EOT (f) resonance. Labels S_{avg} in (c), (d) and FOM_{avg} in (e), (f) refer to average values of S and FOM, respectively.

With these definitions, we find that the regular EOT configuration is slightly better than the anomalous EOT in terms of average sensitivity: 2.04 vs. 1.19. However, the FOM shows that the anomalous EOT is clearly superior to the regular EOT resonance, with an average value of 153.7 mm^{-1} . This is much higher than the value of 45.4 mm^{-1} calculated for the latter and is due to the comparatively narrower FWHM of the anomalous EOT resonance. With these results, it can be affirmed that the anomalous EOT presents a better behavior for sensing purposes than the regular EOT, improving the FOM by a factor of more than 3.

After this initial study, we concentrate now on the analysis of the designed and fabricated HA metasurfaces. As our aim here is to evaluate in depth the performance of the anomalous EOT resonance for sensing applications, two different substrate thicknesses are used $h_{PP} = 75 \mu\text{m}$ (Figure 3) and $h_{PP} = 50 \mu\text{m}$ (Figure 4), that correspond to $F = 0.24$ and 0.16, respectively. The first case is chosen to have the anomalous resonance very near cutoff, so that a slight change provoked by an analyte can give rise to a strong spectral variation. Conversely, in the second case the anomalous EOT resonance is deeply in cutoff and we do not expect a sharp response, at least with thin analytes. The sensing performance of the structures is evaluated by depositing four different analyte thicknesses: $h_a = 3 \mu\text{m}$

($8.5 \times 10^{-3} \lambda_0$); $7 \mu\text{m}$ ($19.8 \times 10^{-3} \lambda_0$); $10 \mu\text{m}$ ($28.3 \times 10^{-3} \lambda_0$); and $13 \mu\text{m}$ ($36.8 \times 10^{-3} \lambda_0$). Numerical results are shown in the upper panels (a), (b), (e), (f); and experimental measurements on the lower panels (c), (d), (g), (h) of Figures 3 and 4. To have a complete picture of the performance, two different scenarios were considered: when the analyte is deposited on the HA side and on the PP side, schematically depicted in Figure 1b,c.

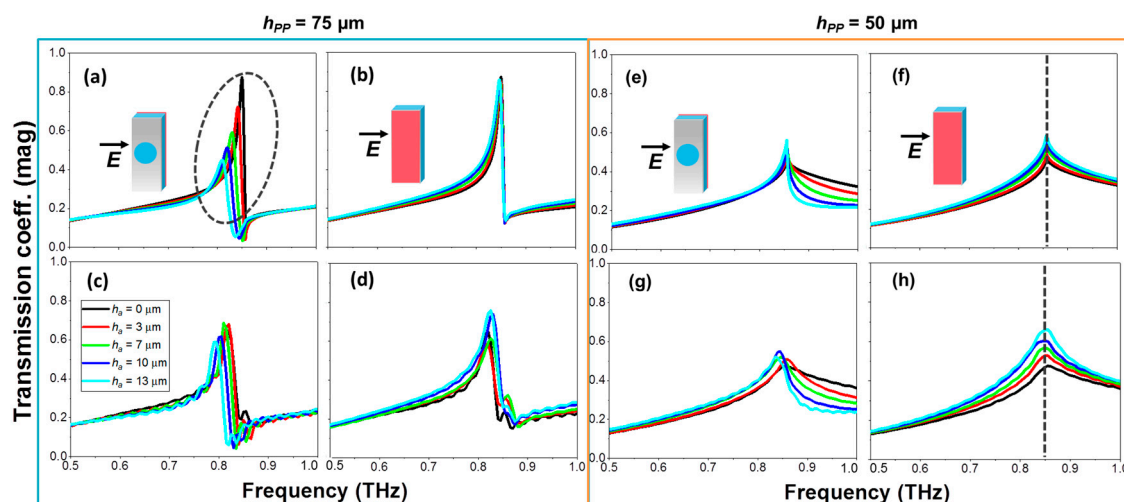


Figure 3. Transmission coefficient magnitude at the anomalous EOT regime in HA metasurfaces with $h_{pp} = 75 \mu\text{m}$ (a–d) and $h_{pp} = 50 \mu\text{m}$ (e–f) μm under normal incidence and different analyte thicknesses: $h_a = 0 \mu\text{m}$ (black); $h_a = 3 \mu\text{m}$ (red); $7 \mu\text{m}$ (green); $10 \mu\text{m}$ (dark blue); $13 \mu\text{m}$ (cyan) for the anomalous EOT. Simulated (top) and measured (bottom) results. The dashed ellipse in panel (a) highlights the region where sensing based on frequency shift is feasible. The dashed grey lines in panels (f,h) highlights the resonance frequency (0.85 THz) where the amplitude sensitivity analysis can be done. Insets in panels (a,b,e,f) depict schematically each scenario, following the colour convention of Figure 1.

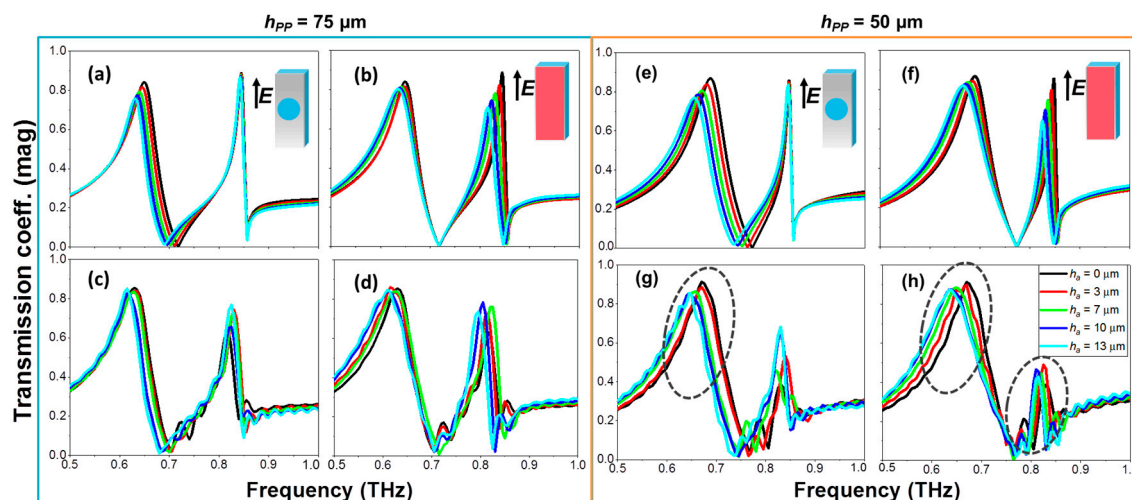


Figure 4. Transmission coefficient magnitude at the regular EOT regime in HA metasurfaces with $h_{pp} = 75 \mu\text{m}$ (a–d) and $h_{pp} = 50 \mu\text{m}$ (e–f) μm under normal incidence and different analyte thicknesses: $h_a = 0 \mu\text{m}$ (black); $h_a = 3 \mu\text{m}$ (red); $7 \mu\text{m}$ (green); $10 \mu\text{m}$ (dark blue); $13 \mu\text{m}$ (cyan) for the anomalous EOT. Simulated (top) and measured (bottom) results. The dashed ellipse in panels (f,g) highlights the regions where sensing is feasible. Insets in panels (a,b,e,f) depict schematically each scenario, following the colour convention of Figure 1.

Focusing first on the horizontal polarization (anomalous EOT), we find that the transmission coefficient without analyte ($h_a = 0$) shows in all considered cases clear resonant features at ~ 0.85 THz,

with very good concordance between simulation and measurement, see black curves in Figure 3. Although in the case of the 75 μm thick PP film (Figure 3a–d) the anomalous EOT resonance is slightly below cutoff, it is close enough so that it gives rise to a high transmission peak followed by a minimum in the spectrum. This is in contrast with the behavior of the 50 μm thick PP film (Figure 3e–h) that shows only a local maximum (a “kink”) with reduced amplitude (~ 0.5), as expected [29–31]. Now, the sensing performance of each configuration is analyzed by increasing the analyte thickness. It can be seen that the best scenario for sensing purposes is the one in which the analyte is deposited on the PP side of the $h_{\text{PP}} = 75 \mu\text{m}$ thick metasurface (Figure 3a,c), with an average sensitivity of ~ 0.8 (~ 1.24) and an average FOM of $\sim 28.6 \text{ mm}^{-1}$ ($\sim 46 \text{ mm}^{-1}$) in the experimental (numerical) results. This is in agreement with our analysis above, since depositing on the PP side is equivalent to increasing the substrate thickness (as a side comment, note that the peak amplitude decreases as h_a increases due to the growing ohmic loss because, unlike the previous study, we are considering here a lossy and dispersive analyte. Note also that this effect is more evident in the simulation than in the experimental results, probably because in the experiment the characteristics of the analyte might differ between successive depositions and, in addition, it is rather difficult to have a proper characterization of metal and dielectric losses). When the analyte is deposited on the HA side (Figure 3b,d) the frequency shift of the anomalous EOT resonance is negligible, rendering this configuration ineffective for sensing purposes. As explained in our previous paper [31], two different anomalous EOT peaks can be excited independently by placing dielectric slabs on both sides of the holey metal. In the configuration considered here, the analyte slab is too thin and hence unable to excite its own anomalous EOT resonance (i.e., $F \ll 0.25$ in that side). This is why in the spectral response we only see the peak corresponding to the PP slab, which is largely insensitive to the analyte deposition on the other face.

For the 50 μm PP thick structure with the analyte deposited on the PP side we find that the “kink” becomes narrower and its amplitude grows faintly as h_a is enlarged, see Figure 3e,g. This is because we are approaching gradually towards, but never reaching cutoff, even with the largest analyte thickness. In practice, this means that it might be feasible to perform sensing by looking at the peak amplitude variation. At least in simulation (Figure 3e) this looks viable, but it seems hardly attainable experimentally (Figure 3g), probably due to fabrication tolerances, and to the fact that high Q resonances are greatly affected by losses. When the analyte is placed on the HA side (Figure 3f,h) we notice a negligible frequency shift but, interestingly, a clear amplitude increment of the “kink”. This enhancement in the transmission coefficient is associated with a better impedance matching of the structure. From the specialized literature [47], it is known that the optimal operation of frequency selective surfaces and spatial filters is achieved when both faces of the metallic film are coated with dielectric slabs of identical characteristics. In our case, increasing the analyte thickness leads to a better matching of the impedance seen at both interfaces, giving as a result a higher peak amplitude. In this way, it is possible to define a new sensitivity, referred to as Amplitude Sensitivity (AS) and calculated as the ratio between the variation of the amplitude at the resonant frequency and the variation of the analyte thickness: $AS = \Delta A/h_a$. With this definition, we experimentally obtain $AS = 0.02 \mu\text{m}^{-1}$. Note that in this case it is impossible to define a FOM, due to the inexistence of a valid FWHM. If we define the amplitude sensitivity as done in [28], $AS_{\%} = \Delta A(\%)/h_a$, we achieve a maximum experimental value for the case of $h_a = 3.2 \mu\text{m}$ of $35\%/\mu\text{m}$. Although this value is much lower than the $66\%/\mu\text{m}$ reported in [28], note that in our case it is only needed to tune the spectrum at a single frequency. In addition, our amplitude modulation is done “positively”, and does not experience vanishing of the signal as the analyte increases. Indeed, our device exhibits an amplitude rise as we add the analyte material, because when the analyte thickness is increased, the F factor gets closer to the limit condition in which the anomalous peak appears. Obviously, a saturation of the response will arise when we get the condition $F = 0.25$.

We consider next vertical polarization (regular EOT) just for comparison purposes; see all results in Figure 4. In this case, the response is very similar regardless the PP thickness, as this parameter is not critical for the performance (in contrast to anomalous EOT). Therefore, we will study both cases,

$h_{pp} = 50$ and $75 \mu\text{m}$, in parallel. The first difference we observe in the spectral response in comparison with the previous study is that there are two resonance peaks, at 690 and 847 GHz. Each peak is related to the EOT resonance principally at the PP and air interfaces [48]. Therefore, depositing the analyte on the PP side mainly shifts the lower frequency peak whereas depositing on the air side mainly affects the higher frequency one. Although in the simulation both peaks can be potentially employed for sensing purposes, in the measurement only the lower frequency resonance presents a noticeable redshift. Furthermore, the structure with $h_{pp} = 50 \mu\text{m}$ has a better performance in practice, probably due to the thinner substrate, which is further from the saturation point of the maximally achievable frequency shift. Consequently, we only select the cases highlighted with a dotted ellipse for the calculation of the sensitivity and FOM as these are the ones in which we can appreciate a frequency shift large enough to use the structure as a sensing device, and we have a good agreement between the simulated and measured results. Note that in the case of the second resonance when depositing on the HA side, the FOM cannot be calculated due to a low magnitude of the peak.

To ease the comparison all the values of the cases of interest extracted from the experimental measurements are collected in Table 1. As shown there, although the sensitivity in the anomalous EOT case is below the regular EOT case, the FOM is higher, corroborating our initial study.

Table 1. Average sensitivity and FOM achieved in the configurations shown in Figures 3 and 4, experimental results.

Resonance	h_{pp} (μm)	Analyte Side	S	FOM (mm^{-1})
Anomalous	75	PP	0.8	28.6
		HA	—	—
	50	PP	—	—
		HA	$0.02 \mu\text{m}^{-1} *$	—
Regular	75	PP	—	—
		HA	—	—
	50	PP	1.2	12.9
		HA	$1.85/0.68 **$	$16.6/- **$

* Note that in these cases we are referring to the amplitude sensitivity, $AS = \Delta A/h_a$. ** The first/second number refers to the first/second resonance

As a final study, we compare our structure with others found in the literature that also exploit sharp peaks in transmission, such as Fano resonances. For this comparison, we use the sensitivity as defined before, $S = \Delta\lambda/h_a$. In [37], a dual flexible THz asymmetric split ring resonator (TASR) was used to detect a thin film of 100 nm with refractive index $n = 4$, by coating both sides of the structure, and achieved an experimental sensitivity of 67 and 85 for the analyte deposited in the non-patterned and patterned side, respectively. In [38], a toroidal TASR was designed with a sensitivity of 3.74 for a $13.8 \mu\text{m}$ thick analyte with $n = 1.6$. Finally, a TASR based on a Fano resonance operating at 0.52 THz was designed in [39]. The sensitivity achieved for a $1 \mu\text{m}$ thick analyte of $n = 1.6$ was 11.3. As seen in this comparison, our designs present lower sensitivity values. Nevertheless, the sharp peak of the EOT resonance leads to higher values of FOM. Moreover, the use of the EOT resonance instead of Fano resonances brings the advantage of not having any theoretical limit in the achievable frequency shift.

4. Conclusions

To sum up, we have demonstrated the superior performance of a HA metasurface when it operates at the anomalous EOT resonance, exceeding largely the results obtained at the regular EOT in label-free thin-film sensing applications. Although the frequency shift and hence the sensitivity of the anomalous EOT resonance are smaller than those of the regular EOT resonance, its comparatively narrower FWHM leads to an increment of the FOM. In our initial study considering idealized structures we have achieved an average FOM of 153.7mm^{-1} , which improves the results obtained with the regular EOT by a factor of more than 3. Two HA metasurfaces of different PP thicknesses have been fabricated

and measured to analyze the effects on the sensing quality parameters depending on the side on which the analyte under measurement is deposited. We have demonstrated that, for sufficiently thick substrates, sensing in the anomalous EOT resonance and depositing on the non-patterned side of the metasurface is a much better option with lower sensitivities but higher FOMs, with an improvement of a factor between 2 and 3 as compared to the best case of the regular EOT resonance. Using the optimal configuration provides a benefit that in routine operation the structure can be cleaned without damaging the metallic pattern. Additionally, we have found an alternative for thin-film sensing based on a variation of a peak amplitude. This can be used when the substrate thickness is too thin to exhibit the anomalous EOT resonance and takes place when the analyte is deposited on the patterned side of the metasurface. The obtained results demonstrate the excellent performance of the anomalous EOT resonance in practical thin-film sensing platforms.

Author Contributions: conceptualization, M.B.; methodology, I.J.-L., P.R.-U., S.A.K., N.A.N. and M.B.; software, I.J.-L. and P.R.-U.; validation, S.A.K. and N.A.N.; formal analysis, I.J.-L. and P.R.-U.; investigation, S.A.K. and N.A.N.; resources, S.A.K.; writing—original draft preparation, I.J.-L., and M.B.; writing—review and editing, I.J.-L., P.R.-U., S.A.K., N.A.N. and M.B.; visualization, I.J.-L., P.R.-U., S.A.K. and M.B.; supervision, S.A.K. and M.B.; project administration, S.A.K. and M.B.; funding acquisition, S.A.K., N.A.N. and M.B.

Funding: This research was funded by the Spanish Ministerio de Economía y Competitividad with European Union Fondo Europeo de Desarrollo Regional (FEDER) funds, grant number TEC2014-51902-C2-2-R. The work was partially supported by the Russian Foundation for Basic Research (Project No. 17-32-80039, experimental study; Project No. 18-29-20066, technological implementation). The authors gratefully acknowledge the Shared Equipment Center “Spectroscopy and Optics” of the Institute of Automation and Electrometry SB RAS for the provided instrumental support of THz measurements and the Rzhanov Institute of Semiconductor Physics SB RAS for the provided technological support (State Assignment Program, Project No. 0306-2016-0020).

Conflicts of Interest: The authors declare no conflict of interest. The funders had no role in the design of the study; in the collection, analyses, or interpretation of data; in the writing of the manuscript, or in the decision to publish the results.

References

1. Ebbesen, T.W.; Lezec, H.J.; Ghaemi, H.F.; Thio, T.; Wolff, P.A. Extraordinary optical transmission through sub-wavelength hole arrays. *Nature* **1998**, *391*, 667–669. [[CrossRef](#)]
2. Garcia-Vidal, F.J.; Martín-Moreno, L.; Ebbesen, T.W.; Kuipers, L. Light passing through subwavelength apertures. *Rev. Mod. Phys.* **2010**, *82*, 729–787. [[CrossRef](#)]
3. García de Abajo, F.J. Colloquium: Light scattering by particle and hole arrays. *Rev. Mod. Phys.* **2007**, *79*, 1267–1290. [[CrossRef](#)]
4. Martín-Moreno, L.; García-Vidal, F.J.; Lezec, H.J.; Pellerin, K.M.; Thio, T.; Pendry, J.B.; Ebbesen, T.W. Theory of Extraordinary Optical Transmission through Subwavelength Hole Arrays. *Phys. Rev. Lett.* **2001**, *86*, 1114–1117. [[CrossRef](#)] [[PubMed](#)]
5. Beruete, M.; Sorolla, M.; Campillo, I.; Dolado, J.S.; Martín-Moreno, L.; Bravo-Abad, J.; García-Vidal, F.J. Enhanced millimeter-wave transmission through subwavelength hole arrays. *Opt. Lett.* **2004**, *29*, 2500–2502. [[CrossRef](#)] [[PubMed](#)]
6. Xu, T.; Shi, H.; Wu, Y.K.; Kaplan, A.F.; Ok, J.G.; Guo, L.J. Structural colors: From plasmonic to carbon nanostructures. *Small* **2011**, *7*, 3128–3136. [[CrossRef](#)] [[PubMed](#)]
7. Zhao, Y.; Zhao, Y.; Hu, S.; Lv, J.; Ying, Y.; Gervinskas, G.; Si, G. Artificial Structural Color Pixels: A Review. *Materials (Basel)* **2017**, *10*, 944. [[CrossRef](#)] [[PubMed](#)]
8. Beruete, M.; Sorolla, M.; Campillo, I. Left-handed extraordinary optical transmission through a photonic crystal of subwavelength hole arrays. *Opt. Express* **2006**, *14*, 5445–5455. [[CrossRef](#)] [[PubMed](#)]
9. Navarro-Cía, M.; Beruete, M.; Sorolla, M.; Campillo, I. Negative refraction in a prism made of stacked subwavelength hole arrays. *Opt. Express* **2008**, *16*, 560–566. [[CrossRef](#)] [[PubMed](#)]
10. Valentine, J.; Zhang, S.; Zentgraf, T.; Ulin-Avila, E.; Genov, D.A.; Bartal, G.; Zhang, X. Three-dimensional optical metamaterial with a negative refractive index. *Nature* **2008**, *455*, 376–379. [[CrossRef](#)] [[PubMed](#)]
11. Brolo, A.G.; Gordon, R.; Leathem, B.; Kavanagh, K.L. Surface plasmon sensor based on the enhanced light transmission through arrays of nanoholes in gold films. *Langmuir* **2004**, *20*, 4813–4815. [[CrossRef](#)] [[PubMed](#)]

12. Gordon, R.; Sinton, D.; Kavanagh, K.L.; Brolo, A.G. A New Generation of Sensors Based on Extraordinary Optical Transmission. *Acc. Chem. Res.* **2008**, *41*, 1049–1057. [[CrossRef](#)] [[PubMed](#)]
13. Gordon, R.; Brolo, A.G.; Sinton, D.; Kavanagh, K.L. Resonant optical transmission through hole-arrays in metal films: Physics and applications. *Laser Photonics Rev.* **2010**, *4*, 311–335. [[CrossRef](#)]
14. Ding, T.; Hong, M.; Richards, A.M.; Wong, T.I.; Zhou, X.; Drum, C.L. Quantification of a Cardiac Biomarker in Human Serum Using Extraordinary Optical Transmission (EOT). *PLoS ONE* **2015**, *10*, e0120974. [[CrossRef](#)] [[PubMed](#)]
15. Eftekhari, F.; Escobedo, C.; Ferreira, J.; Duan, X.; Giroto, E.M.; Brolo, A.G.; Gordon, R.; Sinton, D. Nanoholes As Nanochannels: Flow-through Plasmonic Sensing. *Anal. Chem.* **2009**, *81*, 4308–4311. [[CrossRef](#)] [[PubMed](#)]
16. Yanik, A.A.; Huang, M.; Kamohara, O.; Artar, A.; Geisbert, T.W.; Connor, J.H.; Altug, H. An optofluidic nanoplasmonic biosensor for direct detection of live viruses from biological media. *Nano Lett.* **2010**, *10*, 4962–4969. [[CrossRef](#)] [[PubMed](#)]
17. Chen, J.; Gan, F.; Wang, Y.; Li, G. Plasmonic Sensing and Modulation Based on Fano Resonances. *Adv. Opt. Mater.* **2018**, *6*, 1–21. [[CrossRef](#)]
18. Blanchard-Dionne, A.-P.; Meunier, M. Sensing with periodic nanohole arrays. *Adv. Opt. Photonics* **2017**, *9*, 891. [[CrossRef](#)]
19. Chorsi, H.T.; Zhu, Y.; Zhang, J.X.J. Patterned Plasmonic Surfaces—Theory, Fabrication, and Applications in Biosensing. *J. Microelectromech. Syst.* **2017**, *26*, 718–739. [[CrossRef](#)] [[PubMed](#)]
20. Escobedo, C. On-chip nanohole array based sensing: A review. *Lab Chip* **2013**, *13*, 2445–2463. [[CrossRef](#)] [[PubMed](#)]
21. Siegel, P.H. Terahertz technology. *IEEE Trans. Microw. Theory Tech.* **2002**, *50*, 910–928. [[CrossRef](#)]
22. Tonouchi, M. Cutting-edge terahertz technology. *Nat. Photonics* **2007**, *1*, 97–105. [[CrossRef](#)]
23. Dhillon, S.S.; Vitiello, M.S.; Linfield, E.H.; Davies, A.G.; Hoffmann, M.C.; Booske, J.; Paoloni, C.; Gensch, M.; Weightman, P.; Williams, G.P.; et al. The 2017 terahertz science and technology roadmap. *J. Phys. D Appl. Phys.* **2017**, *50*, 043001. [[CrossRef](#)]
24. O’Hara, J.F.; Withayachumnankul, W.; Al-Naib, I. A Review on Thin-film Sensing with Terahertz Waves. *J. Infrared Millim. Terahertz Waves* **2012**, *33*, 245–291. [[CrossRef](#)]
25. Rodríguez-Ulibarri, P.; Beruete, M. Sensing at Terahertz Frequencies. In *Fiber Optic Sensors (Smart Sensors, Measurement and Instrumentation vol 21)*; Matías, I.R., Ikezawa, S., Corres, J., Eds.; Springer International Publishing: Cham, Switzerland, 2017; Volume 21, pp. 301–327.
26. Xu, W.; Xie, L.; Ying, Y. Mechanisms and applications of terahertz metamaterial sensing: A review. *Nanoscale* **2017**, *9*, 13864–13878. [[CrossRef](#)] [[PubMed](#)]
27. Miyamaru, F.; Hayashi, S.; Otani, C.; Kawase, K.; Ogawa, Y.; Yoshida, H.; Kato, E. Terahertz surface-wave resonant sensor with a metal hole array. *Opt. Lett.* **2006**, *31*, 1118. [[CrossRef](#)] [[PubMed](#)]
28. Yahiaoui, R.; Strikwerda, A.C.; Jepsen, P.U. Terahertz plasmonic structure with enhanced sensing capabilities. *IEEE Sens. J.* **2016**, *16*, 2484–2488. [[CrossRef](#)]
29. Kuznetsov, S.A.; Navarro-Cía, M.; Kubarev, V.V.; Gelfand, A.V.; Beruete, M.; Campillo, I.; Sorolla, M. Regular and anomalous extraordinary optical transmission at the THz-gap. *Opt. Express* **2009**, *17*, 11730. [[CrossRef](#)] [[PubMed](#)]
30. Beruete, M.; Navarro-Cía, M.; Kuznetsov, S.A.; Sorolla, M. Circuit approach to the minimal configuration of terahertz anomalous extraordinary transmission. *Appl. Phys. Lett.* **2011**, *98*, 014106. [[CrossRef](#)]
31. Beruete, M.; Navarro-Cia, M.; Sorolla Ayza, M. Understanding Anomalous Extraordinary Transmission From Equivalent Circuit and Grounded Slab Concepts. *IEEE Trans. Microw. Theory Tech.* **2011**, *59*, 2180–2188. [[CrossRef](#)]
32. Miyamaru, F.; Sasagawa, Y.; Takeda, M.W. Effect of dielectric thin films on reflection properties of metal hole arrays. *Appl. Phys. Lett.* **2010**, *96*, 021106. [[CrossRef](#)]
33. Han, J.; Lu, X.; Zhang, W. Terahertz transmission in subwavelength holes of asymmetric metal-dielectric interfaces: The effect of a dielectric layer. *J. Appl. Phys.* **2008**, *103*, 033108. [[CrossRef](#)]
34. Navarro-Cía, M.; Rodríguez-Ulibarri, P.; Torres, V.; Beruete, M. Quarter-Wave Plate Based on Dielectric-Enabled Extraordinary Resonant Transmission. *IEEE Photonics Technol. Lett.* **2012**, *24*, 945–947. [[CrossRef](#)]
35. Torres, V.; Sanchez, N.; Etayo, D.; Ortuno, R.; Navarro-Cia, M.; Martinez, A.; Beruete, M. Compact Dual-Band Terahertz Quarter-Wave Plate Metasurface. *IEEE Photonics Technol. Lett.* **2014**, *26*, 1679–1682. [[CrossRef](#)]

36. Navarro-Cía, M.; Rodríguez-Ulibarri, P.; Beruete, M. Hedgehog subwavelength hole arrays: control over the THz enhanced transmission. *New J. Phys.* **2013**, *15*, 013003. [[CrossRef](#)]
37. Srivastava, Y.K.; Cong, L.; Singh, R. Dual-surface flexible THz Fano metasensor. *Appl. Phys. Lett.* **2017**, *111*, 1–6. [[CrossRef](#)]
38. Gupta, M.; Srivastava, Y.K.; Manjappa, M.; Singh, R. Sensing with toroidal metamaterial. *Appl. Phys. Lett.* **2017**, *110*, 121108. [[CrossRef](#)]
39. Singh, R.; Cao, W.; Al-Naib, I.; Cong, L.; Withayachumnankul, W.; Zhang, W. Ultrasensitive THz sensing with high-Q Fano resonances in metasurfaces. *Appl. Phys. Lett.* **2014**, *171101*, 5. [[CrossRef](#)]
40. Goodfellow Cambridge Ltd. Available online: <http://www.goodfellow.com> (accessed on 6 November 2018).
41. Navarro-Cía, M.; Kuznetsov, S.A.; Aznabet, M.; Beruete, M.; Falcone, F.; Sorolla, M. Route for Bulk Millimeter Wave and Terahertz Metamaterial Design. *IEEE J. Quantum Electron.* **2011**, *47*, 375–385. [[CrossRef](#)]
42. Kuznetsov, S.A.; Paulish, A.G.; Navarro-Cía, M.; Arzhannikov, A.V. Selective Pyroelectric Detection of Millimetre Waves Using Ultra-Thin Metasurface Absorbers. *Sci. Rep.* **2016**, *6*, 21079. [[CrossRef](#)] [[PubMed](#)]
43. ALLRESIST GmbH. Available online: <https://www.allresist.com> (accessed on 6 November 2018).
44. Aznabet, M.; Navarro-Cía, M.; Kuznetsov, S.A.; Gelfand, A.V.; Fedorinina, N.I.; Goncharov, Y.G.; Beruete, M.; El Mrabet, O.; Sorolla, M. Polypropylene-substrate-based SRR- And CSRR-metasurfaces for submillimeter waves. *Opt. Express* **2008**, *16*, 18312–18319. [[CrossRef](#)] [[PubMed](#)]
45. Kuznetsov, S.A.; Arzhannikov, A.V.; Kubarev, V.V.; Kalinin, P.V.; Sorolla, M.; Navarro-Cía, M.; Aznabet, M.; Beruete, M.; Falcone, F.; Goncharov, Y.G.; et al. Development and Characterization of Quasi-Optical Mesh Filters and Metastructures for Subterahertz and Terahertz Applications. *Key Eng. Mater.* **2010**, *437*, 276–280. [[CrossRef](#)]
46. Antsygin, V.D.; Mamrashev, A.A.; Nikolaev, N.A.; Potaturkin, O.I.; Bekker, T.B.; Solntsev, V.P. Optical properties of borate crystals in terahertz region. *Opt. Commun.* **2013**, *309*, 333–337. [[CrossRef](#)]
47. Munk, B.A. *Frequency Selective Surfaces: Theory and Design*; Wiley-Interscience: Hoboken, NJ, USA, 2000; ISBN 0471370479.
48. Lomakin, V.; Michielssen, E. Enhanced transmission through metallic plates perforated by arrays of subwavelength holes and sandwiched between dielectric slabs. *Phys. Rev. B* **2005**, *71*, 235117. [[CrossRef](#)]



© 2018 by the authors. Licensee MDPI, Basel, Switzerland. This article is an open access article distributed under the terms and conditions of the Creative Commons Attribution (CC BY) license (<http://creativecommons.org/licenses/by/4.0/>).

Chapter V: MIR spectroscopy for food quality determination

Up to this point, we have focused our research on the THz regime. In this part of the thesis, we now move into the MIR regime, and explore another type of sensing based on MIR spectroscopy. Here the basis of this technique is explained, and our contribution, based on the detection of oxidation parameters in animal meat, presented.

5.1. Fundamentals of Infrared spectroscopy

Spectroscopy is based on the study of electromagnetic radiation interaction with matter. The nature of this interaction will depend on the energy of the radiation itself, but also on the properties of matter. Thus, depending on the region of the EM spectrum different types of interactions can be found: ionizing (Gamma and X-rays), chemical-electronic (Ultraviolet-Visible), vibrational and rotational (IR), or magnetic (microwave and lower rays), as shown in Fig. 5.1.

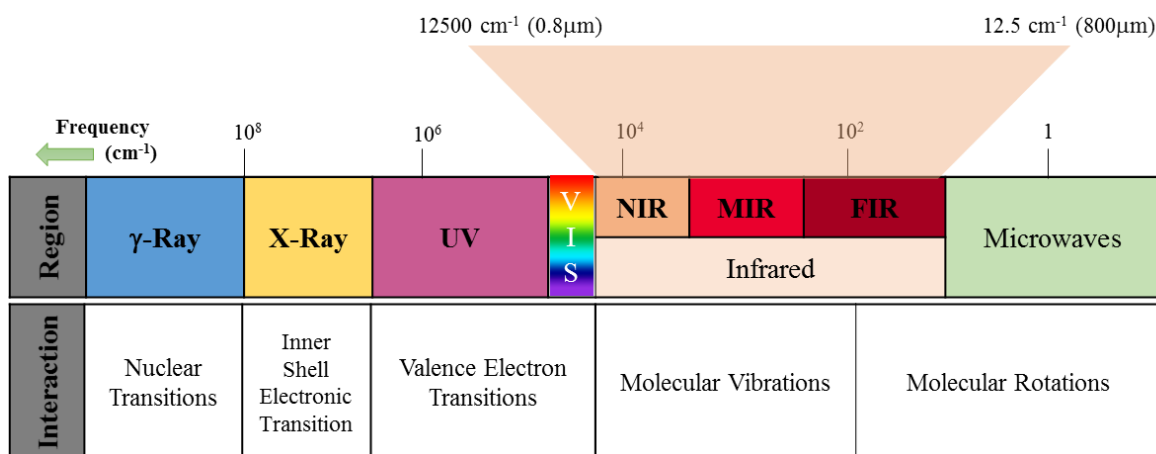


Figure 5.1: The electromagnetic spectrum bands and types of interaction representation.

Infrared spectroscopy is one of the classical methods for determination of small molecules due to the high information content in an infrared spectrum, and its high sensitivity to chemical composition and architecture of molecules. When passing through a sample with infrared light, certain frequencies are absorbed by the chemical bonds of the substance, leading to molecular vibrations [188]. Therefore, chemical bonds vibrate at specific frequencies determined by the shape of the molecule, the type of bond (single, double, triple), or the mass of the constituent atoms. This absorption and its corresponding vibrations are characteristic of each substance or molecule, so this technique allows us to obtain a different and unique fingerprint for each compound. For a molecule to be able to absorb infrared light, its dipole moment must undergo changes during vibration [189], [190]. When the frequency of a specific vibration is equal to the frequency of the IR radiation directed at a molecule, the molecule absorbs the radiation, and the associated energy is converted into various types of motions [188]. Thus, homonuclear molecules (such as O₂, N₂, or Cl₂) that are unable to undergo a net change during vibration or rotation are not able to absorb in the IR band [191]. On the contrary, more complex molecules have many bonds, and the frequencies at which these molecular oscillations occur are determined by the nature of those individual bonds within the molecule and by the different types of functional groups that would be directly associated with the oscillation [192]. Vibrations can also be conjugated, leading to two possible modes: stretching and bending (see Fig. 5.2).

Stretching vibrations:

They involve movements related to valence bond vibrations. These can be symmetrical, where the atoms of a molecule either move away or towards the central atom, but in the same direction; or asymmetrical, in which one atom approaches towards the central atom while the other departs from it.

Bending vibrations:

They are related to deformation vibrations, in which there is a change in the bond angle between the bonds of the central atom and the rest of the molecule. Depending on the plane in which the motion occurs, we can distinguish between four types of vibrations, depending on whether the motion occurs “in-plane” (scissoring and rocking), or “out-of-plane” (wagging and twisting).

- Scissoring: atoms move back and forth with respect to the central atom.
- Rocking: atoms swing back and forth with respect to the central atom.
- Wagging: two atoms oscillate up and below the plane with respect to the central atom.
- Twisting: one atom moving up the plane while the other moves down with respect to the central atom.

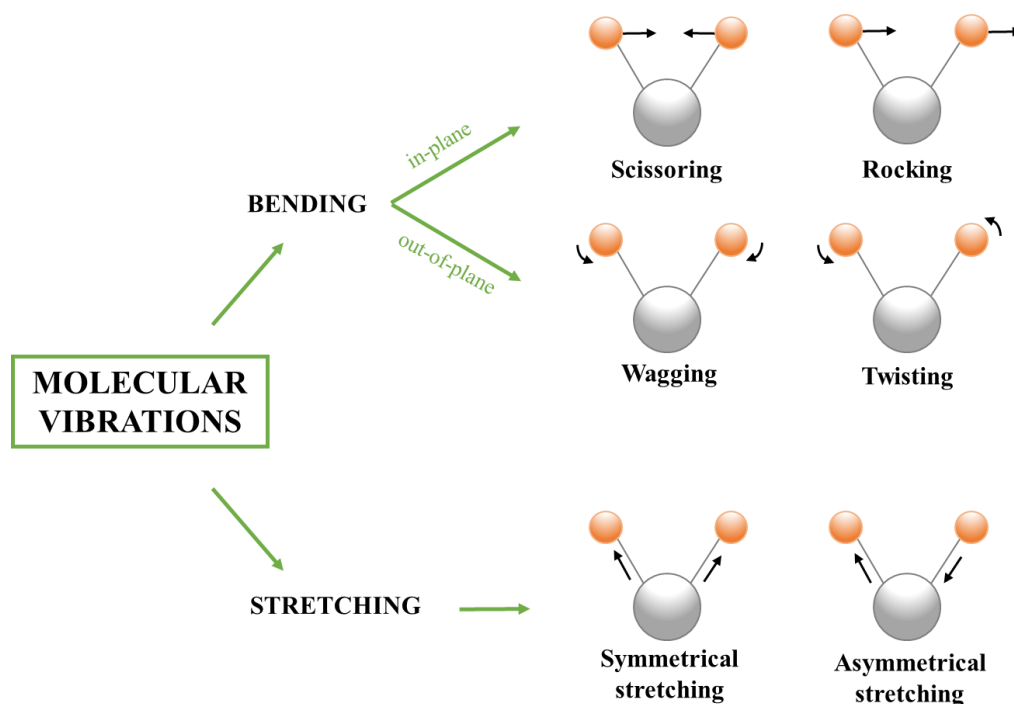


Figure 5.2: Schematic of molecular vibration types and classification.

In a molecule with more than two atoms, all types of vibrations are possible. Moreover, an interaction or coupling of different kind of vibrations can occur if they involve bonds with the same central atom. This coupling results in a change in the characteristics of the vibrations involved. When doing experiments in practice, it is common to observe a lower number of absorption peaks in these cases. According to Seamus, this can be due to some factors [193]:

- When the symmetry of the molecule is such that there is no change in the dipole moment due to one or more possible molecular oscillations.

- If a molecule can have two or more distinct vibrations that have nearly identical energy, the infrared absorption peaks of those processes can merge, and appear as a single one.
- If a molecular vibration produces an extremely small absorption, in some cases it will be too weak to be detected.

Although the infrared range covers a wide band of frequencies (12500 – 12.5 cm⁻¹ or 374 – 0.374 THz respectively), these type of fundamental molecular vibrations occur mainly in the MIR region, where two general areas can be found [11], [194]:

- The Functional Group Region (4000 – 1500 cm⁻¹): peaks characteristic of specific types of bonds, which can be used to identify whether a specific functional group is present.
- The Fingerprint Region (1500 – 400 cm⁻¹): peaks arising from complex deformation of molecules, which may be characteristic of its symmetry, or combined bands arising from simultaneously deformed multiple bonds.

5.2. IR Instrumentation

IR spectrometers are instruments to measure the electromagnetic radiation transmission of a sample as a function of wavelength (λ), or wavenumber (ν). The most important element must isolate the radiation from defined spectral regions, allowing us to differentiate between two types of instruments: Dispersive IR spectrometers and FTIR spectrometers, as shown in both panels of Fig. 5.3. IR radiation (both in dispersive and FTIR spectrometers) is obtained from the thermal emission of an appropriate source that produces a continuous radiation. Moreover, unlike UV-VIS spectrometers, in IR instruments the sample and reference compartment are always placed between the source and the monochromator (in dispersive instruments). This arrangement is possible because the IR radiation, unlike the UV-VIS radiation, is not energetic enough to cause the photochemical decomposition of the sample [191], [195].

Dispersive spectrometers were employed for the first time in the 1940s as a common analytical technique for organic compound characterization in laboratories [188], [196], [197]. This kind of devices are sometimes referred to as grating or scanning spectrometers, and its operating scheme is shown at Fig. 5.3 (a). In dispersive spectrometers, the source radiation passes alternately through the sample or the reference (in double-beam spectrometers), through a chopper that moderates the energy reaching the detector, and directed to a diffraction grating that disperses the light, separating the different wavelengths of light in the spectral range which are individually directed through a slit to the detector by moving the grating. Thus, each wavelength is measured one at a time and the grating-slit combination selects each wavelength being measured. In these measurements, a significant amount of energy is lost at both the input and output slits. Furthermore, in order to get a good signal-to-noise ratio (SNR), a certain amount of time must be spent at each position, until a good average signal is obtained. This is why, nowadays, it is a quite obsolete technology overcome by more modern, faster, and more accurate instruments, such as FTIR spectrometers.

FTIR spectrometers were developed for commercial use in the 1960s, but due to initial disadvantages such as lack of versatility or high cost of components, its use has only recently become widespread in laboratories. The major difference between a FTIR spectrometer and a dispersive IR spectrometer is the use of an interferometer instead of a monochromator (see Fig. 5.3 (b)). Most commercially available FTIR instruments are based on the Michelson interferometer, although other types of optical systems are also available [188], [195], [197]. The interferometer modulates radiation by splitting a beam light into two paths of similar strength and then recombines them in such a way that the intensity variations of the recombined beam can be measured as a function of the differences in the path lengths of the two beams. One beam of radiation from a source is collimated and incident on a beamsplitter, which transmits about half of the radiation and reflects the other half. The resulting twin beams are reflected by two mirrors, one of which is stationary and the other moving. The two beams are reflected from the mirrors and are recombined at the beamsplitter, resulting in an interference pattern [196]. The interferometer produces interference signals, which contain IR spectral information generated after a beam has passed through a sample, where some energy is absorbed and some is transmitted. The transmitted portion reaches the detector, which records the total intensity. Instead of examining each wavenumber in succession, as in dispersive IR spectroscopy, all frequencies are examined simultaneously. After the beam has passed through the sample or has been reflected, the measured signal is the resulting interferogram, which contains information from the entire IR region. Finally, the beam passes to the detector and the measured signal is digitalized and sent to the computer, where it is processed by the Fourier transform algorithm. This Fourier transformation of the signal can be viewed as a mathematical method of converting the individual frequencies from the interferogram, by using a mathematical procedure able to transform a function from the time domain to the frequency domain. The final IR is identical to that obtained from dispersive IR spectroscopy [195]. However, FTIR spectrometers has major advantages over a typical dispersive IR spectrometer, among which the following can be highlighted [195], [196]:

- Performance: because they are composed of few optical elements and due to the lack of slits that attenuate radiation, more energy reaches the sample and thus, FTIR instruments offer higher SNR than dispersive instruments.
- Speediness: in FTIR instruments, the emission time of a pulse is less than 1 second. In addition, every point in the interferogram contains information from each wavelength of light being measured unlike in dispersive instruments, where every wavelength across the spectrum must be measured individually as the grating scans.
- Very high resolution ($0.1 - 0.01 \text{ cm}^{-1}$). This makes it possible to analyze complex spectra where the total number of lines and spectral overlap make it difficult to determine individual spectral features.

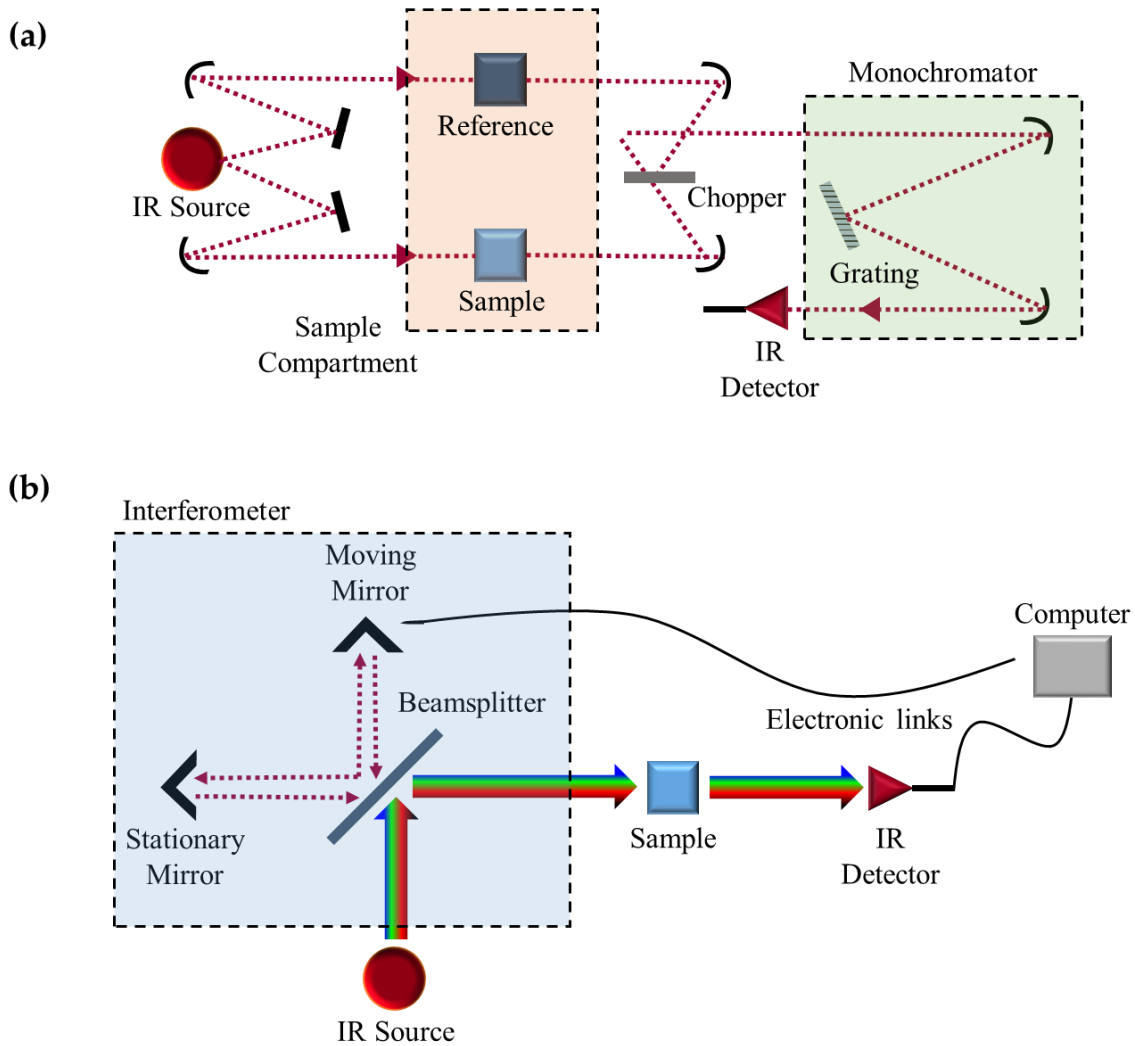


Figure 5.3: (a) Main components and operation scheme of Dispersive IR spectrometer.
 (b) Main components and operation scheme of Interferometer FTIR spectrometer.

In FTIR transmittance techniques, the sample is placed in the path of the IR incident radiation and scanned before reaching the detector (see Fig. 5.4(a)). However, there are times when transmittance measurement is not possible due to the sample's nature, or is not interesting for the study purpose. For these cases, accessories are available based on attenuated total reflectance (ATR).

ATR occurs when a beam of radiation enters from a denser medium (with higher refractive index, n_1) into a less dense medium (with lower refractive index, n_2). The fraction of the incident beam reflected increases as the angle of incidence increases. All incident radiation is reflected at the interface when the angle of incidence is greater than the critical angle, θ_c , which is a function of the refractive index of both mediums, as shown in equation 5.1 [198].

$$\theta_c = \arcsin \frac{n_2}{n_1} \quad (5.1)$$

Thus, the incident beam penetrates a very small distance beyond the interface into the less dense medium before complete reflection occurs and creates an evanescent wave, which extends beyond the surface of the crystal and projects into the sample in close contact

with the ATR crystal [172]. Some of that energy of the evanescent wave is absorbed by the sample, whereas the reflected radiation reaches the detector as it exits the crystal, as shown in Fig. 5.4 (b). In FTIR-ATR spectroscopy, the sample is placed onto an optically dense crystal that should present two main characteristics: it must be optically transparent at the IR frequency, so that little or no radiation is absorbed by the sensor material; besides, the ATR sensor crystal must have a higher refractive index than the surrounding medium, so the ATR acts as a waveguide and internally reflects light energy. Unlike the transmission technique, where the light must pass through the sample, the thickness of the sample is not relevant in FTIR-ATR because the intensity of the evanescent waves decreases exponentially with distance from the surface of the ATR crystal. This makes ATR ideal for studying a wide range of chemical reactions, as no sample preparation or dilution is required to obtain useful spectra [199].

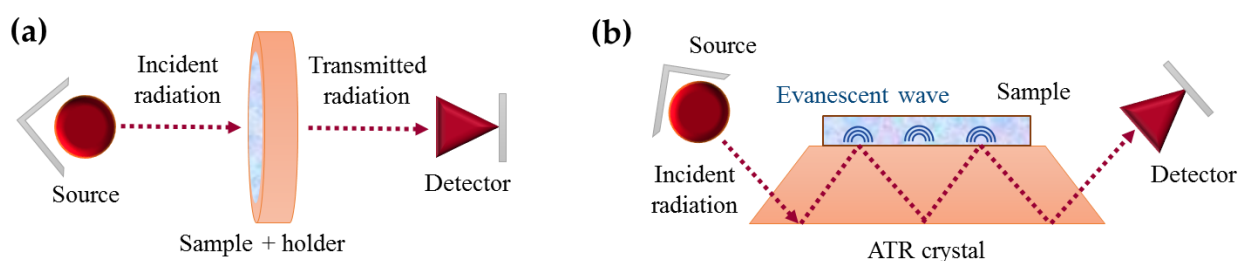


Figure 5.4: (a) Scheme of a transmittance FTIR detection method. (b) Schematic of FTIR-ATR detection method.

IR absorption information is usually presented as wavenumbers (ν), or wavelengths (λ) in the x-axis, and absorption intensity or percent transmittance as the y-axis. Wavenumber is a frequency quantity that indicates the number of times a wave vibrates in a unit of distance (cm^{-1} in spectroscopy applications) [188]. Although wavenumber representation is normally preferred, wavenumbers and wavelengths can be related using the equation 5.2:

$$\nu (\text{cm}^{-1}) = \frac{1}{\lambda (\mu\text{m})} \times 10^4 \quad (5.2)$$

The incident power can be theoretically divided into transmitted, reflected, and absorbed powers, which are related through the transmittance (T), absorbance (A), and reflectance (R) coefficients, as expressed in equation 5.3:

$$1 = T + R + A \quad (5.3)$$

However, in practice, reflectance is typically negligible in FTIR applications and therefore not taken into account. In such cases, T and A can be related as well by using the equation 5.4:

$$A = \log_{10} (1/T) = -\log_{10} (T) = -\log_{10} (I/I_0), \quad (5.4)$$

where I is the light transmitted by the sample, and I_0 is the incident light on the sample at a specific wavelength. Transmittance ranges from 0% to 100%, and provides better visual contrast

between the intensities of strong and weak bands, whereas absorbance extends from zero to infinity [200].

5.3. MIR applications in Food Systems

Due to increasing globalization in the food supply chain, food quality and safety has become a concern for producers, consumers, and governments [201], [202]. Although within the EU there is no precise definition of what is considered to be food fraud, the European Commission defined four criteria in 2018 including violation of food legislation, intentionality, economic benefit, and deception of consumers [202]. This adulteration can be defined more concretely as the process in which the quality of food is intentionally degraded, either by the addition of low-quality materials or by the removal of valuable ingredients [203]. Therefore, it is of great interest to investigate food fraud not only from an economic point of view, but also from a health perspective. In addition to intentional adulteration, degradation of food products can also occur due to changes in their chemical and structural composition in the process of transport and storage. So, studies on the quality of the food products and information on their chemical composition have also generated great interest in the scientific community in the past decades [204]–[208].

FTIR spectroscopy has become an “analytical fingerprinting technique”, which allows to identify structurally different compounds, since no two chemical structures have the same spectrum [206]. Because the Functional Group Region and the Fingerprint Region are contained in the MIR region, it has been of great interest in determining the structure of molecules. Although FTIR spectra are commonly complex and difficult to interpret, chemometrics has emerged as an effective tool for analytical purposes. Chemometrics was firstly introduced in 1972, and consists of an interdisciplinary method involving multivariate statistics, mathematical modeling, computer science, and analytical chemistry designed with the intention to describe the procedure for optimal measurement, and collect as much chemical information as possible by analyzing the data [209]. For all these reasons, the union of these two tools (FTIR and chemometrics) has been employed for several applications regarding food quality and security assessment since 1990s [188], [199], [210].

In the last years and with respect to food quality control, FTIR has been employed to estimate orange firmness and pectin content [211], to control the changes in cow milk production during the pregnancy stage [212], to determine fresh tomato quality [213], or to analyze the oxidation levels in oil-in-water emulsions [207], to highlight some of them. There are other types of products, such as wine or vinegar, which are under a protected designation of origin, according to specifications related to their chemical and sensory characteristics. In this context, spectroscopy techniques are able to provide a lot of information from a single measurement, allowing simultaneous consideration of both the individual contribution and the interactions of the different chemical components of a sample [214].

FTIR together with chemometrics also plays an important role in chemical characterization of meat products, and there are numerous studies using FTIR and chemometric techniques for meat-product applications, among which the following are worth mentioning: (1) the prediction of protein, fat, and moisture content in meat samples [215], [216]; (2) the determination of quality attributes of meat such as color, pH, or tenderness [217]–[219]; and (3) the monitoring of time-dependent changes in storage processes [220], [221].

5.3.1. Meat Oxidation

Meat and meat products are considered important sources of protein for the human body and have become an essential dietary ingredient due to their appreciated flavor and aroma. Among all the meats consumed in the world, foal meat presents some distinctive characteristics and marked differences in terms of composition with respect to other types of more commonly consumed meats such as beef, or pork [205], and its popularity is growing among the consumers. This is mainly because of its low fat content (around 2% of total lipids) and healthy fatty acid (FA) profile, and its high protein content [222]. Anyway, these physical and chemical properties of meat can undergo alterations during the process of preservation, transport or refrigeration and storage leading to low quality products. Specifically, one of the chemical processes that has a key role in terms of spoilage of meat quality is the oxidation of lipids and proteins (lipid and protein oxidation, respectively).

Lipid oxidation (L_OX) has been the object of numerous studies over the years, what has led to gain knowledge on the principal mechanisms involved in fatty acids oxidation and parallel degradation. However, this is a complex process, and finding a suitable method for quantifying lipid oxidation remains a difficult task. The two most commonly used procedures for this purpose are the following:

- Thiobarbituric Acid Reactive Substances method (TBARS analysis), based on the detection of Malondialdehyde (MDA) and other aldehydes generated in the oxidative breakdown of polyunsaturated fatty acids (PUFAs). Despite its ease and simplicity, the method is not selective for MDA, and also reacts with other aldehydes, carbohydrates, amino acids, and nucleic acids [223], resulting in considerable overestimation, and low reliability due to the variability of the results.
- Chromatography, within which we can use Gas Chromatography coupled to Mass Spectrometry (GC-MS), for the analysis of lipid hydroperoxides (prior extraction of these hydroperoxides is necessary) [224]; or HPLC, which allows analyzing compounds with different characteristics of volatility, molecular weight or polarity [225]. However, sample preparation is often tedious and also requires prior lipid extraction. Thus, these chromatography-based techniques involve much harder and time-consuming experimental work, as well as a high level of complexity in data processing.

On the other hand, protein oxidation (P_OX) has not been as extensively studied in meat quality research, despite the fact that protein oxidation has been shown to significantly affect the functional properties of meat and, in particular, foal meat [226]. It was not until the mid-90s when it was observed that proteins could also be susceptible to oxidation reactions. Today we know that protein oxidation is responsible for the appearance of abnormal textures in fresh meat and meat-based products, but it also triggers an irreversible loss of essential amino acids and an alteration in the digestibility of oxidized proteins, leading to a loss of nutritional value in meat and meat products [227]. To quantify this oxidation process, two main groups of quantification methods are usually employed:

- The quantification of the total content of protein carbonyls by using the Dinitrophenylhydrazine (DNPH) technique. The procedure involves a simultaneous determination of carbonyl derivatives and protein content of the sample [228]. The original method from Oliver et al. (1987) [228] was

developed for analyzing oxidative stress in biological samples and has been afterwards employed with slight modifications by food scientists in recent years. Despite its popularity, drawbacks of this procedure include lack of specificity and a possible overestimation of the carbonyl due to other artifacts, which may result in an underestimation of the overall oxidative damage of proteins, and an overestimation of the amount of protein carbonyls.

- The Specific Protein Carbonyls Method, referred to the study of α -aminoadipic (AAS) and γ -glutamic semialdehydes (GGS) as protein oxidation biomarkers. Both semialdehydes are very sensitive to acid hydrolysis and because of this, a derivatization procedure is required for stabilization of the compounds. In comparison with DNPH method, these procedures of AAS and GGS detection are more complicated and equipment demanding, as for example pre-processes of derivatization are needed and the reagents employed are more expensive than those of the DNPH method.

5.4. Our work (Paper F): Application of MIR spectroscopy to Lipid and Protein Oxidation Quantification in Foal Meat

According to the demands of the agricultural industries, it is of vital importance to develop food analysis methods that combine speed, ease of use, little or no sample preparation, and no sample destruction. As far as we have seen, most classical techniques show several weaknesses regarding sensitivity, susceptibility, and/or overestimations (TBARS and DNPH); while more accurate ones present much more complex experimental procedures and tedious preparations and post-processing data (GC-MS and HPLC).

Our work [PAPER F] broadens the study of lipid and protein oxidation marker compounds in foal meat, employing the technology of Attenuated Total Reflectance-Fourier Transform Mid-Infrared Spectroscopy (ATR-FT/MIR). Starting from the marker compounds extracted from a total of 23 foals from two groups differentiated by age at slaughter and type of feeding, a study of their absorbance spectra is carried out in order to try to establish prediction models (calibration and validation). Thus, the main objectives of this work are three:

- To decide if this technique (ATR-FT/MIR) is useful to estimate the value of oxidation marker compounds, due to its greater ease of use compared to the traditional methodology.
- To determine whether it is preferable to perform a pre-extraction of the oxidation marker compounds before performing the analysis of the spectra, instead of performing the measurements directly on raw meat.
- To determine the influence of slaughter age and feeding regime of the animals used on the degradation of lipids and proteins of foal meat.

In order to achieve these objectives, the following series of experimental and numerical tasks have been performed:

- i. ATR-FT/MIR spectroscopy analysis of previous L_OX and P_OX extracts and spectral characterization.
- ii. ATR-FT/MIR spectroscopy analysis of direct raw meat samples and spectral characterization.
- iii. Construction and comparison of prediction models for both ATR-FT/MIR analysis carried out in previous steps.

As a final point, a comparison of the results with those obtained by means of the classical techniques in a previous work, has been carried out [205]. This study has shown that prediction models were promising to estimate the values of protein and lipid oxidation markers, but with more consistent results in previously extracted compounds rather than making the analysis on raw samples. Therefore, more research is needed on the application of MIR spectroscopy directly on raw meat to improve the estimation of the predictive models. Nevertheless, MIR spectroscopy emerges as an interesting alternative to traditional meat composition analytical methods, which are time-consuming and expensive.

Author contribution to this work:

- ATR-FT/MIR spectroscopy analysis and spectral characterization.
- Manuscript preparation and writing.



Article

Lipid and Protein Oxidation Marker Compounds in Horse Meat Determined by MIR Spectroscopy

Irati Jáuregui-López ^{1,2}, Fernando Zulategi ³, María José Beriain ³ , María Victoria Sarriés ³ , Miguel Beruete ^{1,2} and Kizkitza Insausti ^{3,*}

¹ Antennas Group-TERALAB, Campus de Arrosadía, Universidad Pública de Navarra (UPNA), 31006 Pamplona, Spain; irati.jauregui@unavarra.es (I.J.-L.); miguel.beruete@unavarra.es (M.B.)

² Multispectral Biosensing Group, Navarrabiomed, Complejo Hospitalario de Navarra (CHN), Instituto de Investigación Sanitaria de Navarra (IdiSNA), Universidad Pública de Navarra (UPNA), Irunlarrea 3, 31008 Pamplona, Spain

³ Research Institute for Innovation and Sustainable Development in Food Chain (IS-FOOD), Campus de Arrosadía, Universidad Pública de Navarra, 31006 Pamplona, Spain; zulategui.79089@e.unavarra.es (F.Z.); mjberiaín@unavarra.es (M.J.B.); vsarriés@unavarra.es (M.V.S.)

* Correspondence: kizkitza.insausti@unavarra.es

Received: 14 November 2020; Accepted: 6 December 2020; Published: 9 December 2020



Abstract: This work broadens the study of lipid and protein oxidation marker compounds in foal meat, employing the technology of Attenuated Total Reflectance-Fourier Transform Mid-Infrared Spectroscopy (ATR-FT/MIR, shortened in the following as MIR). As a main objective, marker compounds from 23 foals were extracted and their absorbance spectra were measured to establish prediction models (calibration and validation) between them and classical quantification analysis of the compounds. Another objective was to ascertain whether a previous extraction of the marker compounds before executing their MIR analysis is preferable compared to direct MIR measurements on the raw meat samples. In this context, marker compound results (TBARS between 0.4387 and 2.1040, and carbonyls between 4.07 and 4.68) showed more consistent predictive models than the ones achieved using quantitative analysis of the spectra obtained from the raw meat. Lipid oxidation compounds predictive models obtained in this work offered an R^2_{cv} of 63.18% and protein oxidation R^2_{cv} obtained in this project showed a value of 54.24%. Thus, MIR technology arises as a promising tool to identify and quantify products derived from lipid and protein oxidation in fresh foal meat.

Keywords: MIR (Mid-Infrared) spectroscopy; lipid oxidation markers; protein oxidation markers; foal meat

1. Introduction

While historically horse breeds used for consumption came from old animals previously employed for field labor, nowadays these animals come from selected breeds with meat production purposes [1]. Around 700,000 foals graze in Spanish lands [2] and thousands of livestock heads are slaughtered annually, e.g., 38,200 during the year 2019, according to the data provided by the Ministry of Agriculture, Fisheries and Food of the Spanish Government [3]. Thus, Spain is positioned as an important foal meat exporter and it is one of the biggest European producers. Foals raised for commercialization are animals between 7 and 9 months of slaughter age (*lechales* foals), or between 15 to 16 months of slaughtering age (*quincenos* foals) [4], demystifying the extended belief that horse meat always comes from old and rejected animals employed for other purposes.

Foal meat composition presents several differences with other types of meat. Its main peculiarity is its higher protein content and lower fat content than other popular meats. Concretely, foal meat presents a 2% of total lipids in its composition, 32% of which are saturated fatty acids (SFA), while lean

beef has up to 5.4% of fat, of which 41% are SFA [5]. In the last years, several works and results about foal meat's lipid composition can be found in the literature and it has been observed that, regarding fatty acids (FA) in intramuscular fat foal muscles, the most predominant ones are Polyunsaturated Fatty Acids (PUFA), ranging from 41.1 to 48.2% of the total methyl esters [6]. With respect to proteins, foal meat is characterized by having a higher proportion of protein content than beef or pork, and with a high biological value, as it presents around 40% of essential amino acids [7].

Oxidation is one of the main causes, if not the principal, of meat quality loss during the meat preservation process as it affects lipids, proteins, carbohydrates and vitamins in meat, producing changes in the meat consistency, texture, color and sensory properties in general. During the aging and storage time, the close relationship between lipid and protein oxidation (L_OX, P_OX) in fresh meat and its influence on the deterioration of meat quality is already known [8]. Over the years, L_OX has been the subject of plenty of studies, leading to a substantial knowledge of the principal mechanisms involved in PUFA oxidation and parallel degradation. The oxidation process involves the degradation of PUFA or vitamins, among others, giving rise to the generation of free radicals, more susceptible to suffer oxidation, leading to changes in the meat composition and its nutritional value [9]. L_OX is a convoluted mechanism that involves complex chains of reactions that gives rise to different primary (peroxides), and secondary oxidation compounds [10]. Associated changes to L_OX constitute the principal cause of degradation in meat and meat products, as they trigger bad odors and flavors formation, as well as color alteration, all of it consequently leading to a loss in the organoleptic quality of the final product. In addition, this L_OX also leads to a loss in the meat's nutritional value, and to the formation of potentially harmful compounds related to different pathologies [11].

L_OX, through the oxidant activity of primary and secondary L_OX products, is also thought to promote the oxidation and degradation of proteins. According to Pignoli et al. [11,12], the different chemical modifications in specific amino acid chains, or the peptide backbone, can lead to changes in the physical properties of the proteins, with different chemical manifestations, such as gain of carbonyl derivatives, formation of intra and intermolecular cross-links, or loss of tryptophan fluorescence, among others. Color changes in foal meat occur more quickly than in other meats such as beef due to a higher iron content, which affects the myoglobin [13]. Besides, tenderness is usually greatly affected by P_OX. Meat becomes harder and less juicy due to changes in protein cross-linking, due to oxidation reactions [14]. P_OX is mainly produced due to the presence of free radicals that act as oxidizing agents. These oxidation agents act on the side chains of amino acids, causing the loss of the amino group, and the formation of carbonyl groups. In addition, L_OX usually has a direct influence in P_OX. Nevertheless, the protein degradation can also occur without L_OX. The carbonyl formation is also favored by refrigerated storage and freezing of the meat, as well as by culinary treatments. Contrary to what happens to L_OX, protein degradation has not been as deeply studied in foal meat quality researches [15], despite having been proved that P_OX has an important effect on the functional properties of meat, and on foal meat in particular [12].

In this context, Lipid/Carbonyl radicals, hydroperoxides and malonaldehyde (MDA) play a vital role in promoting in vivo oxidative reactions, which have been proven to not only reduce the quality of meat and food but also to increase health risks. That is why through the years different techniques have been developed in order to detect and measure some of these compounds. Concretely, quantification of milligrams of MDA per kilogram of meat sample by the Thiobarbituric Acid Reactive Substances (TBARS) analysis; and quantification of the total amount of carbonyls by using the Dinitrophenylhydrazine (DNPH) technique are frequent methods for assessing L_OX and P_OX, respectively. These techniques are time consuming, though. Thus, there is an increasing interest in the food industry on the application of new, fast, and reliable techniques. In this way, Attenuated Total Reflectance-Fourier Transform Mid-Infrared Spectroscopy (ATR-FT/MIR, shortened in the following as MIR) might be a practical option. MIR spectroscopy applications in food analysis are diverse, although its current use is limited [16,17]. In this context, the objective of this research was to study the usefulness of MIR technology to estimate the values of L_OX and P_OX marker compounds in foal meat,

due to its high susceptibility to oxidation. To do so, MIR spectra were recorded on L_OX and P_OX marker compounds previously extracted from raw meat samples. Then, a second objective, was to study if MIR technology is more useful when applied on previously extracted oxidation compounds or when measured directly on raw meat samples.

2. Material and Methods

2.1. Animal Management and Meat Sampling

In this study, two different types of animals (differing in age and feeding diet) and four meat aging times were used in order to obtain samples with potentially different oxidation levels.

Foals were kept with their mothers and allowed to suck freely on the pasture from birth to weaning at the age of 6 to 7 months. Then, foals were randomly divided in two groups to be slaughtered at two different ages: 12 foals were slaughtered at 26 months of age (784 ± 37 days) which correspond to the “Adult” (A) group. The diet (Appendix A) of the A group was supplemented with a standard/conventional concentrate (C). Then, 11 foals were slaughtered at 13 months (403 ± 30 days), which corresponds to the “Young” (Y) group, whose diet was supplemented with a linseed-rich concentrate (L) (5%). This fattening period lasted around 104 days (± 10 days) in both groups.

Foals were transported 50 km to the abattoir the day before slaughter in compliance with current European regulations (Council Regulation 1/2005EC, 2005), and were stunned with a captive bolt, slaughtered, and dressed according to the specifications outlined in the European legislation (Council Directive 93/119/EC, 1993). Twenty-four h post-mortem, Longissimus dorsi (LD) muscles of each of the animals were extracted from the left half-carcasses. The LD muscle was sliced into 20 mm (± 0.2) thick cuts, and steaks were aged under vacuum (99%) and in refrigerated chambers at 2 ± 1 °C and under dark during the corresponding days (0, 4, 8, or 12 days for the Y-L group; and 4 days for the A-C group). Once these periods elapsed, samples were frozen during 3 months (± 10 days). After that, samples were thawed during 24 h under refrigerated conditions (2 ± 1 °C) before analysis. Meat from the A-C group was aged 4 days, as this is the standard aging time for this type of meat. Meat from the Y-L group was aged longer in order to promote potential oxidation of the meat due to the linseed diet fed to the foals.

2.2. Experimental Design

Once the meat cuts from each animal were fridge-stored for the time required in the analysis, two different parts in the design were performed according to two analyses: L_OX quantification by TBARS and MIR spectroscopy analysis; and P_OX quantification by DNPH method and MIR spectroscopy analysis. In both L_OX and P_OX analysis, MIR spectra were recorded to previously extracted oxidation compounds, and directly on raw meat samples. A scheme of the experimental design is shown in Figure 1.

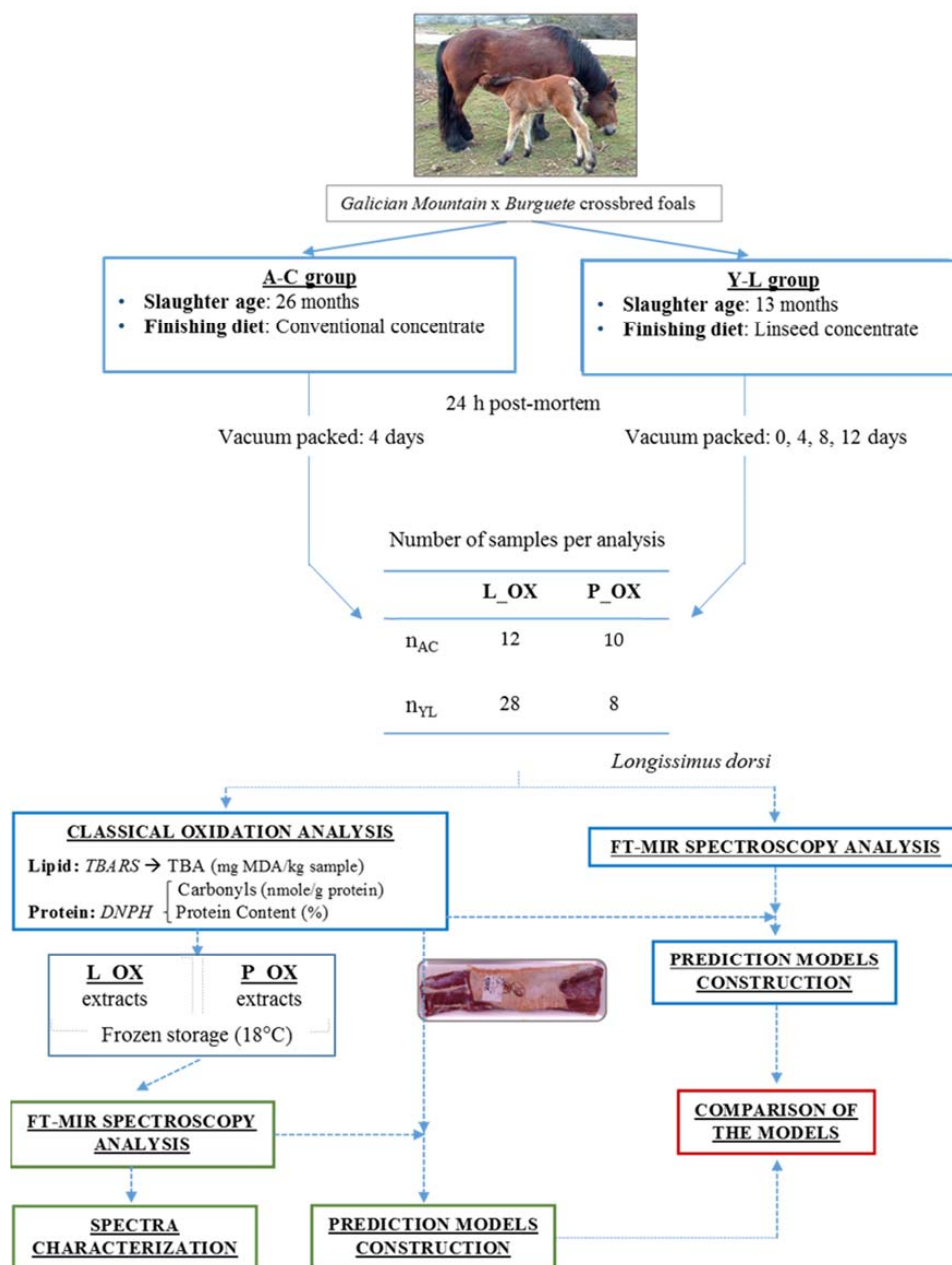


Figure 1. Scheme of the experimental design for both models performed in this work (n_{AC}: number adults on concentrate; n_{YL}: number young on linseed; TBARS: Thiobarbituric Acid Reactive Substances; DNPH: Dinitrophenylhydrazine; L_OX: lipid oxidation; P_OX: protein oxidation).

2.3. Analytic Method for Both Lipid and Protein Oxidation Quantification

2.3.1. Lipid Oxidation Quantification: Thiobarbituric Acid Reactive Substances (TBARS) Analysis

L_OX was evaluated through the method proposed by [18], with some variations applied. Two grams of meat were minced and 10 mL of 5% trichloroacetic acid (TCA) was added. Then, it was homogenized with an Ultra-Turrax (IKA T25 digital ULTRA-TURRAX, IKA-Werke GmbH & Co., Staufen im Breisgau, Germany) for 1 min at 11,500 rpm. The homogenized sample was stored at $-10\text{ }^{\circ}\text{C}$ for 10 min and was centrifuged at 5000 rpm, for 10 min at $4\text{ }^{\circ}\text{C}$. Supernatant was filtered using a Filter-lab no 1246 filter on ice. One mL of the filtered substance was taken and reacted with 1 mL 0.02 M TBA. Immediately, it was incubated in a water bath at $96\text{ }^{\circ}\text{C}$ for 40 min. Then, tubes were chilled and centrifuged at 10,000 rpm for 4 min at $20\text{ }^{\circ}\text{C}$. Part of the extract was used for MIR measurement

(L_OX marker compound). Absorbance was measured on the rest of the extract at 530 nm employing a UV/vis Spectrophotometer with diodes detector, model Shimadzu UV-2101PC. TBA values were calculated from a pattern curve of 1,1-3,3 tetraethoxypropane (TEP) and expressed as mg of MDA/kg of meat sample.

2.3.2. Protein Oxidation Quantification: Dinitrophenylhydrazine (DNPH) Method

P_OX, measured as total carbonyl content, were quantified according to the method described by Oliver [19] and modified by Vuorela [20], commonly known as the DNPH method. Each of the meat samples was homogenized with 20 mL of 0.6 M NaCl for 60 s using an Ultra-Turrax homogenizer (IKA T25 digital ULTRA-TURRAX, IKA-Werke GmbH & Co., Staufen im Breisgau, Germany). Two aliquots of homogenate were taken (0.1 mL) and were transferred into Eppendorf vials. Proteins were precipitated with 10% (1 mL) TCA and were centrifuged for 5 min at 10,000× *g*. One of the pellets was treated with 2N HCl (1 mL) in order to quantify proteins and the other one with 0.2% 2,4-dinitrophenyl hydrazine (DNPH) in HCl 2M (1 mL) to quantify carbonyls. Part of the extract was used for MIR measurement (P_OX marker compound). Protein concentration samples (*p*) were measured spectrophotometrically attending to absorbance at 280 nm (Spectrophotometer UV/vis with diode detector, Shimadzu UV-2101PC, Mettler-Toledo S.A.E. L'Hospitalet de Llobregat, Barcelona, Spain) using Bovine Serum Albumin (BSA) as the standard. Carbonyl content was expressed as nmol of carbonyl compounds per milligram of protein using an extinction coefficient of 21.0 mM⁻¹ cm⁻¹ at 370 nm.

2.4. MIR Spectra Acquisition

The measuring instrument used in this research was a FTIR Vertex 80v spectrometer (Bruker, Ettlingen, Germany). The measurements were made with an ATR Platinum (Bruker, Rheinstetten, Germany) inserted in the FTIR. The spectrometer was equipped with a Globar source (operation bandwidth, 6000–50 cm⁻¹), a beam splitter of KBr (10,000–400 cm⁻¹), and DLaTGS detector (10,000–250 cm⁻¹). The active area of the ATR Platinum was a diamond crystal (2 × 2 mm, approximately) on top of which the samples under test were deposited.

First, a reference spectrum was taken with the ATR device empty, and then the spectrum of each of the samples was measured. The different samples were placed on the diamond crystal of the ATR, ensuring that the entire crystal surface was completely covered and that there was a perfect contact between the samples and the crystal. Once every sample measurement was performed, the ATR diamond crystal was cleaned with a piece of Berkshire Durx[®] 670 optic cleaning wipe using distilled water and isopropyl alcohol to leave it ready for the next sample's reference measurement. In order to establish the adequate number of replicates, 32 scans were averaged in the 4000 to 400 cm⁻¹ spectral range and were recorded with a resolution of 4 cm⁻¹. It was observed that, on average, 1 out of 15 measurements of the same sample showed outlier or anomalous spectral results in comparison to the others (this was performed for a total of 105 measurements from 10 different samples). In this way, it was established that repetitions of the same sample would be enough to obtain consistent and similar results. Thus, taking into account the number of extracts used (see Figure 1) a total of 240 measurements were performed for L_OX determination, and a total of 108 measurements were carried out for P_OX determination. Every measurement provided a single and unique spectrum, which was saved in the PC in order to employ them for the chemometric model of the data obtained. The spectra acquisition of the raw meat samples was done and described in a previous work [21].

2.5. Statistical/Chemometric Treatment

The analysis of variance (ANOVA) was performed using the General Linear Model (GLM, SPSS 23.0, Chicago, IL, USA) to study the TBARS and carbonyl content of the samples. Significant differences (*p* < 0.05) between groups were tested using Tukey's test.

In order to perform the quantitative analysis, the software package QUANT 2, from Bruker's Opus v.7.0, was used. The purpose of QUANT 2 is to perform quantitative analysis of unknown multicomponent samples. A chemometric model, using a number of calibration samples of known composition that were representative of the studied system, was used. Outliers and negative bands were discarded and MIR spectra of the remaining samples would then be used by QUANT 2 to calculate a calibration function, which essentially is the model used for the analysis of unknown samples.

The cross validation method was employed, which uses the same set of samples for calibration and validation. In this method, a representative set of samples for a multicomponent system is used to calibrate and validate a system. Before starting the calibration, one of the samples was excluded from the entire set of samples, and used for the validation process. The remaining samples were then used to calibrate the system. In order to do this, a set of calibration samples was measured by MIR spectroscopy. With the obtained spectral results, the main absorption peak amplitudes for each substance were determined and plotted versus different known concentrations. Thus, the resulting calibration graph was used to evaluate the concentration of an unknown sample, by measuring its absorption peaks and comparing them with the resulting graph. The information contained in the calibration samples spectra was then compared to the information of the known concentration values using a Partial Least Square (PLS) regression. This method assumes that systematic variations observed in the spectra are a consequence of the changes in the concentration of the components.

Multivariate calibrations make use of not only a single spectral point but they take into account spectral features over a wide range. Therefore, the analysis of overlapping spectral bands or broad peaks becomes feasible. Multivariate calibrations require a large number of calibration samples and yield a large amount of data (several spectra with hundreds or thousands of relevant data points). In order to conveniently handle so many results, the spectral response and its concentration values were written in a matrix form, where each row in the spectral data matrix represented a sample spectrum, and the concentration data matrix contained the corresponding concentration values of the samples. The matrices were decomposed into their Eigenvectors, by which it is possible to define a spectral characteristic without using all its components. Thus, only the relevant principal components were taken into account, leading to a considerable reduction in the data amount. Finally, a PLS regression algorithm was deployed to find the best correlation function between spectra and concentration data matrix.

Data Preprocessing

In order to ensure the reproducibility of the calibration samples, several spectra of each sample were acquired. Due to the inhomogeneity of the samples, a spectral normalization was first performed. Then, data preprocessing procedures were applied to align the different spectra. Data preprocessing can eliminate variations in offset or different linear baselines and is useful to ensure a good correlation between the spectral data and the concentration values. In this study, different preprocessing methods were used for L_OX and P_OX results. When working with the marker compound samples, two preprocessing steps were applied. First, a whole calibration/validation, using the entire data set with all the studied samples, was made. Due to the fact that there were many samples, and in order to homogenize the spectral results, a second calibration/validation model with reduced data was also elaborated by taking the average of six repetitions for each sample, and were referred to as the Mean Set.

Regarding the L_OX results acquisition, two methods were employed: Standard Normal Variable Vector Normalization (SNV), which normalizes a spectrum by first calculating the average intensity value and subsequent subtraction of this value from the spectrum; and then calculates the sum of the squared intensities, and divides the spectrum by the square root of that sum; and a Linear Offset Subtraction, which shifts the spectra in order to set the absorbance minimum to zero.

In the case of P_OX results, a combination of two methods was employed. First, a Multiplicative Scatter Correction, which performs a linear transformation of each spectrum for it to best match the

mean spectrum of the whole set. Second, a First Derivative method, which calculates the first derivative of the spectrum, emphasizing the steep edges of a peak, was employed to obtain the carbonyl content results. Finally, a Min-max Normalization method (first subtracts a linear offset and then sets the absorbance-maximum to a value of 2 by multiplication with a constant) was employed to obtain the results of the carbonyl content using the Mean Set.

As a final step, a discussion of the results obtained with the quantitative analysis of the spectra from the oxidation marker compounds (L_OX and P_OX) vs. the ones obtained in the quantitative analysis of the spectra analyzed directly from raw meat in a previous work [22] was carried out.

3. Results and Discussion

3.1. Lipid and Protein Oxidation Quantification

The L_OX and P_OX quantification was done using the analytically obtained lipid (TBA) and protein (DNPH) oxidation values from Y-L and A-C animals. As shown in Table 1, TBA content showed an increasing trend, though non-significant, with ageing time (0–12 days), meaning a higher L_OX in aged samples, as it was expected from the results found in [8]. As it can be observed in Table 1, the results for the A-C group in TBA analysis at day 4 showed higher MDA content, with 2.1 mg MDA/kg, in comparison to the 0.44 mg MDA/kg of meat obtained for the Y-L group, at an ageing time of 4 days ($p < 0.001$). These results suggest that the MDA content in foal meat increases as the slaughter age increases, most likely due to a higher intramuscular fat percentage of older animals [23]. Nevertheless, if redoing the statistical analysis by subtracting the AC group, significance in the data is still found for different days of ageing (data not shown).

Table 1. Lipid and protein oxidation quantification of Young-Linseed (Y-L) and Adult Conventional (A-C) foal meat.

	TBA (MDA/kg)	Total Carbonyl (nmole/mg)
Y-L 0d	0.4525 ^a	4.07 ^a
Y-L 4d	0.4387 ^a	4.20 ^{ab}
Y-L 8d	0.505 ^a	4.35 ^{ab}
Y-L 12d	0.5287 ^a	4.28 ^{ab}
A-C 4d	2.1042 ^b	4.68 ^b
SEM	0.054	0.059
<i>p</i> -VALUE	0.000	0.009

TBA: Thiobarbituric Acid; Means within a column lacking a common superscript letter differ ($p < 0.05$).

According to Zakrys-Waliwander [14] and Ruiz [21], P_OX in beef samples increases with oxygen and conservation ageing time. For this reason, similar behavior was expected for P_OX of foal meat than the one obtained for TBA. Nevertheless, the results presented in Table 1 do not show any apparent increase or decrease, nor any clear pattern followed by the samples. As shown in Table 1, differences in the carbonyl content were only due to the differences observed between the A-C group and the Y-L-0d group ($p < 0.01$). This way, although it is demonstrated that TBA increases as the slaughtering age does, there is no evidence that it occurs in a similar way in the case of carbonyls. Regardless, both oxidative processes should be taken into account for a correct determination of meat quality, allowing the evaluation and differentiation of the oxidative changes that take place in lipids and proteins.

3.2. Spectral Characterization

In this section, the spectral MIR characteristics of the analyzed substances are studied, with a total of 348 analyzed spectra, shown in Figures 2 and 3. As it can be observed, a moderate variability is shown in L_OX and P_OX content extract samples' spectra (see Figure 3). In order to study the different peaks present in the spectra, a bibliographic revision of the main absorption peaks of these kinds of

substances was performed. Table 2 contains a compilation of the main wavenumbers associated to their functional groups according to the bibliography consulted, in relation to the compounds considered.

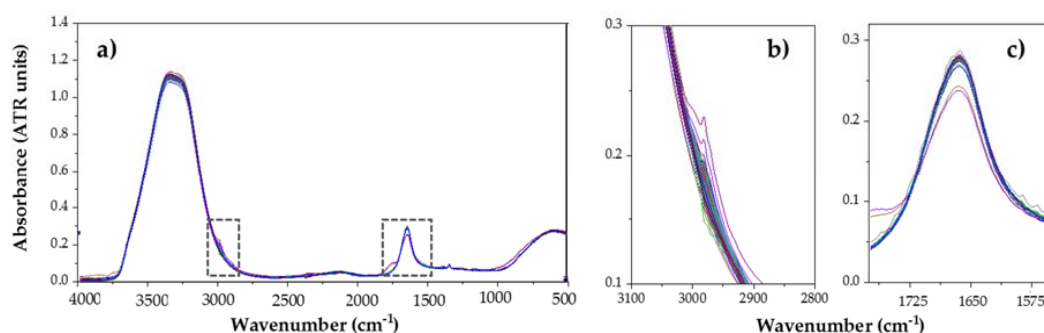


Figure 2. (a) ATR MIR spectra (Attenuated Total Reflectance-Fourier Transform Mid-Infrared Spectroscopy) of L_OX (lipid oxidation) samples (240 analyses) and expanded areas of interest: (b); 2800–3100 cm^{-1} . (c) 1525–1750 cm^{-1} .

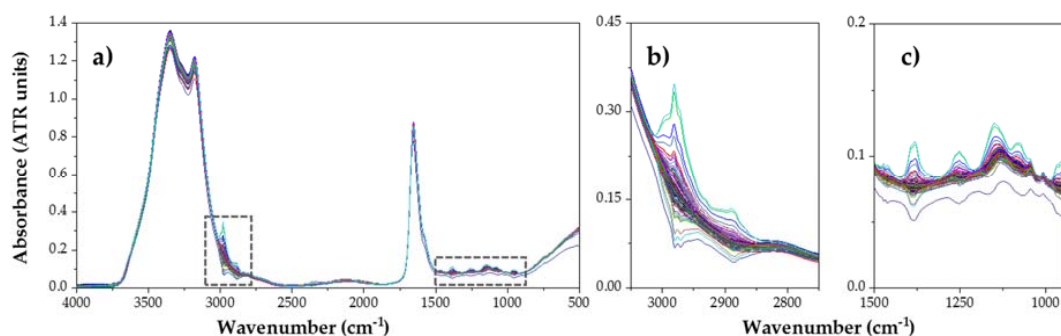


Figure 3. (a) ATR MIR spectra of P_OX (protein oxidation) samples (108 analyses) and expanded areas of interest: (b) 2750–3100 cm^{-1} ; (c) 950–1500 cm^{-1} .

Table 2. Compilation of principal wavenumbers associated to functional groups.

Wavenumber (cm^{-1})	Assignment	Reference
3700–3200	Stretching vibration of bonded and non-bonded -O-H groups (water vibration)	[24]
3500–3300	Amines	[25]
~3400	Amide A (N-H stretching vibrations)	[25]
~3100	Amide B (N-H stretching vibrations)	[26]
3000–2850	Symmetrical and asymmetrical stretching vibrations of C-H groups (Alkanes); fatty acids backbone	[27]
1659–1653	=C-H stretching vibrations/Amide I (C=O stretching vibration)/O-H bending vibrations in water	[25,28]
1680–1620	Stretching vibration of C=C groups (Alkenes)	[29]
~1640	Hydrogen covalent bonds bending of water	[30]
1580–1540	C-O vibrations/Amide II (N-H bending vibration mixed with C-N stretching vibration)/Aromatic -C=C stretching vibrations	[31]
1400–1200	Amide III (N-H, C-C and C-N vibrations)	[26]
970–920	Trans = C-H out-of-plane bending	[32]
610–711	Amide V (C-N and N-H vibrations)	[26]
900–400	Stretching of O-H (water vibration)	[24]

3.2.1. Spectral Characteristics of Lipid Oxidation Marker Compounds

Among all the absorption peaks shown in the Figure 4, the most significant one is the band located between 3700 cm^{-1} and 3100 cm^{-1} , which corresponds to the wide band of high absorption associated to the hydroxyl groups O-H of water. In this case, it hides the possible presence of other peaks. In the same way as before, vibrational oscillations of these O-H groups provoke the apparition of another wide band between 900 cm^{-1} and 400 cm^{-1} . After these two regions, the band with the highest absorption appears between 1680 cm^{-1} and 1590 cm^{-1} , with a peak at 1636 cm^{-1} . This area, according to [29], corresponds to the stretching vibrations of C=H groups (Alkenes). However, the peak placed at 1640 cm^{-1} corresponds to the hydrogen covalent bonds bending of water. This way, results are not clear enough to determine the type of bond that provokes that absorbance. Moreover, a weak peak can also be observed at 2981 cm^{-1} , again associated to the different vibrational oscillations of C-H bonds. This one in particular was assigned to the stretch of C-H in the study of Tertiary Amine-Triethylamine [33]. Finally, it can be clearly observed that an isolated peak in the Fingerprint Region (from 1500 to 400 cm^{-1}) [29] was present in each of the 240 samples measured. The peak is located at 1336 cm^{-1} and has a low but repeated absorption from 0.086 to 0.095 (mean = 0.088). No reference regarding this particular peak has been found in any of the works consulted in the literature. Nevertheless, it is located in the region correspondent to CH₃ symmetric deformation and CH₂ wagging band (1400 – 1200 cm^{-1}), so it is supposed to belong to this kind of peptide complex band. As a curiosity, the only reference found regarding the apparition of a peak at this particular frequency was in the study of [34], in which they found that the band corresponding to 1336 cm^{-1} may be considered a sensitive marker for the identification of *Lactobacillus casei*, used to evaluate lactic fermentation in fermented foods production.

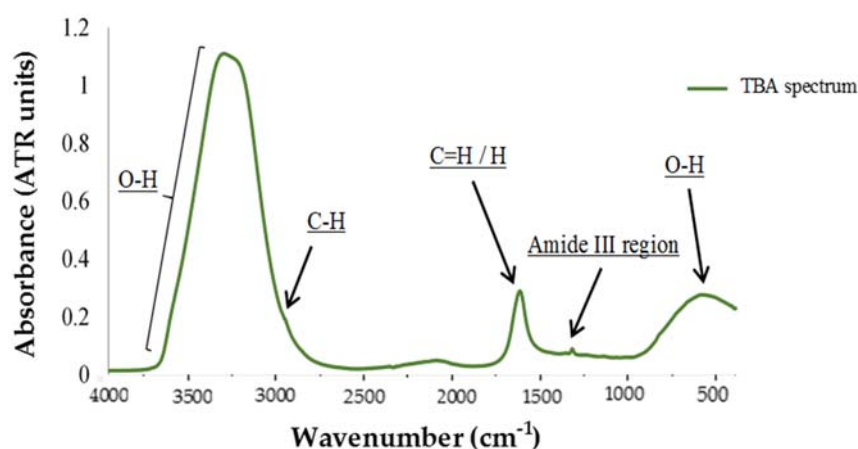


Figure 4. Example of MIR spectrum corresponding with L_OX (lipid oxidation) compounds.

3.2.2. Spectral Characteristics of Protein Oxidation Marker Compounds

Regarding MIR analysis of a carbonyl sample, two areas can be differentiated in order to perform a more detailed study (Figure 3); the Functional Group Region, between 4000 and 1500 cm^{-1} , which corresponds to hydrogen bonds atoms (C-H, O-H, and N-H) vibrational oscillations; and the Fingerprint Region (1500 – 400 cm^{-1}). Among all the absorption peaks that can be seen in the graph, the most remarkable ones are those located in the Functional Region, and more concretely between 3700 and 3100 cm^{-1} . This range presents high absorption associated to the hydroxyl groups O-H, where water appears. Usually, these absorption peaks hide the N-H associated peaks [35]. However, Figure 5 shows two clearly differentiated peaks, corresponding to Amide A group, at 3350 cm^{-1} ; and Amide B group, at 3175 cm^{-1} , which is originated from a Fermi resonance between the first overtone of Amide II and N-H stretching vibrations [25]. If we observe both graphs, there is another peak that stands out over the rest. It is found at 1650 cm^{-1} and corresponds to the Amide I band, the most intense absorption band

in proteins. This is primarily due to the stretching vibrations of the C=O (70–85%) and C-N groups (10–20%), and its frequency can be found in the range between 1600 and 1700 cm^{-1} . Next to Amide I group, another less pronounced peak appears between 1588 and 1565 cm^{-1} known as Amide II. This is a more complex region than Amide I, and derives mainly from in-plane N-H bending (40–60% of the potential energy). The rest of the potential energy arises from the C-N (18–40%) and the C-C stretching vibrations (about 10%) [36]. Finally, Amide III band can be found at the region between 1400 and 1200 cm^{-1} , and corresponds to complex bands dependent on the details of the force field, the nature of side chains and hydrogen bonding [26].

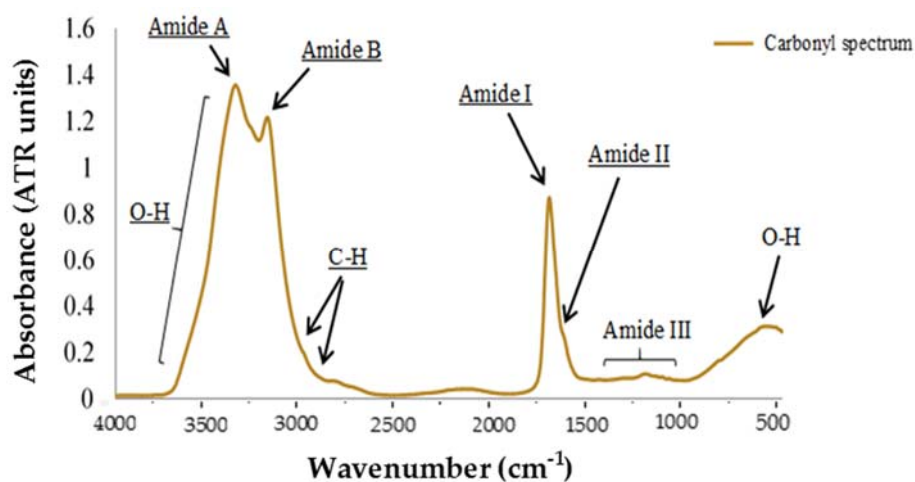


Figure 5. Results of MIR absorbance spectra from P_OX (protein oxidation) compounds.

If we observe how the weaker peaks, we find moderate absorbance at 3000 cm^{-1} , associated to the C-H bonds different vibrational oscillations. The highest peak among them is the one located at 2980 cm^{-1} and corresponds to the asymmetrical stretching vibrations of Alkanes, which could represent the fatty acids backbone (carbon atom basis of fatty acids), for both methyl ($-\text{CH}_3$) and methylene ($-\text{CH}_2$) groups. Finally, a wide band with large absorption is observed in the region between 900 and 400 cm^{-1} , which again corresponds to hydroxyl groups O-H of water, and thus they do not give any substantial structural information [24].

3.3. Multivariate Analysis and Data Processing

In this section, the validation and calibration models for both protein and lipid oxidation results, for the two kinds of samples studied, raw meat, and marker compounds, were performed. All of these results are shown in Table 3, where the two first columns correspond to TBA and carbonyl content of raw meat samples; whereas the rest of the columns correspond to L_OX and P_OX marker compounds.

Table 3. Results of the predictive models (calibration and validation), of the TBARS, carbonyls studied in raw meat and L_OX (lipid oxidation) and P_OX (protein oxidation) marker compounds.

Parameter	TBARS Raw Meat Samples	Carbonyl Raw Meat Samples	L_OX Entire Set	L_OX Mean Set	P_OX Entire Set	P_OX Mean Set	
Calibration	R ² RMSEE RPD Rank	94.99 0.136 4.47 8	75.19 0.338 2.01 10	92.74 0.262 3.71 9	41.44 0.00809 1.31 5	98.46 0.00199 8.06 8	
Validation	R ² _{cv} RMSECV RPD _{cv} Rank _{cv}	24.6 0.492 1.15 8	63.18 0.402 1.65 10	60.84 0.527 1.6 9	24.09 0.00894 1.15 5	54.24 0.00769 1.48 8	
Preprocessing Treatment	First Deriv. + Vectorial Normalization (SNV) (2559–2199 cm ⁻¹)	Second Deriv. (3998–3637; 3278–2918; 2559–478 cm ⁻¹)	SNV Normalization 3278–2918 cm ⁻¹	Linear Offset Subtraction Between 3998–3637 cm ⁻¹	MSC 1839–1478 cm ⁻¹	Min-Max Normalization 3638–3277 cm ⁻¹	Straight Line Subtraction 3278–2918; 2198–1118; 760–399 cm ⁻¹
Outliers (spectra)	6	3	13	0	5	0	0

RPD: Ratio of (standard error of) Prediction to (standard) Deviation. R²: proportion of the variance for a dependent variable that is explained by the independent variable in the regression model. RMSEE: root mean square error of estimation. RMSECV: root mean square error of cross validation.

3.3.1. Lipid Oxidation Results

As observed in Table 3, several differences can be found among the obtained results. With regard to TBA results, there are significant differences between the raw meat samples, and the ones obtained from the compounds themselves (marker compound samples), showing a calibration R^2 of 9.96% and 75.19% respectively, which means a difference of 65.23%. Regarding the validation models, there are also similar differences between both kinds of samples, showing an R^2_{cv} of 2.43% for raw samples; and 63.18% for the marker compounds samples. The rest of the studied parameters presented less consistent results in the raw meat samples than in the compound markers.

In this section, a total of 240 spectral analyses from 40 L_OX samples were employed for the model construction. The samples were extracted from a total of 19 different animals from two different groups ($n = 7$ Y-L and $n = 12$ A-C). Results of the first validation were not very consistent, as they presented a poor R^2 , and a high Root Mean Square Error of cross validation (RMSECV). Because of that, some preprocessing methods were applied to the spectral data, and the most remarkable outlier points were subtracted from the cross validation in order to obtain a stronger and more reliable result. From all the possibilities, we selected the one with minimum RMSECV and higher rank and regression point displacement (RPD) values.

The resulting validation model after the preprocessing procedures showed a R^2 of 63.14% (33.83% without preprocessing), RMSECV of 0.402 (0.685 without preprocessing), and RPD of 1.65 (1.23 without preprocessing). In order to make the validation, we employed a cross validation model with one sample exclusion. In this case, 13 outlier spectra were subtracted from the results, so a total of 227 spectral data were employed for the calibration/validation model. The studied spectral range can be divided in two different regions: the region between 3278 and 2918 cm^{-1} ; and the area between 1.839 and 759 cm^{-1} . The L_OX concentration suffered variations in a range between 0.28 and 3.58 mg/kg so, in order to homogenize the results, a new calibration/validation model for the mean of each group of six spectral measurements performed for each L_OX sample was elaborated. This way, the set of spectra was reduced from $n = 240$ to $n = 40$. Following the same procedure as previously explained, a first calibration equation was given.

The validation model after the second preprocessing procedure (Linear Offset Subtraction), showed a Coefficient of Determination of 60.84%, a RMSECV of 0.527 and a RPD of 1.6, unlike the first results of validation, which showed a poorer R^2 of 33.63%, a quite higher RMSCV of 0.686, and a lower RPD of 1.23. The type of validation employed was cross validation with one sample exclusion. In this case, no outlier spectra were subtracted, so a total of 40 spectra data were employed for calibration/validation model. Table 4 shows the calibration and validation results for both the entire and mean set of data.

Table 4. Calibration and cross validation results for entire and mean sets in the L_OX (lipid oxidation) spectra.

Parameter	L_OX Entire Set ($n = 240$)	L_OX Mean Set ($n = 40$)
Calibration	R^2	75.19
	RMSEE	0.338
	RPD	2.01
	Rank	10
Validation	R^2_{cv}	63.18
	RMSECV	0.402
	RPD_{cv}	1.65
	$Rank_{cv}$	10

As observed in Table 4, the most remarkable improvements appear in the calibration model when performing the mean of the group of spectral data. In that case, R^2 increases from 75.9% to 92.74%. The root mean square error of estimation (RMSEE) decreases from 0.338 to 0.262, and the RPD goes from 2.01 to 3.71. However, the validation model shows worse results for the mean than for the whole

set of spectra. This is directly related to the use of a noticeably smaller set of spectra (40 in comparison to 240), so differences between samples have stronger repercussions over the results.

3.3.2. Protein Oxidation Results

In the case of carbonyl content validation model results, R^2_{cv} values for raw meat showed similar results than the ones obtained through the predictive model of the entire set, with values of 24.6% and 24.09%, respectively. However, when comparing these results with those obtained with the predictive model using the mean set, a significant improvement was observed, showing a R^2_{cv} of 54.24%, which means an improvement of 29.69%. This suggests that when studying carbonyl content through MIR spectroscopy, it is preferable to perform a mean of the obtained spectra before constructing the predictive model.

In the same way as previously explained, the procedure consisted of introducing the spectral measurements into QUANT 2 software, versus their carbonyl quantitative values. A first calibration equation was given, but, in this case, the results of first validation were not consistent at all, as they presented really poor R^2 , and high RMSECV. The negative values of R^2_{cv} were due to their low value of rank (1), as the residuals were larger than the variance in true values. Again, as happened with L_OX sets of spectra, a preprocessing treatment for the spectral data was performed. In the case of carbonyls, Derivative + Multiplicative Scatter Correction (MSC) was first performed as it offered almost the minimum RMSECV with the highest rank (5). After that, outlier points were subtracted and the validation was repeated. The validation model after the preprocessing procedure showed a R^2 of 24.09%, a RMSECV of 0.00894 and a RPD of 1.15, unlike the first results of validation which showed a poorer R^2 of 3.33%, a quite higher RMSECV of 0.0116, and a lower RPD of 0.984. This time, cross validation with one sample exclusion was employed. In this case, five outlier spectra were subtracted, so a total of 103 spectra were employed for the calibration/validation. The spectral range was focused on one particular area, between 1839 and 1478 cm^{-1} , and the carbonyls concentration range was between 0.088 and 0.134 mM.

Following the same procedure as the one followed with the L_OX compound markers, calibration/validation models were set for the mean of the spectral measurements of P_OX compounds. Sample sets in this case were reduced from $n = 108$ to $n = 18$ to get better results compared to the analysis of the whole set of spectra of P_OX. As was expected, attending to the calibration results, the first validation outcomes were not consistent at all, as they presented the worst R^2 values of the whole study (-24.41%), and quite high RMSECV values. As happened in all the previous analysis, a preprocessing treatment for the spectral data was done. Min-Max Normalization was performed as it offered the minimum RMSECV with an acceptable rank (8). In this case, the validation model after the preprocessing procedure of P_OX mean spectra showed a R^2 of 54.24%, a RMSECV of 0.00769 and a RPD of 1.48. This time, cross validation with one sample exclusion validation model was chosen. In this case, no outlier spectra were subtracted, so the total spectra for calibration/validation employed were 18. The spectral range was focused between 3638 and 3277 cm^{-1} . The concentration range for Carbonyls was 0.088–0.134 mM. Calibration and validation results from the entire set of spectra are presented and compared with mean sets results in Table 5.

Table 5. Calibration and cross validation results for entire and mean sets in P_OX (protein oxidation) spectra.

		P_OX Entire Set ($n = 108$)	P_OX Mean Set ($n = 18$)
Calibration	R^2	41.44	98.46
	RMSEE	0.00809	0.00199
	RPD	1.31	8.06
	Rank	5	8
Validation	R^2_{cv}	24.09	54.24
	RMSECV	0.00894	0.00769
	RPD_{cv}	1.15	1.48
	$Rank_{cv}$	5	8

As in L_OX results, the most remarkable improvements in the results shown at Table 5 appear in the calibration model when performing the mean of each group of spectra, and comparing the results with their entire sets. Thus, R^2 ascends from 41.44% to 98.46% in P_OX, and as for RMSEE, it descends significantly from 0.00809 to 0.00199. Not only that, but RPD also shows a great increment in P_OX from 1.31 up to 8.06.

In the case of validation models, P_OX results show an improvement when performing means compared to the ones obtained with the whole set of spectra. R^2_{cv} value in the entire set increases from 24.09 to 54.24 when employing the mean spectra set. Here, the most important factor is the rank chosen. When performing preprocessing methods in the entire set of P_OX, a very low rank was chosen, something that might have affected these results. However, in the P_OX mean set, a higher rank was obtained and this could have helped to obtain more consistent results of R^2_{cv} , RPD_{cv} and RMSECV.

3.3.3. Raw Meat vs. Marker Compounds Quantitative Analysis Results

In this section, we discuss the results achieved for both type of samples, oxidation marker compounds (L_OX and P_OX), and the ones obtained in the quantitative analysis of the spectra analyzed directly from raw meat [22].

As an approach to this comparison, some spectra are presented in Figure 6, showing L_OX and P_OX responses of some of the randomly selected samples compared to their correspondent raw meat MIR spectra. Moreover, a quantitative comparison of both groups of spectra is shown in Table 6.

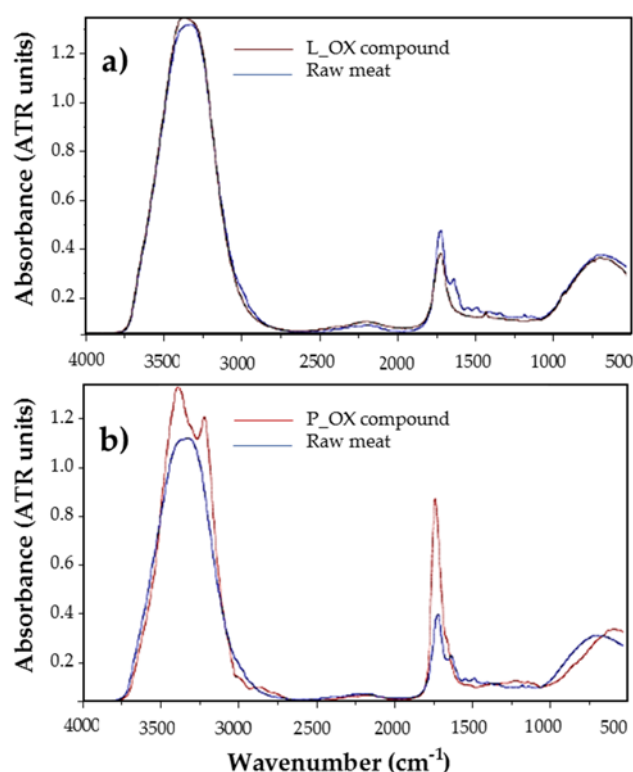


Figure 6. Comparison of marker compounds spectra vs. its raw meat samples: (a) L_OX (lipid oxidation) compound (brown) vs. raw meat animal (blue) (b) P_OX (protein oxidation) compound (red) vs. raw meat animal (blue).

Table 6. Results of the predictive models (calibration and validation), of the TBA, and carbonyls content studied in raw meat and L_OX (lipid oxidation) and P_OX (protein oxidation) markers compounds.

Parameter	Calibration				Validation				Preprocessing Treatment	Outliers (Spectra)
	R ²	RMSE	RPD	Rank	R ² _{cv}	RMSECV	RPD _{cv}	Rank _{cv}		
TBA Raw Meat Samples	9.96	0.143	1.05	1	2.43	0.146	1.01	1	First Deriv. + Vectorial Normalization (SNV) (2559–2199 cm ⁻¹)	6
Carbonyl Raw Meat Samples	94.99	0.136	4.47	8	24.6	0.492	1.15	8	Second Deriv. (3998–3637; 3278–2918; 2559–478 cm ⁻¹)	3
L_OX Entire Set	75.19	0.338	2.01	10	63.18	0.402	1.65	10	SNV Normalization (3278–2918 cm ⁻¹)	13
L_OX Mean Set	92.74	0.262	3.71	9	60.84	0.527	1.6	9	Linear Offset Subtraction (Between 3998–3637 cm ⁻¹)	0
P_OX Entire set	41.44	0.00809	1.31	5	24.09	0.00894	1.15	5	MSC (1839–1478 cm ⁻¹)	5
P_OX Mean Set	98.46	0.00199	8.06	8	54.24	0.00769	1.48	8	Min-Max Normalization (3638–3277 cm ⁻¹)	0

As it can be observed, only slight differences can be appreciated between L_OX and raw meat samples, with both spectra being quite similar; however, raw meat spectra present several absorption peaks in the 1.650 to 1400 cm^{-1} region that L_OX samples do not show, as can be appreciated, for example, at 1336 cm^{-1} . There, a weak absorption peak can be appreciated in L_OX spectra, which does not appear in raw meat samples, and it is related to the CH₃ symmetric deformation and CH₂ wagging group.

Regarding the protein comparison, the differences observed in the P_OX spectral response are more significant. The main difference is the appearance of a double absorption peak in the band located between 3500 and 3000 cm^{-1} (Amide A, and Amide B group), which represents the N-H bond stretching vibrations. A higher absorption peak appears around 1650 cm^{-1} , corresponding to Amide I group. This one is the most intense absorption band in proteins and is due to the stretching vibrations of the C=O (70–85%) and C-N groups (10–20%). It makes sense that these peaks present higher absorption values in the P_OX spectra than in the raw meat one, as these peaks are associated to peptide bonds. These bonds may be much more concentrated in the P_OX marker compounds than in raw meat samples, which present a much more complex tissue matrix and, hence, may interfere with the measured results.

Several differences can be found among the results observed in Table 6. Regarding L_OX extracts, very significant differences can be found between raw samples and compounds results, from calibration values of $R^2 = 9.96\%$ in raw meat to $R^2 = 75.19\%$ in L_OX entire set calibration (dif. = +65.23). Focusing on the validation models, the differences observed are of the same order, with a value of $R^2_{cv} = 2.43\%$ in the raw samples, to a value of 63.18% in the entire set of L_OX samples. In the rest of the studied parameters, the results are less consistent in raw meat samples than the ones obtained through L_OX compounds through MIR analysis. It should also be noted that the highest RPD value of the whole group of predictive models was obtained through the L_OX entire set, achieving a value of 1.65.

On the other hand, the results found of the entire set and the mean set of carbonyls are strikingly different in the case of P_OX. Concretely, in the validation models, R^2 in raw meat samples showed a very similar result to the one obtained through the predictive model of the entire set of P_OX, with values of 24.6% and 24.09%, respectively. However, when comparing it to the result obtained through the predictive model of the mean set, a significant improvement can be observed in the latter one, with a $R^2_{cv} = 54.24\%$ (diff. = +29.69). This may suggest that when studying P_OX content through MIR spectroscopy, it is preferable to perform a mean of the spectra obtained before constructing the predictive model.

4. Conclusions

The spectra showed some remarkable differences between protein and lipid oxidation marker compounds. Prediction models were promising for the usefulness of MIR technology to estimate the values of lipid and protein oxidation marker compounds from previously extracted samples or when applied directly on raw meat samples. However, marker compound results showed more consistent predictive models than the ones achieved using quantitative analysis of the spectra obtained from the raw meat. From a practical point of view, given the results, the use of regression treatments delimiting the range of the spectrum coinciding with the wavelengths in which a large number of protein and fatty acid bonds are recognized could be useful in future research. Besides, it has been proved that performing a previous extraction of the marker compounds notably helps to achieve more consistent results for lipid and protein oxidation assessment in horse meat products. Considering the potential of this technique, MIR spectroscopy arises as an interesting alternative to traditional meat composition analytical methods, which are time consuming. Regardless, more research is needed on the MIR application directly on raw meat in order to improve the estimation of the obtained predictive models.

Author Contributions: Conceptualization, M.J.B. and K.I.; methodology K.I., M.V.S., and M.B.; software, M.B.; formal analysis, M.J.B., I.J.-L. and K.I.; investigation, M.J.B., F.Z. and M.V.S.; resources, M.J.B. and M.B.; Writing—original draft preparation, I.J.-L. and F.Z.; writing—review and editing, M.V.S., M.J.B., K.I., I.J.-L. and M.B.; project administration, M.B. and K.I. All authors have read and agreed to the published version of the manuscript.

Funding: This research was funded by INIA Instituto Nacional de Investigación y Tecnología Agraria y Alimentaria, grant number RTA 2012-00090-C03-01 and by the Spanish Ministerio de Ciencia, Innovación y Universidades, Project RTI2018-094475-B-I00 (MCIU/AEI/FEDER,UE).

Acknowledgments: Authors want to acknowledge Susana García from the UPNA for her support in sampling preparation and analysis.

Conflicts of Interest: The authors declare no conflict of interest.

Appendix A

Table A1. Concentrates Composition.

Ingredients	Standard Concentrate			Linseed Concentrate		
	Ration (%)	Digestible Energy (Mcal/kg DM)	% Brute Protein/kg DM	Ration (%)	Digestible Energy (Mcal/kg DM)	% Brute Protein/kg DM
Oat flour	30.03	2.5	7.4	45.95	2.5	7.4
Barley flour	30.10	2.9	8.3	13.07	2.9	8.3
Cornmeal	15.47	3.0	6.5	14.54	3.0	6.5
Wheat Bran	7.95	2.3	13.0	5.92	2.3	13.0
Soybean meal	9.99	3.0	38.2	9.06	3.0	38.2
Glycerol	3.96	3.2		3.96	3.2	
Linseed				5.01	3.9	19.1
TOTAL	97.50 ¹	2.69	10.57	97.51 ¹	2.70	10.61

¹ 2.5 % added to the total ration addition (%) (vitamins + salt + calcium carbonate + calcium phosphate).

References

- Martuzzi, F.; Catalano, A.; Sussi, C. Characteristics of horse meat consumption and production in Italy. *Ann. Della Fac. Med. Vet.* **2001**, *21*, 213–223.
- Caballero, J. Carne de Potro, la Nueva Favorita de la Alta Gastronomía por su Alto Valor Proteico y su Poca Grasa. Available online: <http://www.expansion.com/fueradeserie/gastro/2017/07/11/595f50cee2704ef94d8b45f2.html> (accessed on 12 July 2017).
- Ministerio de Agricultura, Pesca, y Alimentación, G. de E. El Sector Equino en Cifras. Available online: https://www.mapa.gob.es/es/ganaderia/temas/produccion-y-mercados-ganaderos/indicadoreseconomicos/sectorequino2019_parapublicar_tcm30-420793.pdf (accessed on 29 October 2020).
- Sarriés, M.V.; Beriain, M.J. Carcass characteristics and meat quality of male and female foals. *Meat Sci.* **2005**, *70*, 141–152. [CrossRef]
- Lorenzo, J.M.; Sarriés, M.V.; Tateo, A.; Polidori, P.; Franco, D.; Lanza, M. Carcass characteristics, meat quality and nutritional value of horsemeat: A review. *Meat Sci.* **2014**, *96*, 1478–1488. [CrossRef]
- Lorenzo, J.M.; Pateiro, M. Influence of type of muscles on nutritional value of foal meat. *Meat Sci.* **2013**, *93*, 630–638. [CrossRef]
- Dobranic, V.; Njari, B.; Cvrtila Fleck, Z.; Kadivc, M. Chemical composition of horse meat. *First Croat. Meat J.* **2009**, *XI*, 62–67.
- Gómez, M.; Lorenzo, J.M. Effect of packaging conditions on shelf-life of fresh foal meat. *Meat Sci.* **2012**, *91*, 513–520. [CrossRef]
- Estévez, M.; Ventanas, S.; Cava, R. Oxidation lipids and proteins in frankfurthers with different fatty acid compositions and tocopherol and phenolic contents. *Food Chem.* **2007**, *100*, 55–63. [CrossRef]
- Barriuso, B.; Astiasarán, I.; Ansorena, D. A review of analytical methods measuring lipid oxidation status in foods: A challenging task. *Eur. Food Res. Technol.* **2012**, *236*, 1–15. [CrossRef]
- Pignoli, G.; Bou, R.; Rodríguez-Estrada, M.T.; Decker, E.A. Suitability of saturated aldehydes as lipid oxidation markers in washed turkey meat. *Meat Sci.* **2009**, *83*, 412–416. [CrossRef]
- Estévez, M. Protein carbonyls in meat systems: A review. *Meat Sci.* **2011**, *89*, 259–279. [CrossRef]
- Brewer, S. Irradiation effects on meat color—A review. *Meat Sci.* **2004**, *68*, 1–17. [CrossRef] [PubMed]

14. Zakrys-Waliwander, P.I.; O'Sullivan, M.G.; Allen, P.; O'Neill, E.E.; Kerry, J.P. Investigation of the effects of commercial carcass suspension (24 and 48 h) on meat quality in high oxygen modified atmosphere packed beef steaks during chill storage. *Food Res. Int.* **2010**, *43*, 277–284. [[CrossRef](#)]
15. Lund, M.N.; Heinonen, M.; Baron, C.P.; Estévez, M. Protein oxidation in muscle foods: A review. *Mol. Nutr. Food Res.* **2011**, *55*, 83–95. [[CrossRef](#)] [[PubMed](#)]
16. Allendorf, M.E. Use of FTIR for Rapid Authentication and Detection of Adulteration of Food. *Annu. Rev. Food Sci. Technol.* **2011**, *2*, 467–483.
17. Reid, L.M.; Downey, G. Recent technological advances for the determination of food authenticity. *Trends Food Sci. Technol.* **2006**, *17*, 344–353. [[CrossRef](#)]
18. Vyncke, W. Evaluation of the Direct Thiobarbituric Acid Extraction Method for Determining Oxidative Rancidity in Mackerel (*Scomber scombrus* L.). *Meat Sci.* **1975**, *77*, 239–240. [[CrossRef](#)]
19. Oliver, C.N.; Ahn, B.W.; Moerman, E.J.; Goldstein, S.; Stadtman, E.R. Age-related changes in oxidized proteins. *J. Biol. Chem.* **1987**, *262*, 5488–5491.
20. Vuorela, S.; Salminen, H.; Mäkelä, M.; Kivikari, R.; Karonen, M.; Heinonen, M. Effect of plant phenolics on protein and lipid oxidation in cooked pork meat patties. *J. Agric. Food Chem.* **2005**, *53*, 8492–8497. [[CrossRef](#)]
21. Ruiz, M.; Beriain, M.J.; Beruete, M.; Insausti, K.; Lorenzo, J.M.; Sarriés, M.V. Application of MIR Spectroscopy to the Evaluation of Chemical Composition and Quality Parameters of Foal Meat: A Preliminary Study. *Foods* **2020**, *9*, 583. [[CrossRef](#)]
22. Ruiz Darbonnens, M. Effect of Production Factors on Foal Carcass and Meat Quality: Consumers Preferences. Ph.D. Thesis, Universidad Pública de Navarra, Pamplona, Spain, 2017.
23. Dominguez, R.; Pateiro, M.; Crecente, S.; Ruiz, M.; Sarriés, M.V.; Lorenzo, J.M. Effect of Linseed Supplementation and Slaughter Age on Meat Quality of Grazing Crossbred Galician x Burguete Foals. *Sci. Food Agric.* **2018**, *98*, 266–273. [[CrossRef](#)]
24. Pretsch, E.; Bühlmann, P.; Affolter, C. *Structure Determination of Organic Compounds*; Springer: Berlin/Heidelberg, Germany, 2000; ISBN 9783540938095.
25. Jabs, A. Determination of Secondary Structure in Proteins by Fourier Transform Infrared Spectroscopy (FTIR). Available online: http://jenalib.leibniz-flf.de/ImgLibDoc/ftir/IMAGE_FTIR.html (accessed on 14 November 2020).
26. Tamm, L.K.; Tatulian, S.A. Infrared spectroscopy of proteins and peptides in lipid bilayers. *Q. Rev. Biophys.* **1997**, *30*, 365–429. [[CrossRef](#)] [[PubMed](#)]
27. Silverstein, R.M.; Bassler, G.C.; Morrill, T.C. *Spectrometric Identification of Organic Compounds*, 4th ed.; John Wiley and Sons: New York, NY, USA, 2005; ISBN 978-0-470-61637-6.
28. Kanou, M.; Nakanishi, K.; Hashimoto, A.; Kameokaj, T. Influences of monosaccharides and its glycosidic linkage on infrared spectral characteristics of disaccharides in aqueous solutions. *Appl. Spectrosc.* **2005**, *59*, 885–892. [[CrossRef](#)]
29. Karoui, R.; Downey, G.; Blecker, C. Mid-infrared spectroscopy coupled with chemometrics: A tool for the analysis of intact food systems and the exploration of their molecular structure-quality relationships—A review. *Chem. Rev.* **2010**, *110*, 6144–6168. [[CrossRef](#)]
30. Eisenberg, D.; Kauzmann, W. *The Structure and Properties of Water*; Oxford University Press: New York, NY, USA, 1969; ISBN 9780198570264.
31. Nikonenko, N.A.; Buslov, D.K.; Sushko, N.I.; Zhabankov, R.G. Spectroscopic manifestation of stretching vibrations of glycosidic linkage in polysaccharides. *J. Mol. Struct.* **2005**, *752*, 20–24. [[CrossRef](#)]
32. Sun, D.W. *Infrared Spectroscopy for Food Quality Analysis and Control*, 1st ed.; Sun, D.-W., Ed.; Elsevier Science Publishing: Amsterdam, The Netherlands, 2009; ISBN 978-0-12-374136-3.
33. Bacher, A. Infrared Spectroscopy: Theory and Examples. Available online: <http://www.chem.ucla.edu/~bacher/spectroscopy/IR1.html> (accessed on 14 November 2020).
34. Vodnar, D.C.; Pop, O.L.; Socaciu, C. Monitoring lactic acid fermentation in media containing dandelion (*Taraxacum officinale*) by FTIR spectroscopy. *Not. Bot. Horti Agrobot. Cluj-Napoca* **2012**, *40*, 65–68. [[CrossRef](#)]

35. Carbonaro, M.; Nucara, A. Secondary structure of food proteins by Fourier transform spectroscopy in the mid-infrared region. *Amino Acids* **2010**, *38*, 679–690. [[CrossRef](#)] [[PubMed](#)]
36. Venyaminov, S.Y.; Kalnin, N.N. Quantitative IR spectrophotometry of peptide compounds in water (H₂O) solutions. I. Spectral parameters of amino acid residue absorption bands. *Biopolymers* **1990**, *30*, 1243–1257. [[CrossRef](#)] [[PubMed](#)]

Publisher’s Note: MDPI stays neutral with regard to jurisdictional claims in published maps and institutional affiliations.



© 2020 by the authors. Licensee MDPI, Basel, Switzerland. This article is an open access article distributed under the terms and conditions of the Creative Commons Attribution (CC BY) license (<http://creativecommons.org/licenses/by/4.0/>).

Chapter VI: Conclusions and Future Lines

This last chapter aims to summarize the main conclusions reached in this thesis. In addition, future lines of work are proposed to continue the studies discussed in this work, as well as new lines of research in the field of sensing with metamaterials, metasurfaces, and metageometries.

6.1. Conclusions

- In this thesis several MTM-based structures working on the THz regime have been proposed, for sensing applications. For the different designs, numerical, experimental results, or both, have been presented.
- A new structure based on the metageometries paradigm, called labyrinth metasensor, and based on an absorber structure has been designed for the detection of thin-films, biological elements (fungi), and chemical elements (PAHs).
 - The labyrinth metasensor operating at ~ 136 GHz was able to detect variations of only $1.1 \times 10^{-5} \lambda_0$ in SnO_2 films even for a relatively low dielectric constant, with high values of sensitivity and FOM, and good agreement between numerical and experimental results.
 - This structure has also demonstrated the ability to experimentally discern between different health-risky PAH compounds at the same concentration but with very similar chemical structures. Moreover, the labyrinth metasensor was able to experimentally detect different concentrations of the same compound, ranging from 100 ppm to 500 ppm.
 - The great performance achieved is explained due to its intricate labyrinth design, which provokes a strong electrical coupling between adjacent metallic strips, with resonances distributed all along the device surface (metageometries).
 - Scaling to higher frequencies (0.8 – 0.9 THz), allowed us to improve the detection limit, and gave us the possibility to detect analytes of a much smaller size, fungi in our case (numerical results only).
- Starting from a very simple blade structure based on the concept of meta-atoms, we made several modifications to its geometry in order to enhance its electric field and achieve higher sensitivities, without losing the ease of its manufacture with traditional techniques.
 - Hollow designs were found to be better for sensing purposes, due to the large electric field confinement generated between metallic plates, what emphasizes the importance of the geometry design and the electric field distribution in sensing devices.
- An exhaustive study of two-dimensional structures composed of perforated annular apertures in metallic screens (SHAs), with different substrate thicknesses (50 and 75 μm), with and without a dielectric substrate has been carried out based on the study of the ET phenomenon and its possibilities in sensing applications.
 - Both ET with vertical and horizontal polarizations, this is, regular and anomalous ET regimes, were studied for thin-film sensing applications. The results showed that the anomalous ET regime, despite being the most unknown polarization in this kind of approaches, worked better in terms of sensitivity/FOM.

- The effect of depositing the analyte to be sensed on the patterned or the non-patterned side of the SHAs was studied, with different interpretations depending on the substrate thickness, which will indicate the ET regime to be excited in each case.
 - For the ET established regular regime (50 μm SHA and vertical polarization), both deposition options allowed us to detect film thicknesses ranging from 3 μm to 13 μm . Nevertheless, depositing on the patterned side offers somewhat better values in terms of sensitivity/FOM.
 - For the non-established anomalous ET regime (50 μm SHA and horizontal polarization), it was not possible to perform the typical frequency shift based sensing procedure, due to the insufficient substrate thickness to fully excite the anomalous resonance. However, an alternative for thin-film sensing based on a variation of a peak amplitude was achieved.
 - For the 75 μm SHA, the only option to perform a reliable thin-film sensing was in the case of depositing on the non-patterned side of the structure, in the anomalous regime (horizontal polarization).
- We have employed MIR spectroscopy to analyze, estimate and establish prediction models of protein and lipid oxidative processes in foal meat, in both pre-extracted oxidative marker compounds, and directly on raw meat.
 - Previously extracted compounds showed more consistent results in the prediction models rather than making the analysis directly on the raw meat.
 - Although prediction models were promising to estimate the values of protein and lipid oxidation of the samples, there is still a long way to go, and the results obtained are far behind those that can be obtained with traditional methods, despite the fact that these methods are time-consuming and expensive.

6.2. Future lines

Although the first metamaterial-based sensor appeared more than a decade ago, research in this field is still ongoing, and the scientific community is nowadays still trying to come up with ever more sensitive and effective designs. Thus, as part of the current work, new lines of work that are not covered in this thesis are open at present:

- Design and manufacture of the labyrinth metasurface at higher frequencies. We propose to design it in the 1-2 THz band to be able to detect much lower concentrations, or even smaller biological elements than those detected so far, e.g. viruses.
- The design of new structures based on the metageometry paradigm, such as designs based on fractal structures, or space-filling curves (Peano's, Hilbert's, etc.), with intricate designs that allow us to increase the distribution of the electric field over the entire surface of the metasensor unit cell.
- Study and explore new sensing mechanisms, such as the one based on Surface Enhanced Infrared Absorption Spectroscopy (SEIRA) technique.
- Employ of MIR spectroscopy techniques for the spectral characterization of PAH compounds, for the previous appearance identification in meat samples cooked with different cooking methods.

References

- [1] D. J. Griffiths, *Introduction to Electrodynamics*, 3rd ed. Prentice Hall, 1999.
- [2] H. Hertz, *Electric Waves: being researches on the propagation of electric action with finite velocity through space*. Macmillan, 1893.
- [3] J. B. Pendry, "Negative refraction makes a perfect lens," *Phys. Rev. Lett.*, vol. 85, no. 18, pp. 3966–3969, 2000.
- [4] D. Schurig *et al.*, "Metamaterial electromagnetic cloak at microwave frequencies," *Science*, vol. 314, no. 5801, pp. 977–980, 2006.
- [5] I. Newton, *Optiks*. 1704.
- [6] O. S. Heavens and R. W. Ditchburn, *Insight into optics*. Wiley, 1993.
- [7] W. Herschel, "Investigation of the Powers of the Prismatic Colours to Heat and Illuminate Objects; with Remarks, that Prove the Different Refrangibility of Radiant Heat. To which is added, an Inquiry into the Method of Viewing the Sun Advantageously, with Telescopes of," *Philos. Trans.*, vol. 90, 1800.
- [8] W. Herschel, "Experiments on the solar, and on the terrestrial rays that occasion heat; with a comparative view of the laws to which light and heat, or rather the rays which occasion them, are subject, in order to determine whether they are the same, or different," *Philos. Mag.*, vol. 90, 1800.
- [9] J. L. Miller, *Principles Of Infrared Technology A Practical Guide to the State of the Art*. Springer, 1994.
- [10] NASA, "Space Technology Mission Directorate," *Laser Communications Relay Demonstration (LCRD)*, 2021. [Online]. Available: https://www.nasa.gov/mission_pages/tm/lcrd/index.html.
- [11] J. Coates, "Interpretation of Infrared Spectra, A Practical Approach," *Encycl. Anal. Chem.*, pp. 1–23, 2006.
- [12] A. Amorim *et al.*, "Astrophysics Detection of faint stars near Sagittarius A * with GRAVITY," *Astron. Astrophys.*, vol. 127, pp. 1–10, 2021.
- [13] G. Park, M. Lee, H. Jang, and C. Kim, "Automation in Construction Thermal anomaly detection in walls via CNN-based segmentation," *Autom. Constr.*, vol. 125, p. 103627, 2021.
- [14] T. S. Alvares, G. V. De Oliveira, R. Soares, and J. M. Murias, "Near-infrared spectroscopy-derived total haemoglobin as an indicator of changes in muscle blood flow during exercise-induced hyperaemia," *J. Sports Sci.*, vol. 38, no. 7, pp. 751–758, 2020.
- [15] R. Zimroz, "applied sciences An Inspection Robot for Belt Conveyor Maintenance in Underground Mine — Infrared Thermography for Overheated Idlers Detection," *Appl. Sci.*, vol. 10, no. 14, pp. 1–17, 2020.

- [16] M. Tonouchi, "Cutting-edge terahertz technology," *Nat. Photonics*, vol. 1, no. 2, pp. 97–105, Feb. 2007.
- [17] P. H. Siegel, "Terahertz technology," *IEEE Trans. Microw. Theory Tech.*, vol. 50, no. 3, pp. 910–928, Mar. 2002.
- [18] K.-E. Peiponen, J. Axel Zeitler, and M. Kuwata-Gonokami, *Terahertz Spectroscopy and Imaging*. Springer, 2013.
- [19] I. Wilke and S. Sengupta, "Nonlinear Techniques for Terahertz Pulse Generation and Detection — Optical Rectification and Electrooptic Sampling," in *Terahertz Spectroscopy: Principles and Applications*, 2007, pp. 41–72.
- [20] L. Ho, M. Pepper, and P. Taday, "Terahertz spectroscopy: Signatures and fingerprints," *Nat. Photonics*, vol. 2, no. September, pp. 541–543, 2008.
- [21] C. Feng and C. Otani, "Terahertz spectroscopy technology as an innovative technique for food : Current state-of- the-Art research advances," *Crit. Rev. Food Sci. Nutr.*, vol. 61, no. 15, pp. 2523–2543, 2021.
- [22] J.-H. Son, *Terahertz Biomedical Science & Technology*, 1st ed. Boca Raton: CRC Press, 2014.
- [23] R. Safian, G. Ghazi, and N. Mohammadian, "Review of photomixing continuous- wave terahertz systems and current application trends in terahertz domain," *Opt. Eng.*, vol. 58, no. 11, p. 110901, 2021.
- [24] R. A. Lewis, "A review of terahertz detectors," *J. Phys. D. Appl. Phys.*, vol. 52, no. 43, 2019.
- [25] E. T. Papaioannou and R. Beigang, "THz spintronic emitters: a review on achievements and future challenges," *Nanophotonics*, vol. 10, no. 4, pp. 1243–1257, 2021.
- [26] R. You, Z. Tao, and R. Ni, "Space Applications of Terahertz Present and Potential Future," in *2018 11th UK-Europe-China Workshop on Millimeter Waves and Terahertz Technologies (UCMMT)*, 2018.
- [27] T. Kürner, D. M. Mittleman, and T. Nagatsuma, *THz Communications: Paving the Way Towards Wireless Tbps*. Springer International Publishing, 2022.
- [28] A. A. Boulogeorgos, E. Yaqub, M. Renzo, A. Alexiou, R. Desai, and R. Klinkenberg, "Machine Learning: A Catalyst for THz Wireless Networks," *Front. Commun. Networks*, vol. 2, pp. 1–34, 2021.
- [29] X. Yang, K. Yang, Y. Luo, and W. Fu, "Terahertz spectroscopy for bacterial detection: opportunities and challenges," *Appl. Microbiol. Biotechnol.*, vol. 100, no. 12, pp. 5289–5299, 2016.
- [30] S. Alfihed, J. F. Holzman, and I. G. Foulds, "Biosensors and Bioelectronics Developments in the integration and application of terahertz spectroscopy with microfluidics," *Biosens. Bioelectron.*, vol. 165, p. 112393, 2020.
- [31] Y. Huang, R. Singh, L. Xie, and Y. Ying, "Attenuated Total Reflection for Terahertz

- Modulation , Sensing , Spectroscopy and Imaging Applications ;," *Appl. Sci.*, vol. 10, no. 14, p. 4688, 2020.
- [32] L. Zanotto, R. Piccoli, J. Dong, R. Morandotti, and L. Razzari, "Single - pixel terahertz imaging : a review," *Opto-Electronic Adv.*, vol. 3, no. 9, pp. 1–15, 2020.
- [33] N. Akter and M. M. Hasan, "A Review of THz Technologies for Rapid Sensing and Detection of Viruses including SARS-CoV-2," *Biosensors*, vol. 11, no. 10, p. 349, 2021.
- [34] B. Fischer *et al.*, "Terahertz time-domain spectroscopy and imaging of artificial RNA.," *Opt. Express*, vol. 13, no. 14, pp. 5205–5215, 2005.
- [35] K. A. W. Igger, H. E. S. C. Berwein, A. K. Nja, B. Osserhoff, and P. E. H. A. B. Olívar, "Ultrasensitive THz biosensor for PCR-free cDNA detection based on frequency selective surfaces," *Biomed Opt. Express*, vol. 11, no. 1, pp. 448–460, 2020.
- [36] E. Pickwell *et al.*, "Simulating the response of terahertz radiation to basal cell carcinoma using ex vivo spectroscopy measurements.," *J. Biomed. Opt.*, vol. 10, no. 6, p. 064021, Jan. 2005.
- [37] L. Wang, "Terahertz Imaging for Breast Cancer Detection," *Sensors*, vol. 21, no. 19, p. 6465, 2021.
- [38] M. Danciu *et al.*, "Terahertz Spectroscopy and Imaging : A Cutting-Edge Method for Diagnosing Digestive Cancers," *Materials (Basel)*, vol. 19, no. 9, p. 1519, 2019.
- [39] A. I. Nikitkina *et al.*, "Terahertz radiation and the skin : a review," *J. Biomed. Opt.*, vol. 26, no. 4, p. 043005, 2021.
- [40] P. Doradla, C. Joseph, and R. H. Giles, "Terahertz endoscopic imaging for colorectal cancer detection: Current status and future perspectives," *World J. Gastrointest. Endosc.*, vol. 9, no. 8, pp. 346–358, 2017.
- [41] Y. Bin Ji *et al.*, "Terahertz otoscope and potential for diagnosing otitis media," *Biomed. Opt. Express*, vol. 7, no. 4, p. 1201, Apr. 2016.
- [42] D. Saeedkia, *Handbook of terahertz technology for imaging, sensing and communications*. WP Woodhead Publishing, 2013.
- [43] S. S. Dhillon *et al.*, "The 2017 terahertz science and technology roadmap," *J. Phys. D. Appl. Phys.*, vol. 50, no. 4, p. 043001, Feb. 2017.
- [44] H. Cheon, H.-J. Yang, and J.-H. Son, "Toward Clinical Cancer Imaging Using Terahertz Spectroscopy," *IEEE J. Sel. Top. Quantum Electron.*, vol. 23, no. 4, pp. 1–9, Jul. 2017.
- [45] M. Beruete and I. Jáuregui-López, "Terahertz Sensing Based on Metasurfaces," *Adv. Opt. Mater.*, vol. 8, no. 3, p. 1900721, Jul. 2019.
- [46] G. V. Eleftheriades and K. G. Balmain, *Negative-Refraction Metamaterials: Fundamental Principles and Applications*. Wiley-IEEE Press, 2005.
- [47] R. M. Walser, "Metamaterials: An Introduction," in *Introduction to Complex Mediums for Optics and Electromagnetics*, W. S. Weiglhofer and A. Lakhtakia, Eds. International Society of Optical Engineering, 2003, pp. 295–314.

- [48] J. C. Bose, "On the rotation of plane of polarisation of electric waves by a twisted structure," *Proc. R. Soc. London*, vol. 63, no. 389–400, pp. 146–152, 1898.
- [49] W. E. Kock, "Metal-lens antennas," *Proc. IRE*, vol. 34, no. 11, pp. 828–836, 1946.
- [50] V. G. Veselago, "The electrodynamics of substances with simultaneously negative values of ϵ and μ ," *Sov. Phys. Uspekhi*, vol. 10, no. 4, pp. 509–514, Apr. 1968.
- [51] N. Yu *et al.*, "Light Propagation with Phase Discontinuities: Generalized Laws of Reflection and Refraction," *Science*, vol. 334, pp. 333–338, 2011.
- [52] J. B. Pendry, A. J. Holden, D. J. Robbins, and W. J. Stewart, "Magnetism from Conductors and Enhanced Nonlinear Phenomena," *IEEE Trans. Microw. Theory Tech.*, vol. 47, no. 11, pp. 2075–2084, 1999.
- [53] H. O. Moser, B. D. F. Casse, O. Wilhelmi, and B. T. Saw, "Electromagnetic metamaterials over the whole THz range - achievements and perspectives," *Electromagn. Mater.*, pp. 18–25, 2005.
- [54] D. R. Smith, W. J. Padilla, D. C. Vier, S. C. Nemat-Nasser, and S. Schultz, "Composite Medium with Simultaneously Negative Permeability and Permittivity," *Phys. Rev. Lett.*, vol. 84, no. 18, pp. 4184–4187, 2000.
- [55] R. A. Shelby, D. R. Smith, and S. Schultz, "Experimental Verification of a Negative Index of Refraction," *Science*, vol. 292, no. 5514, pp. 77–80, 2001.
- [56] X. Zhang and Z. Liu, "Superlenses to overcome the diffraction limit," *Nat. Mater.*, vol. 7, pp. 435–441, 2008.
- [57] J. B. Pendry, D. Schurig, and D. R. Smith, "Controlling electromagnetic fields," *Science*, vol. 312, no. 5781, pp. 1780–1782, Jun. 2006.
- [58] D. Schurig *et al.*, "Metamaterial electromagnetic cloak at microwave frequencies," *Science*, vol. 314, no. 5801, pp. 977–80, Nov. 2006.
- [59] M. Gharghi *et al.*, "A carpet cloak for visible light," *Nano Lett.*, vol. 11, no. 7, pp. 2825–2828, 2011.
- [60] B. Orazbayev, N. M. Estakhri, M. Beruete, and A. Al, "Terahertz carpet cloak based on a ring resonator metasurface," vol. 195444, pp. 1–5, 2015.
- [61] B. Orazbayev, N. Mohammadi Estakhri, A. Alù, and M. Beruete, "Experimental Demonstration of Metasurface-Based Ultrathin Carpet Cloaks for Millimeter Waves," *Adv. Opt. Mater.*, vol. 5, no. 1, p. 1600606, Jan. 2017.
- [62] N. Yu and F. Capasso, "Flat optics with designer metasurfaces," *Nat. Mater.*, vol. 13, no. 2, pp. 139–150, 2014.
- [63] I. Kim *et al.*, "Holographic metasurface gas sensors for instantaneous visual alarms," *Sci. Adv.*, vol. 7, no. 15, 2021.
- [64] C. Zhang, C. Long, S. Yin, R. Guo, and B. Han, "Graphene-based anisotropic polarization meta-filte," *Mater. Des.*, vol. 206, p. 109768, 2021.

- [65] S. D. Rezaei *et al.*, “Nanophotonic Structural Colors,” *ACS Photonics*, vol. 8, no. 1, pp. 18–33, 2021.
- [66] F. Falcone *et al.*, “Babinet Principle Applied to the Design of Metasurfaces and Metamaterials,” *Phys. Rev. Lett.*, vol. 93, no. 19, p. 197401, Nov. 2004.
- [67] M. Aznabet *et al.*, “Polypropylene-substrate-based SRR- And CSRR-metasurfaces for submillimeter waves,” *Opt. Express*, vol. 16, no. 22, pp. 18312–18319, 2008.
- [68] V. Pacheco-Peña and N. Engheta, “Antireflection temporal coatings,” *Optica*, vol. 7, no. 4, pp. 323–331, 2020.
- [69] K. Cheng, Y. Fan, W. Zhang, Y. Gong, S. Fei, and H. Li, “Optical Realization of Wave-Based Analog Computing with Metamaterials,” *Appl. Sci.*, vol. 11, no. 1, p. 141, 2021.
- [70] V. Pacheco-peña and N. Engheta, “Temporal aiming,” *Light Sci. Appl.*, vol. 9, no. 129, pp. 1–12, 2020.
- [71] J. He, X. He, T. Dong, S. Wang, M. Fu, and Y. Zhang, “Recent progress and applications of terahertz metamaterials,” *J. Phys. D. Appl. Phys.*, vol. 55, p. 123002, 2022.
- [72] B. Zhang *et al.*, “Tunable multi-band terahertz absorber based on composite graphene structures with square ring and Jerusalem cross,” *Results Phys.*, vol. 25, p. 104233, 2021.
- [73] H. Mohammadi, N. Abad, E. Zareian, and J. Raheleh, “Design of Metasurface - Based Multi - layer THz Filters Utilizing Optimization Algorithm with Distinct Fitness Function Definitions,” *Plasmonics*, vol. 16, pp. 1865–1876, 2021.
- [74] B. Li *et al.*, “Polarization Multiplexing Terahertz Metasurfaces through Spatial Femtosecond Laser-Shaping Fabrication,” *Adv. Opt. Mater.*, vol. 8, p. 2000136, 2020.
- [75] A. Moreno-Peñarrubia, S. A. Kuznetsov, and M. Beruete, “Ultrathin Subterahertz Half-Wave Plate With High Conversion Efficiency Based on Zigzag Metasurface,” *IEEE Trans. Antennas Propag.*, vol. 68, no. 11, pp. 7700–7704, 2020.
- [76] Q. Li *et al.*, “Gate-tuned graphene meta-devices for dynamically controlling terahertz wavefronts,” *Nanophotonics*, vol. 11, no. 9, pp. 2085–2096, 2022.
- [77] J. F. O’Hara, W. Withayachumnankul, and I. Al-Naib, “A Review on Thin-film Sensing with Terahertz Waves,” *J. Infrared, Millimeter, Terahertz Waves*, vol. 33, no. 3, pp. 245–291, Mar. 2012.
- [78] T. Driscoll *et al.*, “Tuned permeability in terahertz split-ring resonators for devices and sensors,” *Appl. Phys. Lett.*, vol. 91, no. 6, pp. 3–5, 2007.
- [79] R. Marqués, F. Martín, and M. Sorolla, *Metamaterials with Negative Parameters: Theory, Design and Microwave Applications*. John Wiley & Sons, 2008.
- [80] C. Debus and P. H. Bolivar, “Frequency selective surfaces for high sensitivity terahertz sensing,” *Appl. Phys. Lett.*, vol. 91, no. 18, pp. 2005–2008, 2007.
- [81] J. F. O’Hara *et al.*, “Thin-film sensing with planar terahertz metamaterials: sensitivity and limitations,” *Opt. Express*, vol. 16, no. 3, pp. 1786–1795, 2008.

- [82] I. Jáuregui-López, P. Rodríguez-Ulibarri, A. Urrutia, S. A. Kuznetsov, and M. Beruete, "Labyrinth Metasurface Absorber for Ultra-High-Sensitivity Terahertz Thin Film Sensing," *Phys. status solidi - Rapid Res. Lett.*, vol. 12, no. 10, p. 1800375, Oct. 2018.
- [83] H. Tao *et al.*, "Performance enhancement of terahertz metamaterials on ultrathin substrates for sensing applications," *Appl. Phys. Lett.*, vol. 97, no. 26, p. 261909, 2010.
- [84] W. Withayachumnankul *et al.*, "Sub-diffraction thin-film sensing with planar terahertz metamaterials," *Opt. Express*, vol. 20, no. 3, pp. 3345–3352, 2012.
- [85] L. Cong, S. Tan, R. Yahiaoui, F. Yan, W. Zhang, and R. Singh, "Experimental demonstration of ultrasensitive sensing with terahertz metamaterial absorbers: A comparison with the metasurfaces," *Appl. Phys. Lett.*, vol. 106, no. 3, p. 031107, Jan. 2015.
- [86] R. Yahiaoui, S. Tan, L. Cong, R. Singh, F. Yan, and W. Zhang, "Multispectral terahertz sensing with highly flexible ultrathin metamaterial absorber," *J. Appl. Phys.*, vol. 118, no. 8, p. 083103, Aug. 2015.
- [87] H. Zhang, Y. Cheng, and F. Chen, "Optik Quad-band plasmonic perfect absorber using all-metal nanostructure metasurface for refractive index sensing," *Optik (Stuttg.)*, vol. 229, p. 166300, 2021.
- [88] Y. Cheng and F. Chen, "Triple-Band Perfect Light Absorber Based on Hybrid Metasurface for Sensing Application," *Nanoscale Res. Lett. Vol.*, vol. 15, no. 1, 2020.
- [89] S. H. Badri, M. M. Gilarlue, S. SaeidNahaei, and J. S. Kim, "Narrowband-to-broadband switchable and polarization-insensitive terahertz metasurface absorber enabled by phase-change material," *J. Opt.*, vol. 24, no. 2, p. 025101, 2022.
- [90] R. Singh, W. Cao, I. Al-Naib, L. Cong, W. Withayachumnankul, and W. Zhang, "Ultrasensitive THz sensing with high-Q Fano resonances in metasurfaces," *Appl. Phys. Lett.*, vol. 171101, no. 2014, p. 5, 2014.
- [91] P. Rodríguez-ulibarri, S. A. Kuznetsov, and M. Beruete, "Wide angle terahertz sensing with a cross-dipole frequency selective surface," *Appl. Phys. Lett.*, vol. 108, no. 11, p. 111104, 2016.
- [92] M. Gupta, Y. K. Srivastava, M. Manjappa, and R. Singh, "Sensing with toroidal metamaterial," *Appl. Phys. Lett.*, vol. 110, no. 12, p. 121108, 2017.
- [93] H. Im, K. C. Bantz, N. C. Lindquist, C. L. Haynes, and S. H. Oh, "Vertically oriented sub-10-nm plasmonic nanogap arrays," *Nano Lett.*, vol. 10, no. 6, pp. 2231–2236, 2010.
- [94] X. Chen *et al.*, "Atomic layer lithography of wafer-scale nanogap arrays for extreme confinement of electromagnetic waves," *Nat. Commun.*, vol. 4, no. May, pp. 1–7, 2013.
- [95] H. R. Park, X. Chen, N. C. Nguyen, J. Peraire, and S. H. Oh, "Nanogap-enhanced terahertz sensing of 1 nm thick ($\lambda/106$) dielectric films," *ACS Photonics*, vol. 2, no. 3, pp. 417–424, 2015.
- [96] N. C. Lindquist *et al.*, "Flat metallic surface gratings with sub-10nm gaps controlled by atomic-layer deposition," *Nanotechnology*, vol. 27, no. 37, pp. 1–6, 2016.

- [97] T. Nam and H. Kim, "Atomic layer deposition for nonconventional nanomaterials and their applications," *J. Mater. Res.*, vol. 35, no. 7, pp. 656–680, 2019.
- [98] J. Li *et al.*, "Atomic Layer Etching of SiGe for Manufacturing Vertical Nanowire Array with Diameter Less than 20 nm," *Materials (Basel)*, vol. 13, no. 3, pp. 1–11, 2020.
- [99] D. Yoo *et al.*, "Plasmonic Split-Trench Resonator for Trapping and Sensing," *ACS Nano*, vol. 15, no. 4, pp. 6669–6677, 2021.
- [100] M. V Kruchinina *et al.*, "Investigation of red blood cells from patients with diffuse liver diseases by combined dielectrophoresis and terahertz spectroscopy method," *Opt. Eng.*, vol. 60, no. 8, pp. 1–10, 2020.
- [101] A. A. Lykina *et al.*, "Terahertz spectroscopy of diabetic and non-diabetic human blood plasma pellets," *J. Biomed. Opt.*, vol. 26, no. 4, p. 043006, 2022.
- [102] V. Vaks *et al.*, "Analysis of the Thermal Decomposition Products of Pathological and Healthy Tissues in Paranasal Sinuses: A High-Resolution Terahertz Gas Spectroscopy Study," *Appl. Sci.*, vol. 11, no. 16, p. 7562, 2021.
- [103] B. Li, D. Zhang, and Y. Shen, "Study on terahertz spectrum analysis and recognition modeling of common agricultural diseases," *Spectrochim. Acta Part A Mol. Biomol. Spectrosc.*, vol. 243, p. 118820, 2020.
- [104] A. Ahmadvand, B. Gerislioglu, Z. Ramezani, A. Kaushik, P. Manickam, and S. A. Ghoreishi, "Functionalized terahertz plasmonic metasensors: Femtomolar-level detection of SARS-CoV-2 spike proteins," *Biosens. Bioelectron.*, vol. 177, p. 112971, 2021.
- [105] L. Xie, W. Gao, J. Shu, Y. Ying, and J. Kono, "Extraordinary sensitivity enhancement by metasurfaces in terahertz detection of antibiotics," *Sci. Rep.*, vol. 5, p. 8671, 2015.
- [106] G. Wang, F. Zhu, T. Lang, J. Liu, Z. Hong, and J. Qin, "All - metal terahertz metamaterial biosensor for protein detection," *Nanoscale Res. Lett.*, vol. 16, no. 1, 2021.
- [107] R. Zhou *et al.*, "Label-free terahertz microfluidic biosensor for sensitive DNA detection using graphene-metasurface hybrid structures," *Biosens. Bioelectron.*, vol. 188, p. 113336, 2021.
- [108] M. I. T. Ang *et al.*, "Detection of single-base mutation of DNA oligonucleotides with different lengths by terahertz attenuated total reflection microfluidic cell," *Biomed. Opt. Express*, vol. 11, no. 9, pp. 5362–5372, 2020.
- [109] K. Yang *et al.*, "A terahertz metamaterial biosensor for sensitive detection of microRNAs based on gold-nanoparticles and strand displacement amplification," *Biosens. Bioelectron.*, vol. 175, p. 112874, 2021.
- [110] E. Pickwell and V. P. Wallace, "Biomedical applications of terahertz technology," *J. Phys. D. Appl. Phys.*, vol. 39, no. 17, pp. R301–R310, 2006.
- [111] D. Li *et al.*, "Detecting melanoma with a terahertz spectroscopy imaging technique," *Spectrochim. Acta Part A Mol. Biomol. Spectrosc.*, vol. 234, p. 118229, 2020.
- [112] J. Zhang, N. Mu, L. Liu, J. Xie, H. Feng, and J. Yao, "Highly sensitive detection of

- malignant glioma cells using metamaterial-inspired THz biosensor based on electromagnetically induced transparency," *Biosens. Bioelectron.*, vol. 185, p. 113241, 2021.
- [113] W. Shi, Y. Wang, L. Hou, C. Ma, and L. Yang, "Detection of living cervical cancer cells by transient terahertz spectroscopy," *J. Bioph.*, vol. 14, no. 1, pp. 1–7, 2021.
- [114] M. Di Fabrizio, S. Lupi, and A. D'Arco, "Virus recognition with terahertz radiation : drawbacks and potentialities OPEN ACCESS Virus recognition with terahertz radiation : drawbacks and potentialities," *J. Phys. Photonics*, vol. 3, no. 3, p. 032001, 2021.
- [115] S. J. Park *et al.*, "Detection of microorganisms using terahertz metamaterials," *Sci. Rep.*, vol. 4, p. 4988, 2014.
- [116] S. A. Yoon *et al.*, "Identifying different types of microorganisms with terahertz spectroscopy," *Biomed. Opt. Express*, vol. 11, no. 1, pp. 406–416, 2020.
- [117] F. V. Di Girolamo *et al.*, "Detection of fungal infections in chestnuts : a terahertz imaging-based approach," *Food Control*, vol. 123, p. 107700, 2021.
- [118] K. Yang, W. Yu, G. Huang, J. Zhou, X. Yang, and W. Fu, "Highly sensitive detection of Staphylococcus aureus by a THz metamaterial biosensor based on gold nanoparticles and rolling circle amplification †," *RSC Adv.*, vol. 10, no. 45, pp. 26824–26833, 2020.
- [119] X. Guo, "Surface plasmon resonance based biosensor technique: A review," *J. Biophotonics*, vol. 5, no. 7, pp. 483–501, 2012.
- [120] L. Sun *et al.*, "Implantable , Degradable , Therapeutic Terahertz Metamaterial Devices," vol. 2000294, pp. 1–8, 2020.
- [121] S. J. Park, S. H. Cha, G. A. Shin, and Y. H. Ahn, "Sensing viruses using terahertz nanogap metamaterials," *Biomed. Opt. Express*, vol. 8, no. 8, p. 3551, 2017.
- [122] A. G. Brolo, R. Gordon, B. Leathem, and K. L. Kavanagh, "Surface plasmon sensor based on the enhanced light transmission through arrays of nanoholes in gold films," *Langmuir*, vol. 20, no. 12, pp. 4813–4815, 2004.
- [123] H. Yoshida *et al.*, "Terahertz sensing method for protein detection using a thin metallic mesh," *Appl. Phys. Lett.*, vol. 91, no. 25, pp. 1–4, 2007.
- [124] X. Wu *et al.*, "Alkanethiol-functionalized terahertz metamaterial as label-free, highly-sensitive and specific biosensor.," *Biosens. Bioelectron.*, vol. 42, pp. 626–31, Apr. 2013.
- [125] D.-K. Lee *et al.*, "Highly sensitive and selective sugar detection by terahertz nano-antennas," *Sci. Rep.*, vol. 5, p. 15459, Oct. 2015.
- [126] L. Sun, C. Gu, T. H. Tao, and Z. Zhou, "A Degradable Antibacterial Skin patch of Flexible Terahertz Metamaterials made from Silk Proteins," in *IEEE MEMS*, 2020, pp. 2020–2022.
- [127] W. Shi, F. Fan, Z. Zhang, T. Zhang, S. Li, and X. Wang, "applied sciences Terahertz Sensing for R / S Chiral Ibuprofen via All-Dielectric Metasurface with Higher-Order

- Resonance," *Appl. Sci.*, vol. 11, no. 19, p. 8892, 2021.
- [128] B. Li, J. Bai, and S. Zhang, "Molecular and Biomolecular Spectroscopy Low concentration noroxin detection using terahertz spectroscopy combined with metamaterial," *Spectrochim. Acta Part A Mol. Biomol. Spectrosc.*, vol. 247, p. 119101, 2021.
- [129] M. Brucherseifer, M. Nagel, P. Haring Bolivar, H. Kurz, A. Bosserhoff, and R. Büttner, "Label-free probing of the binding state of DNA by time-domain terahertz sensing," *Appl. Phys. Lett.*, vol. 77, no. 24, pp. 4049–4051, 2000.
- [130] Y. Yang and D. Xu, "High-sensitivity and label-free identification of a transgenic genome using a terahertz meta-biosensor," *Opt. Express*, vol. 26, no. 24, pp. 31589–31598, 2018.
- [131] J. T. Hong *et al.*, "Enhanced sensitivity in THz plasmonic sensors with silver nanowires," *Sci. Rep.*, vol. 8, no. 1, pp. 1–8, 2018.
- [132] A. Kovacevic, M. Potrebic, and D. Tomic, "Sensitivity Characterization of Multi-Band THz Metamaterial Sensor for Possible Virus Detection," *Electronics*, vol. 11, no. 5, p. 699, 2022.
- [133] M. Muntasir, F. Sadik, and F. Islam, "Sensing and Bio-Sensing Research A review on plasmonic and metamaterial based biosensing platforms for virus detection," *Sens. Bio-Sensing Res.*, vol. 33, no. May, p. 100429, 2021.
- [134] D. L. Shriner, D. K. McCoy, D. J. Goldberg, and R. F. Wagner, "Mohs Micrographic Surgery," *J. Am. Acad. Dermatol.*, vol. 39, no. 1, pp. 79–97, 1998.
- [135] N. Lassau *et al.*, "Value of high-frequency US for preoperative assessment of skin tumors," *RadioGraphics*, vol. 17, no. 6, pp. 1559–1565, 2013.
- [136] H. K. Song, F. W. Wehrli, and J. Ma, "In vivo MR microscopy of the human skin," *Magn. Reson. Med.*, vol. 37, no. 2, pp. 185–191, 1997.
- [137] M. Huzaira, F. Rius, M. Rajadhyaksha, R. R. Anderson, and S. González, "Topographic variations in normal skin, as viewed by in vivo reflectance confocal microscopy," *J. Invest. Dermatol.*, vol. 116, no. 6, pp. 846–852, 2001.
- [138] R. M. Woodward, V. P. Wallace, D. D. Arnone, E. H. Linfield, and M. Pepper, "Terahertz pulsed imaging of skin cancer in the time and frequency domain," *J. Biol. Phys.*, vol. 29, no. 2/3, pp. 257–261, 2003.
- [139] E. Pickwell, B. E. Cole, A. J. Fitzgerald, M. Pepper, and V. P. Wallace, "In vivo study of human skin using pulsed terahertz radiation," *Phys. Med. Biol.*, vol. 49, no. 9, pp. 1595–1607, 2004.
- [140] C. Zhang *et al.*, "Label-free measurements on cell apoptosis using a terahertz metamaterial-based biosensor," *Appl. Phys. Lett.*, vol. 108, no. 24, p. 241105, Jun. 2016.
- [141] J. L. Domingo and M. Nadal, "Human dietary exposure to polycyclic aromatic hydrocarbons : A review of the scientific literature," *Food Chem. Toxicol.*, vol. 86, pp. 144–153, 2015.

- [142] L. Singh, J. G. Varshney, and T. Agarwal, "Polycyclic aromatic hydrocarbons ' formation and occurrence in processed food," *FOOD Chem.*, vol. 199, pp. 768–781, 2016.
- [143] G. R. Sampaio *et al.*, "Polycyclic aromatic hydrocarbons in foods: Biological effects, legislation, occurrence, analytical methods, and strategies to reduce their formation," *Int. J. Mol. Sci.*, vol. 22, no. 11, 2021.
- [144] H. Kim, J. Cho, D. Kim, T. S. Park, and S. K. Jin, "Effects of Gochujang (Korean Red Pepper Paste) Marinade on Polycyclic Aromatic Hydrocarbon Formation in Charcoal-Grilled Pork Belly," vol. 41, no. 3, 2021.
- [145] S. Sahin, H. I. Ulusoy, S. Alemdar, S. Erdogan, and S. Agaoglu, "The presence of polycyclic aromatic hydrocarbons (pahs) in grilled beef, chicken and fish by considering dietary exposure and risk assessment," *Food Sci. Anim. Resour.*, vol. 40, no. 5, pp. 675–688, 2020.
- [146] O. Herbert *et al.*, "Insight about methods used for polycyclic aromatic hydrocarbons reduction in smoked or grilled fishery and meat products for future re-engineering : A systematic review," *Food Chem. Toxicol.*, vol. 141, no. February, p. 111372, 2020.
- [147] European Commission, "Opinion of the Scientific Committee on Food on the risks to human health of Polycyclic Aromatic Hydrocarbons in food," 2002.
- [148] T. E. Commission, "Regulation (EC) No 1881/2006 as regards maximum levels for polycyclic aromatic hydrocarbons in foodstuffs," *Off. J. Eur. Union*, no. 835, pp. 4–8, 2011.
- [149] CCME, *Canadian Soil Quality Guidelines for Carcinogenic and Other Polycyclic Aromatic Hydrocarbons (Environmental and Human Health Effects). Scientific Criteria Document (revised)*. 2010.
- [150] Y. Zhang, X. Chen, and Y. Zhang, "Analytical chemistry , formation , mitigation , and risk assessment of polycyclic aromatic hydrocarbons : From food processing to in vivo metabolic transformation," *Compr. Rev. Food Sci. Food Saf.*, vol. 20, pp. 1422–1456, 2021.
- [151] E. Oz, "The presence of polycyclic aromatic hydrocarbons and heterocyclic aromatic amines in barbecued meatballs formulated with different animal fats," *Food Chem.*, vol. 352, p. 129378, 2021.
- [152] IARC, *Some Non-heterocyclic Polycyclic Aromatic Hydrocarbons and Some Related Exposures*, vol. 92. 2010.
- [153] World Health Organization, "Polynuclear aromatic hydrocarbons in Drinking-water," 2003.
- [154] K. Kim, S. Ara, E. Kabir, and R. J. C. Brown, "A review of airborne polycyclic aromatic hydrocarbons (PAHs) and their human health effects," *Environ. Int.*, vol. 60, pp. 71–80, 2013.
- [155] I. Mafra, J. S. Amaral, and M. B. P. P. Oliveira, "Polycyclic Aromatic Hydrocarbons (PAH) in Olive Oils and Other Vegetable Oils ; Potential for Carcinogenesis," in *Olives and Olive Oil in Health and Disease Prevention*, Amsterdam: Elsevier, 2010, pp. 489–

- 498.
- [156] J. Cheng, X. Zhang, Y. Ma, J. Zhao, and Z. Tang, "Science of the Total Environment Concentrations and distributions of polycyclic aromatic hydrocarbon in vegetables and animal-based foods before and after grilling : Implication for human exposure," *Sci. Total Environ.*, vol. 690, pp. 965–972, 2019.
- [157] I. Vintilă, *Typical Traditional Processes : Cooking and Frying*. Elsevier Inc., 2016.
- [158] C. Wang *et al.*, "Phenolic compounds in beer inhibit formation of polycyclic aromatic hydrocarbons from charcoal-grilled chicken wings," *Food Chem.*, vol. 294, no. October 2018, pp. 578–586, 2019.
- [159] M. Rose *et al.*, "Investigation into the formation of PAHs in foods prepared in the home to determine the effects of frying, grilling, barbecuing, toasting and roasting," *Food Chem. Toxicol.*, vol. 78, pp. 1–9, 2015.
- [160] D. Kafouris, A. Koukkidou, E. Christou, M. Hadjigeorgiou, and S. Yiannopoulos, "Determination of polycyclic aromatic hydrocarbons in traditionally smoked meat products and charcoal grilled meat in Cyprus," *Meat Sci.*, vol. 164, p. 108088, 2020.
- [161] M. Mirzazadeh, "Comparison of the effects of microwave cooking by two conventional cooking methods on the concentrations of polycyclic aromatic hydrocarbons and volatile N- - nitrosamines in beef cocktail smokies (smoked sausages)," *J. Food Process. Preserv.*, pp. 1–12, 2021.
- [162] C. Of *et al.*, "Code of Practice for the Reduction of Contamination of Food with Polycyclic Aromatic Hydrocarbons (PAH) from Smoking and Direct Drying Processes," in *Prevention and Reduction of Food and Feed Contamination*, 2009, pp. 1–16.
- [163] Ö. Kılıç Büyükkurt, E. Aykın Dinçer, İ. Burak Çam, C. Candal, and M. Erbaş, "The Influence of Cooking Methods and Some Marinades on Polycyclic Aromatic Hydrocarbon Formation in Beef Meat," *Polycycl. Aromat. Compd.*, vol. 40, no. 2, pp. 195–205, 2020.
- [164] W. Wongmaneepratip and K. Vangnai, "Effects of oil types and pH on carcinogenic polycyclic aromatic hydrocarbons (PAHs) in grilled chicken," *Food Control*, vol. 79, pp. 119–125, 2017.
- [165] I. Ali, A. Khan, Y. Zou, Z. Zongshuai, W. Xu, and D. Wang, "Heterocyclic amines in cooked meat products , shortcomings during evaluation , factors influencing formation , risk assessment and mitigation strategies," *Meat Sci.*, vol. 184, no. October 2021, p. 108693, 2022.
- [166] A. Khalil, M. Albachir, and A. Odeh, "Effect of Gamma Irradiation on Some Carcinogenic Grains Effect of Gamma Irradiation on Some Carcinogenic Polycyclic Aromatic Hydrocarbons (PAHs) in Wheat Grains," *Polycycl. Aromat. Compd.*, vol. 36, no. 5, pp. 873–883, 2016.
- [167] A. Khalil and M. A. L. Bachir, "Decontamination of polycyclic aromatic hydrocarbons in pea seeds by gamma irradiation," *J. Food Meas. Charact.*, vol. 11, no. 3, pp. 1167–1173, 2017.

- [168] A. Rosinska Czestochowa, "The influence of UV irradiation on PAHs in wastewater," *J. Environ. Manage.*, vol. 293, 2021.
- [169] K. Kuźmicz and A. Ciemniak, "Assessing contamination of smoked sprats (*Sprattus sprattus*) with polycyclic aromatic hydrocarbons (PAHs) and changes in its level during storage in various types of packaging types of packaging," *J. Environ. Sci. Heal.*, vol. 53, no. 1, 2018.
- [170] A. Ciemniak and K. Ku, "Effect of a packaging material type on PAHs contents in oils and water," *J. Stored Prod. Res.*, vol. 92, 2021.
- [171] D. O. Sparkman, Z. Penton, and F. Kitson, *Gas Chromatography and Mass Spectrometry: A Practical Guide*. Elsevier, 2011.
- [172] D. A. Skoog, S. R. Crouch, F. J. Holler, and M. B. Anzures, *Principles of Instrumental Analysis*, 7th editio. 2008.
- [173] International Standarization Organization, "ISO 15302:2007(en) Animal and vegetable fats and oils — Determination of benzo[a]pyrene — Reverse-phase high performance liquid chromatography method," 2007.
- [174] International Standarization Organization, "ISO 22959:2009 Animal and vegetable fats and oils — Determination of polycyclic aromatic hydrocarbons by on-line donor-acceptor complex chromatography and HPLC with fluorescence detection," 2009.
- [175] International Standarization Organization, "ISO 15753:2016 Animal and vegetable fats and oils — Determination of polycyclic aromatic hydrocarbons," 2016. .
- [176] T. W. Ebbesen, H. J. Lezec, H. F. Ghaemi, T. Thio, and P. A. Wolff, "Extraordinary optical transmission through sub-wavelength hole arrays," *Nature*, vol. 391, pp. 667–669, Feb. 1998.
- [177] L. Martín-Moreno *et al.*, "Theory of Extraordinary Optical Transmission through Subwavelength Hole Arrays," *Phys. Rev. Lett.*, vol. 86, no. 6, pp. 1114–1117, Feb. 2001.
- [178] M. Beruete *et al.*, "Enhanced millimeter-wave transmission through subwavelength hole arrays," *Opt. Lett.*, vol. 29, no. 21, pp. 2500–2502, Nov. 2004.
- [179] M. Beruete, I. Campillo, M. Navarro-cía, F. Falcone, and M. Sorolla Ayza, "Molding Left- or Right-Handed Metamaterials by Stacked Cutoff Metallic Hole Arrays," *IEEE Trans. Antennas Propag.*, vol. 55, no. 6, pp. 1514–1521, 2007.
- [180] M. Navarro-Cía, V. Pacheco-Peña, S. A. Kuznetsov, and M. Beruete, "Extraordinary THz Transmission with a Small Beam Spot: The Leaky Wave Mechanism," *Adv. Opt. Mater.*, vol. 6, no. 8, p. 1701312, Apr. 2018.
- [181] F. Miyamaru, S. Hayashi, C. Otani, and K. Kawase, "Terahertz surface-wave resonant sensor with a metal hole array," vol. 31, no. 8, pp. 1118–1120, 2006.
- [182] F. Miyamaru, Y. Sasagawa, and M. W. Takeda, "Effect of dielectric thin films on reflection properties of metal hole arrays," *Appl. Phys. Lett.*, vol. 96, no. 2, p. 021106, Jan. 2010.
- [183] R. Yahiaoui, A. C. Strikwerda, and P. U. Jepsen, "Terahertz plasmonic structure with

- enhanced sensing capabilities," *IEEE Sens. J.*, vol. 16, no. 8, pp. 2484–2488, 2016.
- [184] M. Beruete, M. Sorolla, M. Navarro-Cía, F. Falcone, I. Campillo, and V. Lomakin, "Extraordinary transmission and left-handed propagation in miniaturized stacks of doubly periodic subwavelength hole arrays," *Opt. Express*, vol. 15, no. 3, p. 1107, 2007.
- [185] A. E. Cetin, M. Dršata, Y. Ekşioğlu, and J. Petráček, "Extraordinary Transmission Characteristics of Subwavelength Nanoholes with Rectangular Lattice," *Plasmonics*, vol. 12, no. 3, pp. 655–661, 2017.
- [186] M. Beruete, M. Navarro-Cía, S. A. Kuznetsov, and M. Sorolla, "Circuit approach to the minimal configuration of terahertz anomalous extraordinary transmission," *Appl. Phys. Lett.*, vol. 98, no. 1, pp. 3–5, 2011.
- [187] M. Beruete, M. Navarro-Cia, and M. Sorolla Ayza, "Understanding Anomalous Extraordinary Transmission From Equivalent Circuit and Grounded Slab Concepts," *IEEE Trans. Microw. Theory Tech.*, vol. 59, no. 9, pp. 2180–2188, Sep. 2011.
- [188] A. Alvarez-ordóñez, *Fourier Transform Infrared Spectroscopy in Food Microbiology*. .
- [189] A. Barth, "Infrared spectroscopy of proteins," vol. 1767, pp. 1073–1101, 2007.
- [190] R. Karoui, G. Downey, and C. Blecker, "Mid-infrared spectroscopy coupled with chemometrics: A tool for the analysis of intact food systems and the exploration of their molecular structure-quality relationships-A review," *Chem. Rev.*, vol. 110, no. 10, pp. 6144–6168, 2010.
- [191] B. Stuart, B. George, and P. McIntyre, *Modern Infrared Spectroscopy*. Wiley, 1996.
- [192] T. Wenzel, "Molecular and Atomic Spectroscopy: Instrumentation," *Chem. Libr.*, 2020.
- [193] S. Higson, *Química Analítica*. Buenos Aires: McGraw-Hill/Interamericana de Mexico, 2007.
- [194] Oregon State University, "CH 335 Organic Chemistry," 2019. [Online]. Available: <http://sites.science.oregonstate.edu/~gablek/CH335/>. [Accessed: 21-Jun-2021].
- [195] B. Stuart, *Infrared Spectroscopy: Fundamentals and Applications*. John Wiley & Sons, 2004.
- [196] Thermo Scientific, "Advantages of a Fourier Transform Infrared Spectrometer," 2000.
- [197] W. Reusch, *Spectroscopy*. Libretexts, 2020.
- [198] F. Jenkins and H. White, *Fundamentals of Optics*, 4th ed. McGraw-Hill, 1976.
- [199] M. E. Allendorf, "Use of FTIR for Rapid Authentication and Detection of Adulteration of Food," *Annu. Rev. Food Sci. Technol.*, vol. 2, pp. 467–483, 2011.
- [200] D. F. Swinehart, "The Beer-Lambert Law," *J. Chem. Educ.*, vol. 39, no. 7, pp. 333–335, 1962.

- [201] H. Food and Drug Administration, *Economically Motivated Adulteration; Public Meeting; Request for Comment*. 2009, pp. 15497–15499.
- [202] European Commission, “Food safety,” 2018. [Online]. Available: https://ec.europa.eu/food/safety/agri-food-fraud_en. [Accessed: 29-Sep-2021].
- [203] J. Spink and D. C. Moyer, “Defining the Public Health Threat of Food Fraud,” *J. Food Sci.*, vol. 76, no. 9, pp. R157–R163, 2011.
- [204] W. Klaypradit and S. Kerdpiboon, “Application of Artificial Neural Networks to Predict the Oxidation of Menhaden Fish Oil Obtained from Fourier Transform Infrared Spectroscopy Method,” pp. 475–480, 2011.
- [205] M. Ruiz, M. J. Beriain, M. Beruete, K. Insausti, J. M. Lorenzo, and M. V. Sarriés, “Application of MIR Spectroscopy to the Evaluation of Chemical Composition and Quality Parameters of Foal Meat : A Preliminary Study,” *Foods*, vol. 9, no. 1, p. 583, 2020.
- [206] M. Lucarini, A. Durazzo, J. Sánchez del Pulgar, P. Gabrielli, and G. Lombardi-Boccia, “Determination of fatty acid content in meat and meat products: The FTIR-ATR approach,” *Food Chem.*, vol. 267, no. November 2017, pp. 223–230, 2018.
- [207] S. Daoud *et al.*, “Fast and direct analysis of oxidation levels of oil-in-water emulsions using,” *Food Chem.*, vol. 293, pp. 307–314, 2019.
- [208] M. Petersen, Z. Yu, and X. Lu, “Application of Raman Spectroscopic Methods in Food Safety : A Review,” *Biosensors*, vol. 11, no. 6, pp. 1–22, 2021.
- [209] A. Rohman, “The employment of Fourier transform infrared spectroscopy coupled with chemometrics techniques for traceability and authentication of meat and meat products,” *J. Adv. Vet. Anim. Res.*, vol. 6, no. 1, pp. 9–17, 2018.
- [210] F. Farouk *et al.*, “Fast detection of bacterial contamination in fresh produce using FTIR and spectral classification,” *Spectrochim. Acta Part A Mol. Biomol. Spectrosc.*, vol. 277, p. 121248, 2022.
- [211] M. Bizzani, D. William, M. Flores, L. Alberto, and M. David, “Non-invasive spectroscopic methods to estimate orange firmness, peel thickness, and total pectin content,” *Microchem. J.*, vol. 133, pp. 168–174, 2017.
- [212] A. Lainé *et al.*, “Assessing the effect of pregnancy stage on milk composition of dairy cows using mid-infrared spectra,” *J. Dairy Sci.*, vol. 100, no. 4, pp. 2863–2876, 2017.
- [213] K. R. Borba, D. P. Aykas, M. I. Milani, L. A. Colnago, M. D. Ferreira, and L. E. Rodríguez-saona, “Portable near Infrared Spectroscopy as a Tool for Fresh Tomato Quality Control Analysis in the Field,” *Appl. Sci.*, vol. 11, no. 7, p. 3209, 2021.
- [214] R. Ríos-Reina, J. M. Camiña, raquel M. Callejón, and S. M. Azcarate, “Spectralprint techniques for wine and vinegar characterization, authentication and quality control: Advances and projections,” *TrAC Trends Anal. Chem.*, vol. 134, p. 116121, 2021.
- [215] N. Prieto, O. Pawluczyk, M. Edward, R. Dugan, and J. L. Aalhus, “A Review of the Principles and Applications of Near-Infrared Spectroscopy to Characterize Meat, Fat, and Meat Products,” *Appl. Spectrosc.*, vol. 71, no. 7, pp. 1403–1426, 2017.

- [216] M. J. Beriain, F. C. Ibañez, E. Beruete, I. Gomez, and M. Beruete, "Estimation of Fatty Acids in Intramuscular Fat of Beef by FT-MIR Spectroscopy," *Foods*, vol. 10, no. 1, pp. 1–13, 2021.
- [217] L. Qiao, X. Tang, X. Zhu, and Y. Su, "Rapid nondestructive evaluation of duck meat pH and color using visible and near-infrared reflectance spectroscopy visible and near-infrared reflectance spectroscopy," *Spectrosc. Lett.*, vol. 50, no. 8, pp. 456–461, 2017.
- [218] H. Jiang, S. Yoon, H. Zhuang, and W. Wang, "Predicting Color Traits of Intact Broiler Breast Fillets Using Visible and Near-Infrared Spectroscopy," *Food Anal. Methods*, vol. 10, no. 10, pp. 3443–3451, 2017.
- [219] S. Lam *et al.*, "Performance of near-infrared spectroscopy in pork shoulder as a predictor for pork belly softness," *Can. J. Anim. Sci.*, vol. 389, pp. 386–389, 2021.
- [220] A. Zaj, L. Dymi, J. Lorenc, and J. Hanuza, "Fourier Transform Infrared and Raman Spectroscopy Studies of the Time-Dependent Changes in Chicken Meat as a Tool for Recording Spoilage Processes," *Food Anal. Methods*, vol. 10, no. 3, pp. 640–648, 2017.
- [221] J. M. Caceres-Nevaldo, A. Garrido-Varo, E. De Pedro-Sanz, D. Tejerina-Barrado, and D. C. Perez-Marin, "Non-destructive Near Infrared Spectroscopy for the labelling of frozen Iberian pork loins," *Meat Sci.*, vol. 175, 2021.
- [222] J. M. Lorenzo, M. V. Sarriés, A. Tateo, P. Polidori, D. Franco, and M. Lanza, "Carcass characteristics, meat quality and nutritional value of horsemeat: A review," *Meat Sci.*, vol. 96, no. 4, pp. 1478–1488, 2014.
- [223] A. M. Salih, D. M. Smith, J. F. Price, and L. E. Dawson, "Modified extraction 2-thiobarbituric acid method for measuring lipid oxidation in poultry," *Poult. Sci.*, vol. 66, no. 9, pp. 1483–1488, 1987.
- [224] M. J. Lagarda, J. G. Mañez, P. Manglano, and R. Farré, "Lipid hydroperoxides determination in milk-based infant formulae by gas chromatography," *Eur. J. Lipid Sci. Technol.*, vol. 105, no. 7, pp. 339–345, 2003.
- [225] T. Ichinose, M. G. Miller, and T. Shibamoto, "Gas chromatographic analysis of free and bound malonaldehyde in rat liver homogenates," *Lipids*, vol. 24, no. 10, pp. 895–898, 1989.
- [226] M. Estévez, "Protein carbonyls in meat systems: A review," *Meat Sci.*, vol. 89, no. 3, pp. 259–279, 2011.
- [227] M. Estévez, D. Morcuende, S. Ventanas, and J. Ventanas, "Oxidación de proteínas cárnicas (I): importancia científica y tecnológica," *Eurocarne*, vol. 208, no. I, pp. 56–65, 2012.
- [228] C. N. Oliver, B. W. Ahn, E. J. Moerman, S. Goldstein, and E. R. Stadtman, "Age-related changes in oxidized proteins," *J. Biol. Chem.*, vol. 262, no. 12, pp. 5488–5491, 1987.

Author Merits

Publications

- [PAPER A] - **Jáuregui-López, I.**; Rodríguez-Ulibarri, P.; Urrutia, A.; Kuznetsov, S.A.; Beruete, M. Labyrinth Metasurface Absorber for Ultra-High-Sensitivity Terahertz Thin Film Sensing. *Phys. status solidi - Rapid Res. Lett.* 2018, 12, 1800375.
- [PAPER B] - **Jáuregui-López, I.**; Rodríguez-Ulibarri, P.; Kuznetsov, S.A.; Quemada, C.; Beruete, M. Labyrinth Metasurface for Biosensing Applications: Numerical Study on the New Paradigm of Metageometries. *Sensors* 2019, 19, 4396.
- [PAPER C] - **I. Jáuregui-lópez,** K. Insausti, M. Beriain, and M. Beruete, "Metageometries for Polycyclic Aromatic Hydrocarbon Detection at THz Range in Food Systems," *IEEE Sens. J.*, vol. 5, no. 5, 2021.
- [PAPER D] - **Jáuregui-López, I.**; Rodríguez-Ulibarri, P.; Kuznetsov, S.A.; Nikolaev, N.A.; Beruete, M. THz Sensing With Anomalous Extraordinary Optical Transmission Hole Arrays. *Sensors* 2018, 18, 3848.
- [PAPER E] - **I. Jáuregui-López,** B. Orazbayev, V. Pacheco-peña, and M. Beruete, "Tripod-Loop Metasurfaces for Terahertz-Sensing Applications: A Comparison," *Appl. Sci.*, vol. 10, no. 6504, 2020.
- [PAPER F] - **I. Jáuregui-López,** F. Zulategi, M. J. Beriain, M. V. Sarriés, M. Beruete, and K. Insausti, "Lipid and Protein Oxidation Marker Compounds in Horse Meat Determined by MIR Spectroscopy," *Foods*, vol. 9, no. 12, pp. 1–19, 2020.
- [PAPER 7] - Beruete, M.; **Jáuregui-López, I.** Terahertz Sensing Based on Metasurfaces. *Adv. Opt. Mater.* 2019, 1900721

Conferences

International

- [1] **I. Jáuregui-López**, K. Insausti, M.J. Beriain, and M. Beruete, “Metageometries-based absorber for THz Polycyclic Aromatic Hydrocarbons Identification”, *16th International Congress on Artificial Materials for Novel Wave Phenomena – Metamaterials 2022*.
- [2] **I. Jáuregui-López**, K. Insausti, M.J. Beriain, and M. Beruete, “Polycyclic Aromatic Hydrocarbons Identification with THz Metageometries”, *Optical Sensors and Sensing Congress 2022*.
- [3] **I. Jáuregui-López**, B. Orazbayev, V. Pacheco-Peña, and M. Beruete, “THz Tripod Metasurfaces for Sensing Applications: From the Basic, to More Elaborated Designs”, *15th International Congress on Artificial Materials for Novel Wave Phenomena – Metamaterials 2021*.
- [4] **I. Jáuregui-López**, P. Rodriguez-Ulibarri, Sergei A. Kuznetsov, and M. Beruete, “High Sensitivity THz Sensing with Labyrinth Absorber Metasurfaces”, *V International Conference on Metamaterials and Nanophotonics – Metanano 2020*.
- [5] **I. Jáuregui-López**, P. Rodriguez-Ulibarri, Sergei A. Kuznetsov, and M. Beruete, “THz Sensing exploiting the Anomalous Extraordinary Optical Transmission in Hole Array Metasurfaces”, *Optical Sensors and Sensing Congress 2020*.
- [6] **I. Jáuregui-López**, P. Rodriguez-Ulibarri, Sergei A. Kuznetsov, and M. Beruete, “Labyrinth Absorber Metasurface Based on Metageometries for High Sensitivity Sensing Applications”, *Optical Sensors and Sensing Congress 2020*.
- [7] **I. Jáuregui-López**, P. Rodriguez-Ulibarri, Sergei A. Kuznetsov, and M. Beruete, “Labyrinth Absorber based on Metageometries Metasurface for Fungi Detection”, *14th European Conference on Antennas and Propagation, EUCAP 2020*.
- [8] **I. Jáuregui-López**, P. Rodriguez-Ulibarri, A. Urrutia, Sergei A. Kuznetsov, and M. Beruete, “High-sensitivity labyrinth metasurface working at THz for thin-film sensing”, *13th International Congress on Artificial Materials for Novel Wave Phenomena – Metamaterials 2019*.
- [9] **I. Jáuregui-López**, P. Rodriguez-Ulibarri, A. Urrutia, Sergei A. Kuznetsov, and M. Beruete, “Labyrinth Metasurface-based Devices for High-sensitivity Thin Film Sensing”, *44th International Conference on Infrared, Millimeter and Terahertz Waves (IRMMW-THz), 2019*.

- [10] **I. Jáuregui-López**, P. Rodríguez-Ulibarri, A. Urrutia, Sergei A. Kuznetsov, and M. Beruete, “THz Thin Film Sensing with Labyrinth Metasurface Absorber”, *13th European Conference on Antennas and Propagation, EUCAP 2019*.
- [11] P. Rodríguez-Ulibarri, **I. Jáuregui** and M. Beruete, “Non-Bianisotropic Complementary Split Ring Resonators Metasurfaces”, *11th International Congress on Advanced Electromagnetic Materials in Microwaves and Optics, Metamaterials 2017*.
- [12] **I. Jáuregui**, P. Rodríguez-Ulibarri, Sergei A. Kuznetsov and M. Beruete, “THz Sensing with Classical FSS”, *10th International Congress on Advanced Electromagnetic Materials in Microwaves and Optics, Metamaterials 2016*.

National

- [1] **I. Jáuregui-López**, B. Orazbayev, V. Pacheco-Peña, and M. Beruete, “Electric Field Enhancement in THz Tripod Metasurfaces for Sensing Applications”, *XXXVII Simposio Nacional de la Unión Científica internacional de Radio, URSI 2022*.
- [2] **I. Jáuregui-López**, P. Rodríguez-Ulibarri, Sergei A. Kuznetsov, and M. Beruete, “Anomalous Extraordinary Transmission for metasurface THz Sensing Applications in Hole Arrays”, *XXXV Simposio Nacional de la Unión Científica internacional de Radio, URSI 2020*.
- [3] **I. Jáuregui-López**, P. Rodríguez-Ulibarri, A. Urrutia, Sergei A. Kuznetsov, and M. Beruete, “Labyrinth Metasurface Absorber for High-Sensitivity Thin film Sensing”, *XXXIV Simposio Nacional de la Unión Científica internacional de Radio, URSI 2019*.
- [4] P. Rodríguez-Ulibarri, Pablo, **I. Jáuregui-López**, Sergei A. Kuznetsov, and M. Beruete, “Metasuperficies basadas en anillos complementarios sin bianisotropía”, *XXXII Simposio Nacional de la Unión Científica internacional de Radio, URSI 2017*.
- [5] P. Rodríguez-Ulibarri, Pablo, **I. Jáuregui-López**, Sergei A. Kuznetsov, and M. Beruete, “THz sensing structures based on classical cross-dipole FSS”, *XXXI Simposio Nacional de la Unión Científica internacional de Radio, URSI 2016*.

